Int J Earth Sci (Geol Rundsch) (2010) 99:1267–1303
DOI 10.1007/s00531-009-0459-8

ORIGINAL PAPER

Higher Himalayan Shear Zone, Sutlej section: structural geology and extrusion mechanism by various combinations of simple shear, pure shear and channel flow in shifting modes

Soumyajit Mukherjee · Hemin A. Koyi

Received: 8 September 2008 / Accepted: 18 May 2009 / Published online: 24 June 2009

Abstract The Higher Himalayan Shear Zone (HHSZ) in the Sutlej section reveals (1) top-to-SW ductile shearing, (2) top-to-NE ductile shearing in the upper- and the lower strands of the South Tibetan Detachment System ($STDS_U$, $STDS_L$), and (3) top-to-SW brittle shearing corroborated by trapezoid-shaped minerals in micro-scale. In the proposed extrusion model of the HHSZ, the E_1-phase during 25–19 Ma is marked by simple shearing of the upper sub-channel defined by the upper strand of the Main Central Thrust (MCT_U) and the top of $STDS_U$ as the lower- and the upper boundaries, respectively. Subsequently, the E_{2a}-pulse during 15–14 Ma was characterized by simple shear, pure shear, and channel flow of the entire HHSZ. Finally, the E_{2b}-pulse during 14–12 Ma observed simple shearing and channel flow of the lower sub-channel defined by the lower strand of the Main Central Thrust (MCT_L) and the top of the $STDS_L$ as the lower- and the upper boundaries, respectively. The model explains the constraints of thicknesses of the $STDS_U$ and the $STDS_L$ along with spatially variable extrusion rate and the inverted metamorphism of the HHSZ. The model predicts (1) shear strain after ductile extrusion to be maximum at the boundaries of the HHSZ, which crudely matches with the existing data. The other speculations that cannot be checked are (2) uniform shear strain from the MCT_U to the top of the HHSZ in the E_1-phase; (3) fastest rates of extrusion of the lower boundaries of the $STDS_U$ and the $STDS_L$ during the E_{2a}- and E_{2b}-pulses, respectively; and (4) variable thickness of the $STDS_L$ and rare absence of the $STDS_U$. Non-parabolic shear fabrics of the HHSZ possibly indicate heterogeneous strain. The top-to-SW brittle shearing around 12 Ma augmented the ductile extruded rocks to arrive a shallower depth. The brittle–ductile extension leading to boudinage possibly did not enhance the extrusion.

Keywords Higher Himalayan Shear Zone · Extrusion · Ductile shearing · Channel flow · Brittle shearing · Detachment

S. Mukherjee (✉)
Department of Earth Sciences, Indian Institute of Technology Bombay, Powai, Mumbai 400076, India
e-mail: soumyajitm@gmail.com; msoumyajit@yahoo.com

H. A. Koyi
Hans Ramberg Tectonic Laboratory, Uppsala University, 752 36 Uppsala, Sweden

Introduction

Intracontinental collision between the Indian- and the Eurasian plates since ~55 Ma had deformed and remobilized the Proterozoic Indian crust by dismembering it along a number of thrusts of regional dimensions viz. Main Central Thrust (MCT), Main Boundary Thrust and Main Frontal Thrust. A part of this deformed crust presently occurs as a longitudinal strip as the 'Higher Himalaya' (Gansser 1983; Thakur 1992; Valdiya 1998)—also referred as the 'Greater Himalayan Sequence' by the Dalhousie school (Grujic et al. 1996, 2002), and the 'Higher Himalayan Crystalline Sequence' by the Austrian group (e.g. Vannay and Grasemann 2001; Vannay et al. 2004)—is overlain by the Tethyan Sedimentary Zone in the northeast and underlain by the Lesser Himalayan sedimentary rocks in the southwest (Fig. 1). From structural pxoint of view, the Higher Himalaya has been referred as the 'Higher Himalayan Shear Zone' (HHSZ) by the Roorkee school (Jain and Anand 1988; Jain and Manickavasagam 1993; Manickavasagam et al. 1999; Jain et al. 2000, 2002, 2005a; Mukherjee 2007, 2008; Mukherjee and Koyi 2009b) and recently as an

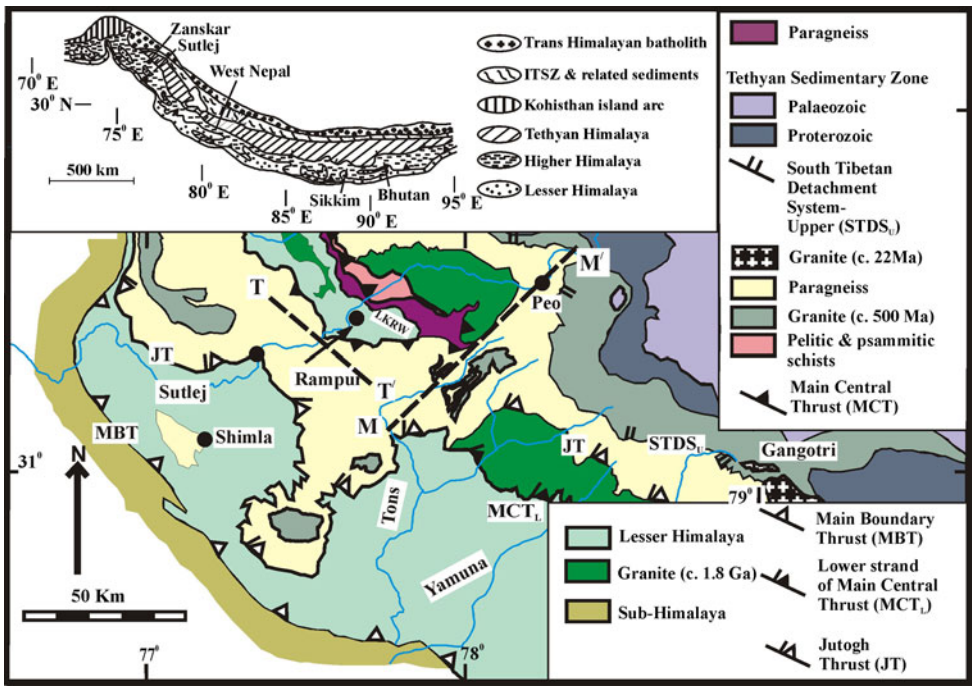

Fig. 1 Tectonic map of the Higher Himalayan Shear Zone, Sutlej section and nearby areas. Compiled from Jain and Anand (1988), Singh (1993), and Vannay and Grasemann (2001). *LKRW* Larji Kulu Rampur Window, *MCT* Main Central Thrust, *MCT$_L$* Main Central Thrust-Lower, *JT* Jutogh Thrust, *MBT* Main Boundary Thrust, *LH* Lesser Himalaya. The Sangla Detachment/Jhala Detachment (Vannay and Grasemann 2001) and the lowest strand of the MCT are designated as the 'South Tibetan Detachment System Upper' (STDS$_U$) and the 'MCT-Lower' (MCT$_L$), respectively as per Godin et al. (2006). Location of the MCT$_L$ is taken as that given for the MCT of Jain and Anand (1988) and Singh (1993). The Wangtu Gneissic Complex is considered as parts of the HHSZ following Singh (1993). Had it not been cut by the JT, the position of the MCT$_L$ would have been the *dashed line* TT′. Perpendicular to TT′is the line MM′ along which ratios of thicknesses of the parts of the HHSZ is calculated in Fig. 9

'orogenic channel' by the tectonic modelers at Dalhousie (e.g. Beaumont et al. 2001, 2004; Jamieson et al. 2004).

Compared to the different longitudinal tectonic units in the Himalaya, the HHSZ has received the greatest attention amongst structural geologists due to its diverse tectono-metamorphic uniqueness discovered during last few decades. This includes (1) inverted metamorphism defined by a northeastward increase in metamorphic grades along the dip direction of the main foliation, (2) the presence of an extensional ductile shear zone within the top of the HHSZ, commonly referred as the 'South Tibetan Detachment System' (STDS), in an overall compressional regime, (3) the simultaneity of extensional ductile shearing in the STDS along with compressional shearing near the base of the shear zone both occurring around Middle Miocene, and (4) the presence of 3–7% partially molten crust in southern Tibet at 25–30 km depth in a sub-horizontal channel that partly acted as the source for the extruding rocks of the HHSZ (Caldwell et al. 2009; reviews by Godin et al. 2006; Yin 2006; Harris 2007).

The base of the HHSZ is delimited by the MCT in the south that separates Lesser Himalayan rocks to that of the Precambrian–Proterozoic greenschist to amphibolite facies schistose and gneissose rocks of the HHSZ. The northern part of the HHSZ is characterized by profound magmatism, anatexis, migmatization, and injection of granitic melt at around 18 Ma (e.g. reviews by Searle 1999; Law et al. 2004; Vannay and Grasemann 2001; Jain et al. 2002; Yin 2006). Within the HHSZ in different sections, a distinct phase of thrust movement has been documented in the field and has been confirmed by geochronologic data. In the Sutlej section of the western Himalaya, this thrust is named as Vaikrita Thrust (VT), whereas it is called the MCT-II in Nepal in the eastern Himalaya (Godin et al. 2006 and references therein). A common name, 'MCT-Upper' (MCT$_U$) has recently been assigned to this thrust and the classical MCT lying at south as the 'MCT-Lower' (MCT$_L$) by Godin et al. (2006). The 1–10 km thick southern region of the HHSZ bounded by the MCT$_L$ and the MCT$_U$ that shows intense deformation and mylonitization has also been differently viewed as the 'MCT Zone' (e.g. Thakur 1992 for review; Grujic et al. 1996; Grasemann et al. 1999; Vannay and Grasemann 2001; Grujic et al. 2002; Carosi et al. 2007; Kohn 2008) and has been described by others as a tectonic mélange of Higher Himalayan- and Lesser Himalayan rocks (Martin et al. 2005 and references therein).

The STDS that separates the Paleozoic Mesozoic Tethyan Sedimentary Zone north from the HHSZ is a ductile extensional shear zone with 15–18 km throw and 80 km

heave (see review by Grujic et al. 1996) with local orogen parallel movement that may be of trivial regional significance (Yin 2006 and references therein). Within the HHSZ and north to the MCT_U, a second extensional ductile/brittle–ductile/brittle shear zone occurs and is designated the 'STDS-Lower' ($STDS_L$), and the previously defined STDS at north as the 'STDS-Upper' ($STDS_U$) (Godin et al. 2006). The main foliation and the tectonic boundaries MCT_L, MCT_U, $STDS_L$ and $STDS_U$ dip towards northeast and are sub-parallel (e.g. Martin et al. 2005; Goscombe et al. 2006; Robinson et al. 2006). The optimum timing of compressional top-to-SW sense of ductile shearing of the MCT_L and the MCT_U, and the extensional top-to-NE sense of ductile shearing of the $STDS_L$ and the $STDS_U$ compiled and deciphered from cooling ages of minerals are 15–0.7, 25–14, 24–12, and 19–14 Ma, respectively (Godin et al. 2006). However, Harris (2007) cautioned that ductile shearing along these tectonic boundaries were not necessarily continuous processes during these time ranges.

From the $STDS_U$, a top-to-SW sense of ductile shearing has also been reported as a relic fabric, e.g. from the locally known Zanskar Shear Zone in the Suru–Doda valley (Patel et al. 1993), the Sangla Detachment from the Sutlej section (Vannay and Grasemann 2001; Vannay et al. 2004) and from further west in the Main Mantle Thrust in Pakistan (Argles and Edwards 2002). No reports of a top-to-SW sense of shearing have been made so far from the $STDS_L$. While the $STDS_L$ has been recognized from a few sections in the eastern Himalaya e.g. at Gonto la (Edwards et al. 1996) and as the Lhotse Detachment from the Everest massif (Searle 1999; Searle et al. 2003; Law et al. 2004), it is absent in the Alaknanda-, Bhagirathi- (Jain et al. 2002), Dhauliganga- and Goriganga sections in Indian Himalaya (field observations of the first author) and also from the Pakistan Himalaya (review by DePietro and Pogue 2004). This means that the $STDS_L$ persists discontinuously within the HHSZ.

Four categories of models of extrusion vis-à-vis inverted metamorphism of the HHSZ have been put forward since 1930s. These are (1) thermal-, (2) coupled thermo-mechanical-, (3) post-metamorphic deformation-, and (4) syn-metamorphic deformation models (Yin 2006 and his review; also see Hodges 2006 and Dasgupta et al. 2009 for other grouping). However, given a wide variation in tectonic framework of the HHSZ in different sections, none of these could embrace all the tectonic and metamorphic constraints (see Hodges 2000 for review). Recently the channel flow model (Fig. 2, Eq. 4 in "Appendix") has evolved as an almost unanimously accepted extrusion mechanism of the HHSZ through the wedge-shaped HHSZ in the Bhutan Himalaya (Grujic et al. 1996, 2002; Hollister and Grujic 2006), implicitly for the Zanskar section (Stephenson et al. 2001; also see Mukherjee and Koyi 2009b), and eventually for all the Himalayan sections by the Dalhousie research

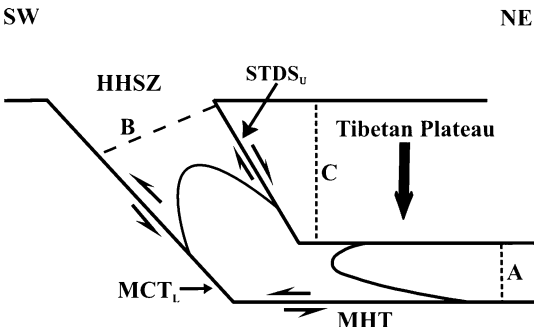

Fig. 2 A simplified NE–SW cross-section of the diverging upward inclined Higher Himalayan Shear Zone (HHSZ). The lower and the upper boundaries of the HHSZ are the Main Central Thrust-Lower (MCT_L) and the top of the South Tibetan Detachment System-Upper ($STDS_U$), respectively. The MCT_L merges at depth with the Main Himalayan Thrust (MHT). The MHT in reality is sub-horizontal (see Beaumont et al. 2001) but is simplified to be a horizontal one. The MHT undergoes a top-to-SW sense of shearing. The over-thickened crust of the Tibetan plateau exerts pressure on the horizontal channel, squeezes and feeds molten rocks into the inclined channel leading to extrusion of the HHSZ. Parameters *A*, *B* and *C* are the thickness of the horizontal channel, that of the HHSZ, and the depth at which the upper boundary of the HHSZ meets the horizontal channel, respectively. Parabolic velocity profiles of extrusion are produced in the two channels. The figure is a simplification of Figure 2b of Jamieson et al. (2004). Neither to scale nor angle

group (e.g. Beaumont et al. 2001, 2004; Jamieson et al. 2002, 2004; also see reviews by Burbank 2005; Jain et al. 2005a, b; Mukherjee 2005; Godin et al. 2006; Hodges 2006; Jessup et al. 2006; Grujic 2006; Dewey 2008; Mukherjee 2009a). The Dalhousie school of modeling suggested the channel flow began at 34 Ma in a sub-horizontal channel below the Tibetan plateau. The HHSZ acted as a linked inclined channel through which rocks were extruded toward the surface since 24 Ma (Harris 2007 and references therein) (Fig. 2). Recently, the channel flow extrusion has been considered as the trigger of the out-of-sequence thrusting in the HHSZ in different sections (see Hollister and Grujic 2006; Carosi et al. 2007; Mukherjee 2007; Mukherjee et al. 2008, 2009).

The velocity profile of extrusion of the HHSZ with its characteristic ductile shear senses is a function of the shape of the shear zone. Interpreting Nelson et al.'s (1996) seismic results differently and contrary to the commonly held view of its parallel-wall geometry (e.g. Figure 1b of Vannay and Grasemann 2001), Grujic et al. (1996, 2002) presented the HHSZ as a diverging upward crustal wedge (simplified in Fig. 2) where the MCT_L and the $STDS_U$ converge at mid-crustal depth at 90° E longitude. For such a geometry of the HHSZ, extrusion through it induced by a pressure gradient will be of Jeffery–Hamel type, which is kinematically different from a channel flow. In the Jeffery–Hamel flow, depending on the angle of divergence of the walls and the Reynolds Number of the flow, a number of inflection points in the velocity profile can appear (LeCureux and Burnett

1975 but also others) leading to multiple reverses in shear sense. We note that the possibility of a Jeffery–Hamel flow in extrusion of the HHSZ was considered neither in Beaumont et al.'s (2001) original model of channel flow nor in its later refinement by the Dalhousie school (e.g. Jamieson et al. 2004).

In this study, we report the dominant ductile and brittle deformation patterns in the Sutlej section of the HHSZ in the NW Indian Himalaya from meso- and micro-scales. Based on the structural information, we recast the constraints of ductile extrusion of the shear zone. Discussing a few of the existing important extrusion models, we demonstrate that they are insufficient to describe these constraints. As a consequence, a model of ductile extrusion is proposed that also takes care of negative results obtained from trialed analytical- and analogue models. The brittle–ductile and brittle deformations of the HHSZ reported here do not contribute to the proposed model but gives a complete picture of the deformation pattern of the shear zone and aftereffects of the ductile extrusion.

We note a discrepancy in terminologies in fluid mechanics to categorize specific flow patterns. For example, Rogers (1978) used the term 'plane Couette flow' to represent the 'Couette Poiseuille flow' of Schlichting and Gersten (1999). In our work from now on, 'channel flow'/'Poiseuille flow' will be used to denote laminar flow of an incompressible Newtonian viscous fluid under a pressure gradient through long parallel walls.

The study area

Geology

The HHSZ in the Sutlej River section (Figs. 1, 3) in Rampur- and Kinnaur districts of the state Himachal Pradesh in India is accessible for fieldwork by the National Highway-22A (NH-22A) that runs parallel to the Sutlej River. The rocks of the HHSZ are dominantly gneisses and schists with greenschist to amphibolite facies metamorphism and are of Precambrian and Proterozoic in age (Grasemann et al. 1999; Vannay et al. 1999; Jain et al. 2000, 2002 and references therein; Vannay and Grasemann 2001). The Lesser Himalayan sedimentary rocks also occur inside the HHSZ as the Larji–Kulu–Rampur Window (LKRW) bounded by the MCT. Strands of the MCT- one passing through Karcham as the MCT_U and the other surrounding the LKRW are characterized by mylonite zones (Fig. 3). Southwest to the LKRW the exposed granites gneisses are dated at 1,865 ± 60 Ma (review by Vannay et al. 2004). Northeast of the LKRW, the lithologies of the HHSZ are dominantly pelitic- and psammitic schists and are separated from the 1,866 ± 10 Ma old granites around Wangtu (Singh 1993).

Rocks of the HHSZ northeast to Karcham belong to the Vaikrita Group of Srikantia and Bhargava (1998). From Karcham to Shongthong, the lithologies are dominantly quartzites, psammitic- and pelitic schists. Further northeast

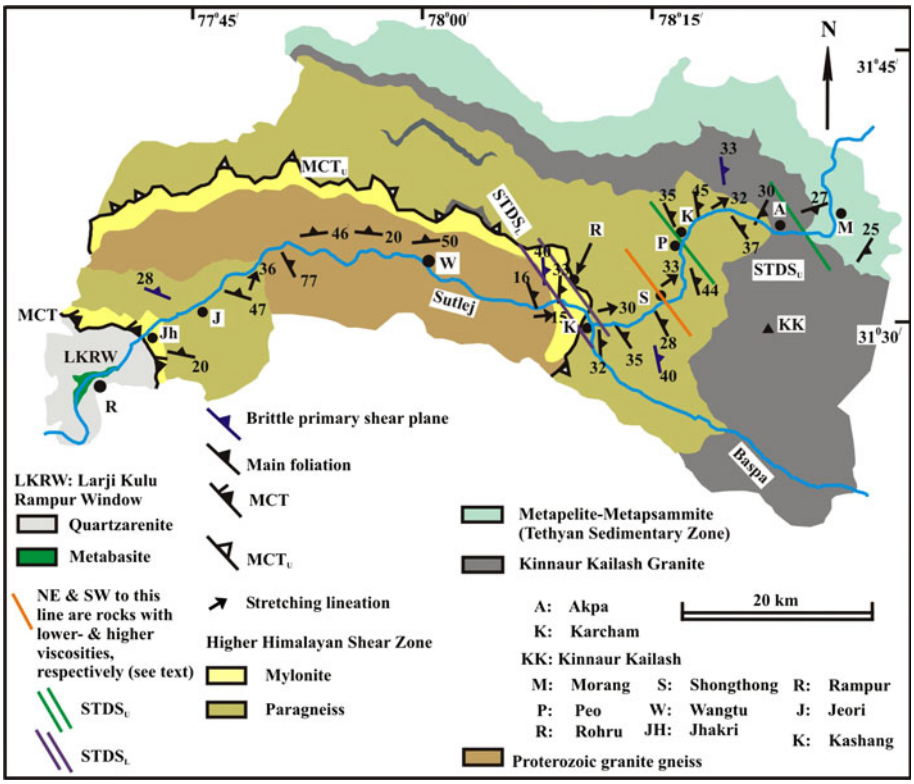

Fig. 3 Geological map of the Higher Himalayan Shear Zone, northeast to the Larji Kulu Rampur Window (LKRW). Compiled and simplified from Singh (1993), Srikantia and Bhargava (1998) and Vannay and Grasemann (1998). The location of the Main Central Thrust (MCT) that bounds the Lesser Himalayan rocks is as per Singh (1993). The Vaikrita Thrust of Srikantia and Bhargava (1998) is designated as the 'MCT-Upper' (MCT_U) of Godin et al. (2006). Litho-units of lower- and higher viscosities during the top-to-NE sense of ductile shearing, attitudes of main foliations, stretching lineations, brittle shear planes, and ductile extensional shear zones in two strands, the $STDS_L$ and the $STDS_U$ are shown

from Shongthong, migmatites followed by the Kinnaur Kailash Granite (KKG) are present- the later are at places pegmatites. The KKG yielded Rb–Sr ages of 453 ± 9 and 477 ± 29 Ma (Kwatra et al. 1999) and young zircon and apatite fission track ages range between 16.3 ± 1.6 to 13.6 ± 1.3 Ma and 4.9 ± 0.8 to 2.6 ± 1.2 Ma, respectively (Vannay et al. 2004). On the Akpa–Ashrang road north to Akpa, the upper boundary of the HHSZ is the contact between the psammitic- and pelitic schists of the Tethyan Sedimentary Zone in the north and granite in the south. The location is in conformity with that previously shown in Figure 1 of Vannay et al. (1999). The contact is extrapolated along the NW–SE Himalayan trend onto the NH-22A, which passes between the locations Akpa and Morang (Fig. 3). The paragneiss northeast to Karcham was reported to be migmatitic along a thinner nearly N–S trending zone that stretches from Baspa valley in the south onto the Sutlej section between the locations Kashang and Akpa in the north (Figure 1 of Vannay et al. 1999). In contrast, our fieldwork revealed that the migmatitic character starts to develop northeastward from Shongthong (Fig. 3) that can be deciphered from the outcrops alongside the NH-22A (such as Fig. 4a) and attains prominence towards north up to the exposures of the KKG.

Field studies reveal that the extensional ductile shear zone within the top of the HHSZ, Sutlej section, the same as the $STDS_U$ as used by Godin et al.'s (2006) terminology, was simultaneous with the injection of granitic melts (Figs. 4a, 5a–d). This indicates that during the extensional shearing event, the rocks in this zone underwent a reduction in viscosity. Within a narrower span of 15–14 Ma of possible simultaneous activation of the MCT_L, the MCT_U, the $STDS_L$, and the $STDS_U$ (from Godin et al. 2006), lithologies that bear signatures of extrusion of the HHSZ in terms of either a top-to-NE or a top-to-SW sense of ductile shearing can be grouped into two rheological categories (Fig. 3). The first category is (1) *rocks with higher viscosity*, from the MCT_L up to Shongthong. The rocks of the LKRW are not included in this group since (a) they are Lesser Himalayan, and (b) the window was exhumed by a late phase doming during the Pliocene–Quaternary Periods (Jain et al. 2002). The doming was a structurally dissimilar event to that of the HHSZ. The granites around Wangtu are also excluded as they mostly escaped ductile shearing

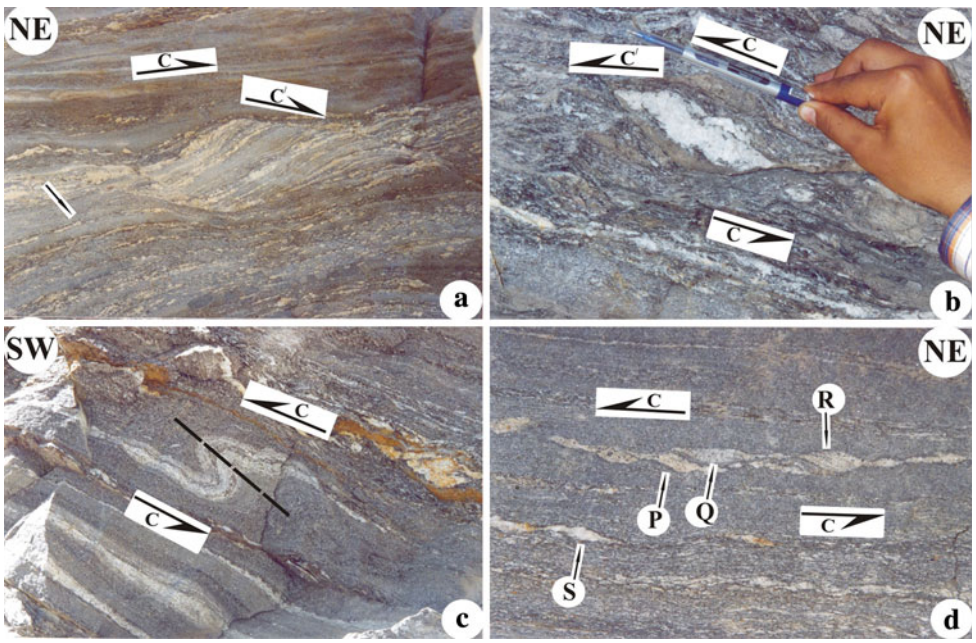

Fig. 4 Top-to-SW sense of ductile shearing demonstrated by different shear sense indicators in the HHSZ outside the $STDS_U$ and the $STDS_L$. **a** S–C–C′fabric defined by thicker leucosome and thinner melanosome layers within migmatite at Shongthong. Prominent secondary synthetic shear C′-plane sharply deflects the S-fabrics. The C-plane is discontinuously occupied by leucosomes, shown by an *arrow*, indicates migmatization syntectonic to this S–C shearing event. The angles between S- and C-, and C- and C′-planes are 30° and 16°, respectively. **b** A sigmoid quartz vein defining the S fabric within gneiss. The C-planes are sharp, straight and discrete. The aspect ratio of the sheared vein is 4.8. The angle between the long axis of the vein and the C-plane, the long axis and the C′-plane, and the C- and the C′-planes are 3°, 24° and 19°, respectively. At Jeori (**c**), intrafolial fold of quartz rich layer in migmatitic gneiss. The main foliation planes or the C-planes enveloping this fold are straight and parallel. Inclination of axial trace (marked by a *dashed line*) of the fold to the main foliation gives the shear sense. The angle between the axial trace of the fold and the C-plane is 13°. At Powari (**d**) A train of sigmoid leucosomes in migmatite that indicate the sense of primary shearing. The C-plane is sub-horizontal. Leucosomes *P*, *Q*, *R* and *S* have aspect ratios 6.7, 6.5, 4 and 5.8, respectively. The angles between the C-plane to the long axes of these leucosomes are within a close range of 5°–8°. Near Pangi

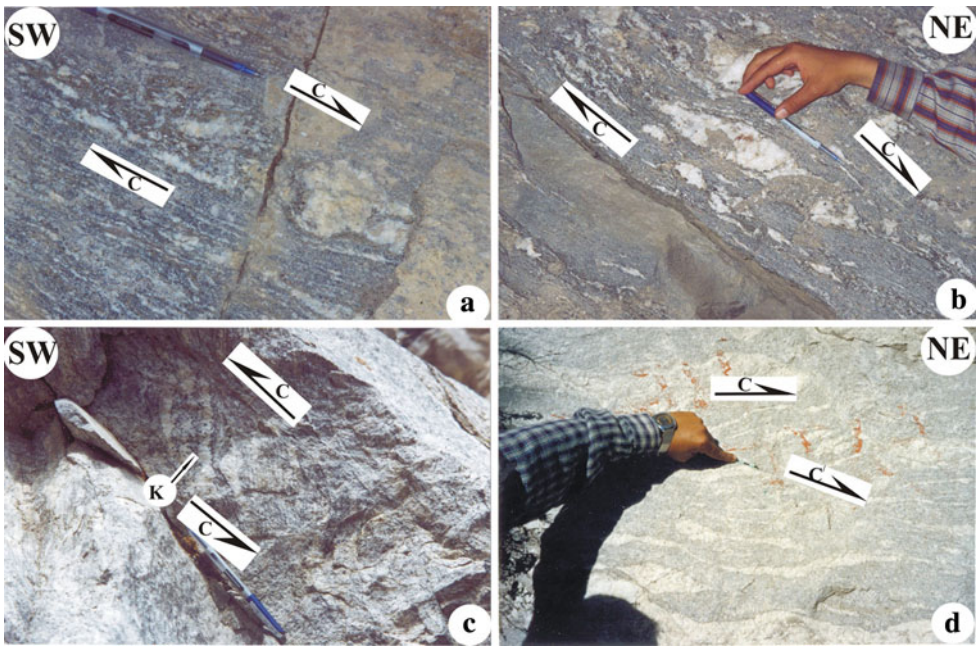

Fig. 5 Dominant top-to-NE extensional ductile shearing and rare top-to-SW compressional ductile shearing noted in migmatite from the $STDS_U$. **a** S–C fabric defined by thicker leucosomes and thinner melanosomes giving a top-to-NE extensional ductile shearing. The angle between the S- and the C-planes is 23°. Located between Pangi- and Kashang bridges. **b** A thick sigmoid-leucosome, with an aspect ratio 5.6 shows a top-to-NE extensional ductile shearing. The long axis of the leucosome is at 20° to the C-plane. Near Kashang bridge, **c** S–C fabric showing a relic top-to-SW ductile shearing. The S-planes are defined by alternate layers of thicker leucosomes and thinner melanosomes. The C-planes are defined by thin and straight melanosomes. The angle between the S- and the C-planes is 45°. Located between Kashang and Kharo bridges. The leucosome *K* has an aspect ratio of 9.5. **d** S–C fabrics defined by leucosomes and melanosomes, showing a top-to-NE extensional shearing. Leucosome layers locally define thin straight secondary synthetic C′-shear planes. The angle between the S- and the C-, and that between the C- and the C′-planes are 20° and 21°, respectively. Near Kharo bridge

possibly due to deformation partitioning. On other hand, the vast stretch of Proterozoic gneiss south to Shongthong is included that underwent ductile shearing without the presence of a leucosome melt phase. The second category is (2) *rocks with lower viscosity,* within the upper part of the HHSZ northward from Shongthong that include migmatites and granites. The contact between the two categories of rocks delineated at Shongthong is a 'spot observation' on the NH-22A and is extrapolated on the map (Fig. 3) for the sake of presentation.

From the lower part of the HHSZ to the MCT_U, the peak metamorphism is characterized by an increase in temperature from 610 to 700°C and a drop in pressure from 900 to 700 MPa (Vannay et al. 1999). Northward from the MCT_U, the temperature increases from 570 to 750°C at nearly a constant pressure of 8 MPa. These thermo-barometric data, along with the presence of isograds of high-grade minerals at the base- and profound melt activities within the top of the HHSZ indicate an inverted metamorphism in the shear zone (Vannay et al. 1999; Vannay and Grasemann 2001). Reviewing the P–T data of this terrain, Vannay and Grasemann (2001) concluded that: (1) the peak metamorphism of the HHSZ was achieved at 30 km depth; and (2) the HHSZ was extruded by simultaneous ductile extensional shearing along the $STDS_U$ and ductile compressional shearing at its south.

Tectonic constraints

The HHSZ in the Sutlej section is subdivided by a few secondary thrusts such as the MCT_U of Godin et al. (2006) previously recognized as the VT (Srikantia and Bhargava 1998) and also as the MCT (Vannay et al. 1999, 2004; Vannay and Grasemann 2001). Another such thrust is the Jutogh Thrust (JT) of Jain and Anand (1988) that cuts the MCT_L of Godin et al. (2006) (Fig. 1). The Jutogh Thrust Sheet skirts around the MCT-bounded Lesser Himalayan rocks of the Larji-Kulu-Rampur Window (LKRW) (Jain et al. 2000). The continuation of the $STDS_U$ in the Sutlej section has been recognized as the mylonitic and phyllonitic Sangla Detachment with an earlier top-to-SW and a later top-to-NE senses of ductile shearing (Figure 3 of Vannay and Grasemann 2001; Figure 5 of Vannay et al. 2004). Near Karcham, the $STDS_L$ of some 100 m thickness—formerly designated as the Karcham Normal Fault by Janda et al. (2002)—is characterized by mylonitization and has a top-to-east sense of brittle normal shearing that steeply cuts the foliation planes. The ductile deformation

patterns inside this $STDS_L$ have not been discussed by the previous workers. From Godin et al.'s (2006) collated timing of activation of the tectonic planes/zones, the following statements can be made: (1) simultaneous movements between the MCT_L to the $STDS_L$ and to the $STDS_U$ could have taken place between 15–12 Ma, and 15–14 Ma, respectively; and (2) all the four tectonic zones—the MCT_L, the MCT_U, the $STDS_L$ and the $STDS_U$ were probably active within a shorter time span of 15–14 Ma. Fission track zircon-apatite ages reveal that the HHSZ in the Sutlej section acted as a number of crustal wedges within the brittle deformation regime after the ductile extrusion ceased. These wedges moved differentially towards southwest and northeast directions during the Plio-Pliestocene Period as a part of the late tectono-thermal evolution of the shear zone (Jain et al. 2000, 2002; Thiede et al. 2004; Vannay et al. 2004; Kumar et al. 2005).

Four phases of ductile deformation have been identified from different sections of the HHSZ on the meso-scale (Patel et al. 1993; Jain and Patel 1999; Jain et al. 1999, 2000, 2002, 2005). Amongst them, a top-to-SW sense of ductile shearing along northeasterly dipping primary shear planes (C-planes) throughout the HHSZ in the Sutlej section belongs to the most pervasive D_2 deformation phase (Jain and Anand 1988; Jain et al. 2002; Vannay and Grasemann 2001; Vannay et al. 2004; also Jain and Mukherjee 2009; Mukherjee 2007; Mukherjee 2009b, c; Mukherjee and Koyi 2009a). Folding of the pre-Himalayan D_1-, Himalayan D_3- (Jain et al. 2002) and superposed folding events (Vannay and Grasemann 2001; Vannay et al. 2004) are locally developed in the HHSZ and, therefore, are not characteristic of the regional deformation pattern responsible for the extrusion of the shear zone. The kinematic vorticity numbers (W_m: ratios of simple shear to pure shear) compiled from different sections of the HHSZ revealed that the top-to-SW sense of ductile shearing in the HHSZ was dominantly of simple shear type with some component of pure shear usually towards the middle of the shear zone (see review by Carosi et al. 2007). For example, using quartz micro-fabrics Grasemann et al. (1999) demonstrated a component of pure shear from the HHSZ in the Sutlej section with a W_m of 0.86. From fold morphometry, Bhattacharya (1981, 1999) documented a flattening (the pure shear component) near the MCT_U at Kumaon Himalaya. Law et al. (2004) deciphered a W_m of 0.71 near the $STDS_L$ (their 'Lhotse Detachment') in the Everest massif region. Jessup et al. (2006) deduced the W_m between 0.57 to 0.85 and 0.63 to 0.77 from inside the Mount Everest transect of the HHSZ and near the lower boundary of the shear zone, respectively. Larson and Godin (2009) calculated the parameter to be 0.67 from the lower part of the HHSZ from the Dhaulagiri section in central Nepal. Besides, Cottle et al. (2007) predicted a component of pure shear on the basis of observed synthetic- and antithetic shear bands in the $STDS_U$ in the Kharta section in the Nepalese Himalaya. Shear bands in the upper part of the HHSZ in the Nepalese Himalaya has also recently been noted by Goscombe et al. (2006).

To build an extrusion model of the HHSZ even qualitatively, the differential rates of extrusion of its tectonic boundaries should be taken into account. Due to the paucity of such data from the Sutlej section, in this work we rely on those data available from other sections. A similar approach was adopted in proposing the 'general shear model' of extrusion of the HHSZ by Vannay and Grasemann (2001). While in the Nepal Himalaya, the slip-rate on the MCT_L was 9 mm $year^{-1}$ (Whipp et al. 2005), 3–5 mm $year^{-1}$ (review by Yin 2006), 1.2 mm $year^{-1}$ (Valdiya 2001), or a still lower magnitudes such as 0.8 mm $year^{-1}$ (Wobus et al. 2005) and 0.37 ± 0.13 mm $year^{-1}$ (Yin 2006 and references therein), the ductile extensional slip on the $STDS_U$ was $\sim$2 cm $year^{-1}$ (Annen et al. 2005 and references therein), i.e. at least four times faster. A similar higher rate of slip on the $STDS_U$ of 1.2–3.3 cm $year^{-1}$ from the Zanskar Himalaya (Dèzes et al. 1999) and 4.7 cm $year^{-1}$ from the Nepal Himalaya (Hodges et al. 1998) are also reported. The rate of extensional slip on the $STDS_L$ is so far not available from any of the Himalayan sections. The combined activation of the boundaries of the HHSZ gave rise to fast extrusion on the shear zone in the Sutlej section at a rate of 2.2 mm $year^{-1}$ till 16 Ma and at 0.6 mm $year^{-1}$ between 16 and 3 Ma (Vannay et al. 2004). A high rate of erosion of 1.6 mm $year^{-1}$ of the HHSZ by the Sutlej River (Vannay et al. 2004) might have accelerated the extrusion rate of the HHSZ. In the Sutlej section of the HHSZ at a higher resolution, variable rates of extrusion across the $STDS_U$ of 1.4 ± 0.2 mm $year^{-1}$ and 1.1 ± 0.4 mm $year^{-1}$ in the brittle deformation regime has been deciphered. As this variable extrusion rate has been attributed to the differential erosion induced by a spatial disparity in monsoonal precipitation during Pliocene–Quarternary Periods (Thiede et al. 2004), it will not be taken in account in modeling the ductile extrusion.

The present geometry of the HHSZ is a product of a series of complicated deformational phases related to India–Asia collision initiating from around 55 Ma. The thickness of the HHSZ changed since 24 Ma to reach its present amount (Figure 2 of Jamieson et al. 2004). Compounded with this, whether the MCT_L or the MCT_U is the lower boundary of the HHSZ has been debated (see Thakur 1992 for review), giving rise to reports of a wide range of thicknesses of the shear zone from 6 to 50 km (Jain and Manickavasagam 1993; Lombardo et al. 1993; Wu et al. 1998; Vannay and Grasemann 2001; Stephenson et al. 2000). As the HHSZ and the linked feeder horizontal channel define the geometry of a ramp and a flat, respectively, the thickness of the later varies along its length with an average thickness of 25 km (Figure 8a of Hauck et al. 1998). At 15 Ma, the depth at which the inclined

channel met the horizontal channel was 35 km (Figure 3 of Jamieson et al. 2004). In the Zanskar section, the thickness of the $STDS_U$, locally known as Zanskar Shear Zone, is of an order of few kilometers (Walker et al. 1999) and is therefore much thinner than the greatest reported thickness of the HHSZ as 50 km by Jain and Anand (1988).

Not only the HHSZ, but the thickness of the $STDS_U$ also varies along its length. For example, in the Zanskar section, it ranges between 2.25 and 6.7 km (Herren 1987), 0.5 and 2.5 km (Jain and Patel 1999), 1.6 km on average (Figure 17 of Searle et al. 1988) or is 1 km (Dèzes 1999). Over tens of kilometers as well, the thickness of the continuation of the $STDS_U$ is variable along the trend of the Himalaya (Vannay and Grasemann 2001). For example, the thickness is at least 5 km in a part of the Nepal Himalaya (Carosi et al. 1999), 1.5 km in Dhaulagiri area in Nepal Himalaya (Kellet 2006; Kellett and Godin 2009), or 1 km in the eastern Himalaya (Molli et al. internet reference), especially in and around Dzakaa Chu section where it varies between 1000 and 800 m (Cottle et al. 2006, 2007), and is as low as 350–400 m in the Annapurna section (Searle and Godin 2003). The thicknesses of the $STDS_U$ in the Sutlej section has so far been unavailable despite several structural studies carried out in this section (e.g. Singh 1993; Jain et al. 2000; Vannay and Grasemann 2001) as its lower boundary remained unidentified.

The horizontal channel that acted as the feeder of the HHSZ and resides below the Tibetan plateau had a thickness of around 25 km and the proto-HHSZ had a maximum slope of $\sim 60°$ at 24 Ma (Figure 2 of Jamieson et al. 2004). With time, the HHSZ moved en-mass towards the foreland and its dip was reduced to 30° (Figure 2b of Vannay and Grasemann 2001) or 40° (Figure 6 of Yin 2006) at present. However, a greater amount of dip of 60° is still present at places in the central Himalaya (Yin 2006, p. 31).

Partially molten rocks are reported in the sub-horizontal channel at 25–30 km below southern Tibet (Nelson et al. 1996) located northward in the dip direction of the HHSZ. Recent magnetotelluric investigations from Garhwal sector of the Himalaya indicate the presence of a zone of low resistivity (<10 Ωm) around 5 km below the MCT zone possibly indicating partially melting (Israil et al. 2008). These, along with the presence of solidified granitic melts as leucosomes in migmatites and also granites restricted to the upper parts of the HHSZ suggests that in its ductile regime, the shear zone extruded like a fluid.

Structural geology

Ductile deformations

Except for a few local folds, the main foliations in the HHSZ are planar and dip usually at moderate angles 30°–35° towards northeast. Stretching lineations are defined on the main foliation planes and plunge towards northeast (also see Figure 3a of Vannay and Grasemann 2001). Within the zone of rocks with lower viscosity, the main foliations/C-planes and also the S-planes are defined by granitic melts/leucosomes (Figs. 4a, d, 5b–d), which indicate syn-shearing/syntectonic migmatization (Marchildon and Brown 2003). It is expected that rheological softening induced by the extruding melt during ductile shearing facilitated the deformation in this zone.

Throughout the HHSZ, the northeasterly dipping main foliation planes that acted as the primary shear planes (the C-planes) are rarely sub-horizontal (Fig. 4a, d). S–C fabrics (Bèrthe et al. 1979) (Fig. 4a), sigmoid quartz veins and leucosomes (Figs. 4b, d, 6c, d), and asymmetric intrafolial folds (as referred by Ghosh 1993) (Fig. 4c) denote a top-to-SW sense of ductile shearing. This deformation initiated around 25 Ma with the activation of the MCT_U within the HHSZ and continued until the recent past at 0.7 Ma in the lower part of the HHSZ at the MCT_L (Godin et al. 2006). Thus, the southwestward shearing seemingly migrated southward, but not necessarily continuously, within a span of ~ 24 Ma. It is important to mention here that not only at its boundaries, but the ductile shearing is found to be distributed throughout the HHSZ in contrary to Grasemann et al.'s (1999) and Dasgupta et al.'s (2009) previous findings from this section and from the Sikkim Himalaya, respectively.

The angles between the S-planes of this shear sense and the C-planes in the shear zone are within 25°–43°, which is close to the higher angular limit of 45° as mentioned by Passchier and Trouw (2005). The axial planes of the intrafolial folds are at 12°–22° to the NE direction of the C-planes. The long axes of sigmoid leucosomes and quartz veins are at very low angle 3°–8° to the C-planes. The aspect ratios (long axis/short axis) of these sigmoid elements show a wide variation between 3.6 and 9.5. Some of the S-fabrics are occasionally affected by secondary C′-shearing synthetic to the main shearing event (Figs. 4a, b, 5d). The angle between the C- and the C′-planes range between 15° and 25°. This is well within the limit of 15°–35° previously compiled from different shear zones by Passchier and Trouw (2005). The C′-planes are planar but are shorter than the C-planes. As the C′-planes are much less ubiquitous in the HHSZ, they cannot be responsible for regional extrusion of the HHSZ. In this work, the C′-shear planes are not considered in defining zones of extensional ductile shearing i.e. the detachments. The overall planar nature of the main foliations/C-planes is utilized in modeling the extrusion mechanism.

Interestingly, an additional phase of a top-to-NE sense of extensional ductile shearing, deciphered from intrafolial folds (as referred by Ghosh 1993) of quartz rich layers (Fig. 6a), S–C fabrics (Bèrthe et al. 1979) (Fig. 5c, d), and sigmoid-shaped quartz veins and leucosomes (Fig. 6b) are

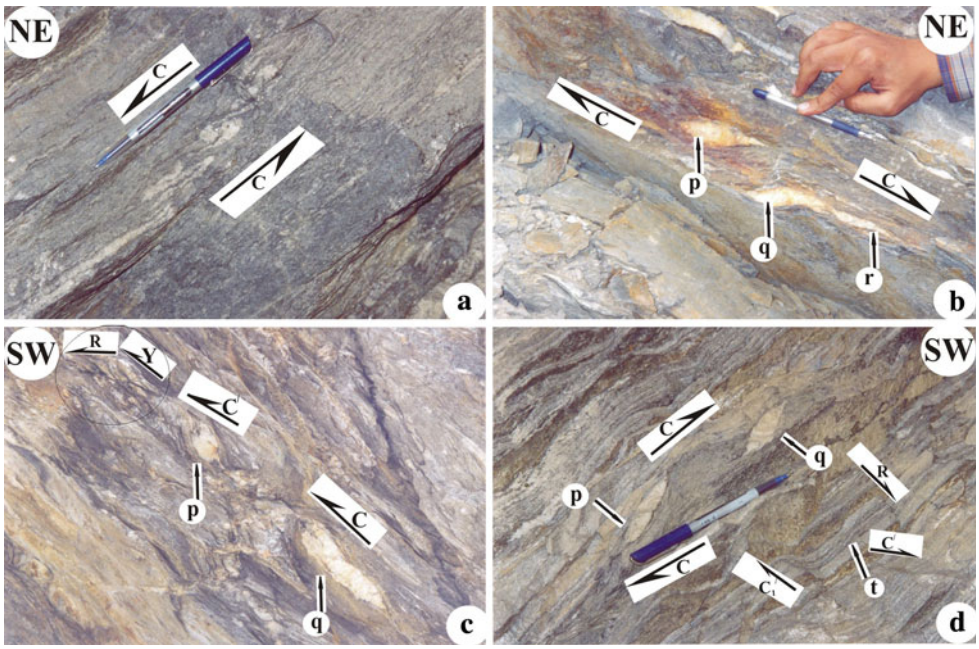

Fig. 6 Both top-to-NE extensional and top-to-SW compressional ductile shearing are documented from the $STDS_L$, located near Karcham. Host rock: psammitic schist. **a** Intrafolial overturned fold of quartz vein with thick rounded hinges and thin limbs give a top-to-NE sense of extensional ductile shearing. The axial traces of such folds are at 10°–15° to the C-shear plane. Note that the primary shear planes also act as the enveloping surfaces of the fold. **b** A number of sigmoid quartz veins showing a top-to-NE extensional ductile shearing. Veins *p*, *q* and *r* have aspect ratios $R = 3.9$, 4.4 and 8.21, respectively. The angles between the long axes of these veins with the C shear plane are 12°, 17° and 8°, respectively. Very high value of *R* and very low θ for vein *r* is a manifestation of its extremely elongated geometry along the C-plane indicating intense shearing. **c** Sigmoid- and elongated veins of quartz, *p* and *q* with aspect ratios 2.8 and 4.9, respectively, indicate a top-to-SW sense of compressional ductile shearing. The angles between their long axes to the C-planes are 17° and 10°, respectively. Prominent synthetic C′-shear plane at low angle (10°) to the C-plane is also displayed. Duplexes of smaller dimensions bounded by the Y-planes and showing a top-to-SW sense of shearing are present and is marked with a circle. These duplexes are affected by synthetic Riedel shear R-planes. The primary brittle shear Y-planes are coincident with the C-planes. The angle between the R- and the Y-plane is 37°. **d** Sigmoid and lenticular veins of quartz, *p* and *q* with aspect ratios 3.2 and 4.9, respectively, indicate a top-to-SW sense of compressional ductile shearing. The angle between their long axes with the C-plane are ~16°. Synthetic secondary ductile shear C′-plane is at 46° to the C-plane. Synthetic secondary brittle–ductile shear plane C_1' is at 75° to the C-plane. An abrupt brittle slip at 86° to the Y-plane is deciphered to be the synthetic secondary Riedel R-shearing. The Y-plane is not seen in the photograph. Here the R-shear is developed without any nearby presence of primary brittle Y-shear planes in adjacency. Part of the rock mass, pointed out as *t*, is bounded by C_1'- and R-planes

found to be confined within two zones in meso-scale in the HHSZ. We recognize these zones as 'detachments' to represent 'low-angle normal faults' as per Davis and Reynolds (1996), but in the ductile shear regime. The top-to-NE sense of ductile shearing is restricted in two zones within the northeasterly dipping C-planes same as that for the top-to-SW sense. One of these zones, designated as the $STDS_L$, is delineated at the locality Karcham (Fig. 3) where the $STDS_L$ in the brittle regime was documented as steeply dipping KNF by Janda et al. (2002). The MCT_U of Godin et al. (2006) or the VT of Srikantia and Bhargava (1998) also passes through the same locality. This is in contrast to other sections of the HHSZ that possess two strands of the STDS, such as the Everest massif in the Nepal Himalaya (Searle 1999) and Gonto La in southern Tibet (Edwards et al. 1996), where the $STDS_L$ occurs much to the northeast to the MCT_L.

The other zone (Fig. 3) of top-to-NE shearing, or the 'Sangla Detachment' of Vannay and Grasemann (2001), occurs within the topmost level of the HHSZ and is equated with the STDS of Burchfiel et al. (1992) or the $STDS_U$ of Godin et al. (2006). Its lower boundary is demarcated between the locations Pangi- and Kashang. The upper boundary is the same as the contact between the HHSZ and the overlying Tethyan Sedimentary Zone. The $STDS_L$ and the $STDS_U$ lie within rocks of lower- and higher viscosities, respectively. The boundaries of the $STDS_U$ and the $STDS_L$ do not match with those of the two litho-units of contrasting viscosities. In these ductile extensional shear zones, fabrics of a top-to-SW sense of shearing also occur less frequently (Figs. 5c, 6c, d, 8b). Therefore, the southwesterly shearing is considered as a precursor deformation event to the top-to-NE shearing, and might be products of 25–5 and 15–0.7 Ma periods of activation of the MCT_U and the MCT_L, respectively. Since the $STDS_U$ and the $STDS_L$ are spatially separated, the relative timing between extensional

ductile shearing in these two zones remains indeterminate from field structural studies.

In the $STDS_U$ and the $STDS_L$ in meso-scale, the angles between the S- and the C- fabrics showing a top-to-NE sense of shearing and those between the C- and the C′-planes show a wide variation between 18°–45° and 10°–48°, respectively. The former range approaches the higher angular limit of 45° between the respective fabrics as mentioned by Passchier and Trouw (2005). However, the later range crosses the upper limit of variation of angles between the C- and the C′-planes of 15°–35°as compiled from different shear zones by Passchier and Trouw (2005). The long axes of the sigmoid leucosomes and veins are at 8°–20° with the C-plane. The aspect ratios of the sigmoid leucosomes and quartz veins show a wide range between 2.8 and 8.21. Lack of any large-scale folds and uniformly dipping foliation planes confirm that the overturned folds within the $STDS_U$ and $STDS_L$ are intrafolial and are not secondary parasitic to other folds. These intrafolial folds are either rootless with a wavelength of ~7 cm or occur in parallel trains. Their enveloping surfaces, which are parallel, define the ductile shear C-planes. The limbs are subparallel to the axial traces, and are unequal in lengths and thicknesses. The hinges are rounded and thicker than the limbs. The axial planes dip towards SW and make 10°–17° to the NE geographic direction of the C-planes.

Thin-sections of rocks of the $STDS_L$ (Fig. 7a–d) and the $STDS_U$ (Fig. 8a–b), oriented perpendicular to the main foliations and parallel to the stretching lineations, reveal dominantly a top-to-NE sense of ductile shearing shown most abundantly by mineral fish (ten Grotenhuis et al. 2002; also Mukherjee and Pal 2000) of sigmoid geometries (Fig. 8a), S–C fabrics (Bèrthe et al. 1979) (Fig. 7a) and rarely by the sigmoidally oriented inclusion pattern inside porphyroblasts (Fig. 7b). The sense of shear deciphered from the orientation of the S-planes with respect to the C-planes is opposite to that deduced from the inclusion patterns. Some of the mica fish (Lister and Snoke 1984) possess a mouth at one of their corners possibly due to their dynamic recrystallisation (Fig. 8a). The top-to-NE sheared higher grade rigid porphyroblastic index minerals indicate the extensional shearing to be quite intense (Fig. 7c). In the $STDS_L$, pronounced extension parallel to the main foliation is deciphered from crystal-plastic extension of rigid and high-grade minerals such as garnet with aspect ratios as high as 9.5 (Fig. 7d). The sheared geometries of these index minerals, however, are partially destroyed by migration of quartz into them from the matrix. The

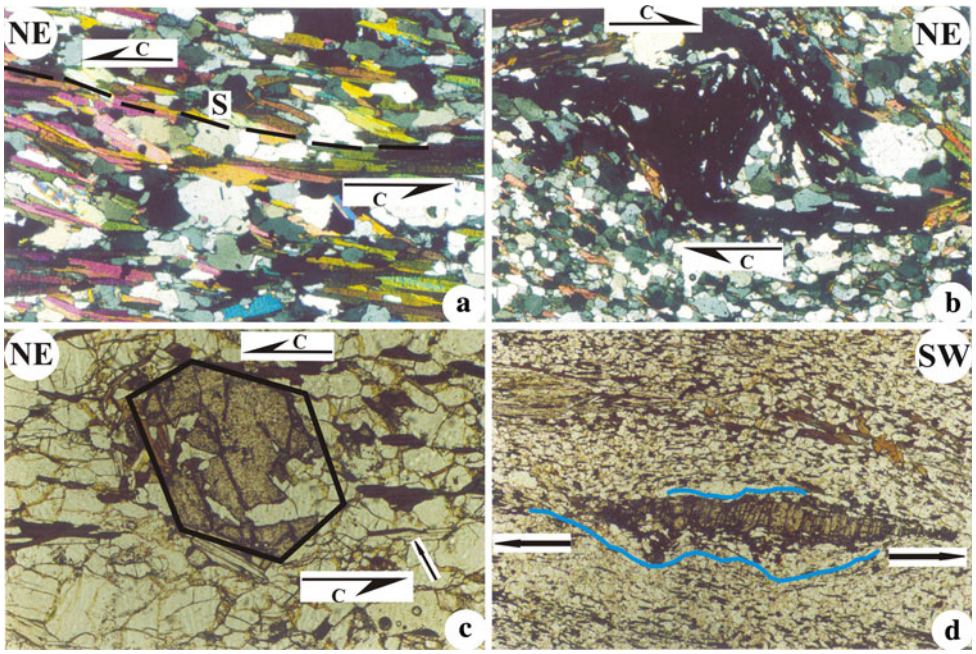

Fig. 7 (**a**–**c**) A top-to-NE sense of extensional ductile shearing is demonstrated by the XZ oriented thin-sections (**a**–**d**) from the $STDS_L$, near Karcham. **a** S–C fabric displayed by micas. The C-planes are almost straight. The S-planes are defined by discrete mica grains, and one of those is traced by a *broken black line*. The S-plane is at low angle (11°) to the C-plane and is curved mainly at the contacts with the C-planes. Photo in cross polarized light. Photo length: 5.0 mm. Thin-section number: SJ24. **b** Sigmoidally oriented inclusions within a sheared garnet porphyroblast. Photo in cross polarized light. Photo length: 2.0 mm. Thin-section number: SJ29. **c** Sheared porphyrblast of garnet partly destroyed by migration of boundaries of quartz grains in the matrix into it. Elongated biotite grains in the matrix pointed out with an *arrow* define the C-plane. Photo in plane polarized light. Photo length: 5.0 mm. Thin-section number: SJ11. **d** Extremely stretched garnet grain with a very high aspect ratio of 9.3. Its long axis is parallel to the main foliation. Warping of the main foliation around the grain is shown with *blue lines*. Photo in plane polarized light. Photo length: 5.0 mm. Thin-section number: SJ15

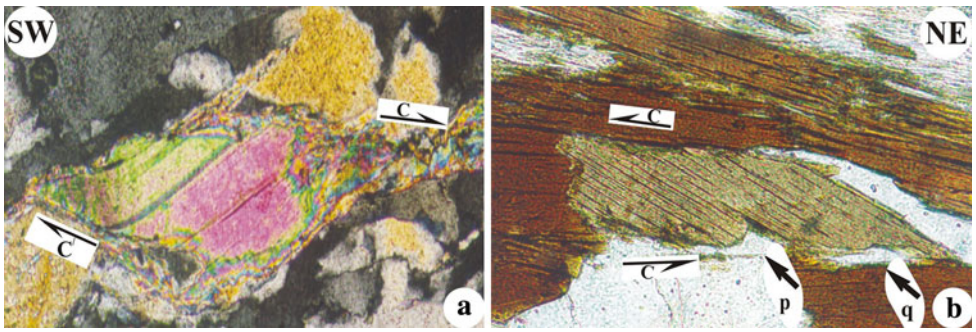

Fig. 8 XZ oriented thin section from the $STDS_U$ reveal both top-to-NE and top-to-SW ductile shear senses. **a** Sigmoid muscovite fish with an aspect ratio of 1.9 give a top-to-NE extensional ductile shearing. The long axis of the fish is at low angle (8°) to the primary shear plane. Synthetic secondary C′-plane is at 23° to the C-plane. The fish is affected by extensive grain boundary recrystallisation at one of its tips. Photo in cross polarized light. Photo length: 4 mm. Thin-section number: SJ34. **b** Parallelogram-shaped biotite fish with an aspect ratio of 4.7 gives a top-to-SW sense of ductile shearing. The angle between the C-plane to the inclined boundary and the long axis of the parallelogram fish are 25° and 11°, respectively. The C-plane is prominently marked by fish trail at *arrow p*. Migration of boundary of the adjacent quartz grain at *arrow q* has partly destructed the accurate parallelogram shape. Photo in plane polarized light. Photo length: 1 mm. Thin-section number: SJ17

S-fabrics are sometimes defined by a number of mutually separated mica grains (Fig. 7a). The C-shear planes are short, remarkably straight and are defined by (a) foliation minerals such as biotite (Fig. 7a); and (b) trails of minerals at the corners of mineral fish (Fig. 8b). The long axes of the mineral fish are at 7°–15° to the C-planes. Their aspect ratios vary within 1.7–4.8, which are a narrower than the range of 2–16 as previously reported from different shear zones by ten Grotenhuis et al. (2002).

In meso-scale, the ductile synthetic secondary C′-shear planes of both the compressional and extensional shearing are straight, less frequently developed, affect individual mineral grains (Fig. 8a), but they are shorter than the C-planes. For both the compressional and extensional senses of ductile shearing at meso- and micro-scales, the S-planes are in most cases sigmoid and attain progressively lower angles as they come closer to the C-planes. The S-fabrics vary in thickness, length, and curvature. The shearing secondary to top-to-SW and top-to-NE senses took place either simultaneous to or later than the respective primary shearing event (Passchier and Trouw 2005). The secondary ductile shearing (C″) at a steep angle and antithetic to the top-to-NE and the top-to-SW senses of sharing are remarkably absent in the HHSZ. The C′-shearing alone may indicate a component of pure shearing (see Cottle et al. 2007) in the $STDS_U$ and the $STDS_L$.

Considering the location of the MCT_L as given in Fig. 1 which is as per Jain and Anand (1988), and the $STDS_U$ and the $STDS_L$ as delineated in this work in Fig. 3, the ratio of thicknesses $STDS_U$: $STDS_L$: HHSZ is measured along the outcrop on the maps and is then converted into the ratio of their orthogonal thicknesses as 5.2:1:34 (Fig. 9). In this calculation, the boundaries of the HHSZ, the $STDS_U$ and the $STDS_L$ are considered to dip to the NE dipping and mutually parallel (see Martin et al. 2005; Goscombe et al. 2006 for other sections). The calculated ratio holds true for any dip angle of the $STDS_U$, the $STDS_L$, the MCT_U and the MCT_L so long they are parallel. Taking their dips as 30° and 45°, the absolute thicknesses of the $STDS_U$ and the $STDS_L$ are estimated to be 5.2–7.3 and 1–1.4 km, respectively (caption in Fig. 9). It can be said that (1) both the $STDS_U$ and the $STDS_L$ are much thinner than the HHSZ; and (2) the $STDS_L$ is thinner than the $STDS_U$.

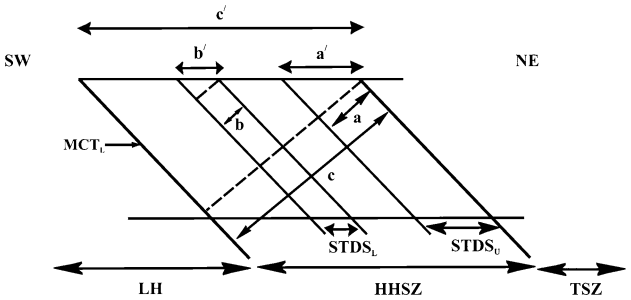

Fig. 9 The boundaries of the $STDS_U$, the $STDS_L$ and the HHSZ dip northeasterly and ideally at the same angle. Their thicknesses on the ground surface and the orthogonal thicknesses are a', b', c' and a, b, c, respectively. The parameters a', $b'$and $c'$are measured from Figs. 1 and 3 along MM′ in Fig. 1. The ratio a′:b′:c′= a:b:c comes out to be ~5.2:1:34. Considering the boundaries of shear zones dip at 30° and 45°, the b parameter is calculated as 1 and 1.4 km, respectively. With similar considerations, the a parameter is calculated as 5.2 and 7.3 km, respectively. *LH* Lesser Himalaya, MCT_L Main Central Thrust-Lower, $STDS_L$ South Tibetan Detachment System-Lower, $STDS_U$ South Tibetan Detachment System-Upper, *HHSZ* Higher Himalayan Shear Zone, and *TSZ* Tethyan Sedimentary Zone. Neither to scale nor angle

Brittle–ductile and brittle deformations

Brittle-ductile secondary shear C_1'-planes are rarely developed in the $STDS_L$ at ~75° to the primary shear C- planes. In exceptional examples, the sheared rock mass is bounded by

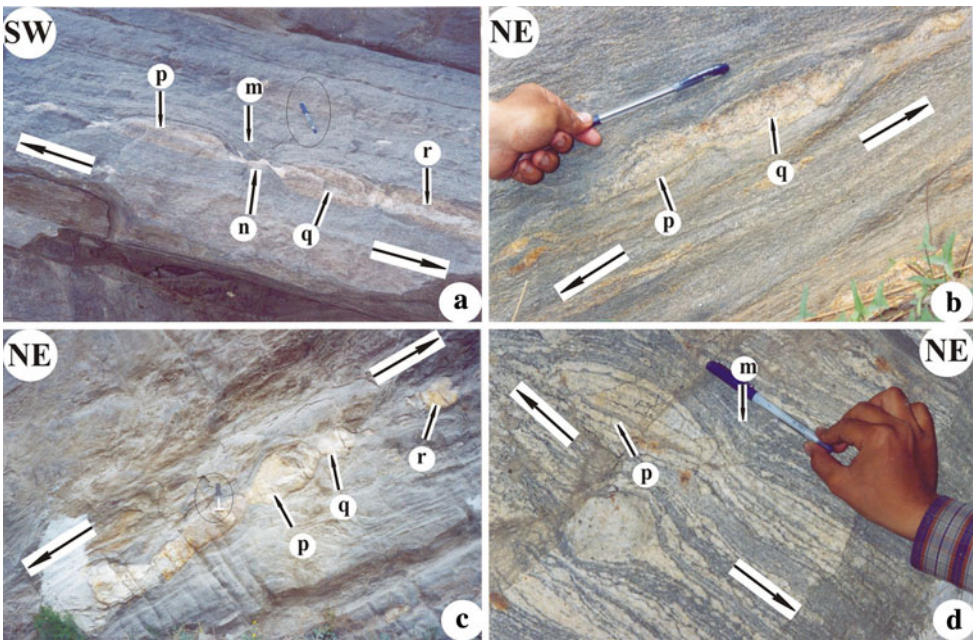

Fig. 10 Different varieties of boudins in the HHSZ indicate a phase of brittle–ductile extension. The long axes of the boudinaged clasts are parallel to the main foliation. *Arrows* indicate extension parallel to the main foliation. The main foliations show prominent scar fold at the inter-boudin separations (*arrow m* in **a**, **d**). Away from the separated clasts, the main foliations are straight and sub-parallel. **a** A boudinaged calc-silicate layer. Clasts *p* and *q* with aspect ratios 5 and 2.5, respectively, and define lenticular boudins. These clasta are separated by 17 cm. Clasts *q* and *r* define pinch and swell structures. The inter-boudin partition is filled with quartz, and is shown with a *smaller arrow*. A pen marked with a *black ellipse* is the scale. Located within the $STDS_L$, near Karcham. A pen pointed out with an ellipse is the scale. **b** Pinch and swell structure of quartz vein within psamite schist. Clasts *p* and *q* have aspect ratios 1.4 and 4, respectively. Located outside the $STDS_U$ and the $STDS_L$, near Shongthong. **c** Very large pinch and swell structure defined by quartz clasts *p* and *q*. Clast *r* defines a lenticular boudin. Clasts *p*, *q* and *r* have aspect ratios 1.9, 1.5 and 1.2, respectively. Clasts *q* and *r* are separated by 1.27 m. All the clasts have notches at one of their corners. A hammer pointed out with a *black ellipse* is the scale. Located within migmatitic gneiss host rock at Powari. **d** Foliation boudin of thick leucosome- and thin melanosome-layers within migmatite. The boudin *p* has an aspect ratio of 2.9. Located within the $STDS_U$, near Kashang

secondary shear planes—one of which is brittle (R-plane) and one is brittle–ductile (C_1'-plane) (Fig. 6d). Throughout the HHSZ, a different manifestation of brittle–ductile extension parallel to the main foliation is evident from different varieties and sizes of boudins, e.g. lenticular boudins (clasts 'p' and 'q' in Fig. 10a, clast 'r' in Fig. 10c), pinch and swell structures (clasts 'q' and 'r' in Fig. 10a, clasts 'p' and 'q' in Fig. 10c), foliation boudins (Fig. 10d), and shear fracture boudins (photograph with the authors). Calc silicate layers (Fig. 10a), quartz veins (Fig. 10c) and migmatitic foliations (Fig. 10d) are boudinaged. Interestingly, microboudins of such varied morphologies were also reported from the Zanskar Shear Zone (=$STDS_U$) by Mukherjee (2007, 2009d) and Mukherjee and Koyi (2009b).

Pinch and swell structures indicate insufficient tectonic force in comparison to the rigidity of these clasts to completely separate them. Lenticular- and foliation boudins denote small competence contrast between the clasts and the matrix (Ghosh 1993 and references therein). On other hand, foliation boudins indicate their genesis was controlled by high fluid pressure (Arslan et al. 2008). The boudinaged clasts may be separated as far as a decimeter (clasts 'p' and 'q' in Fig. 10a) or even more than a meter (clasts 'q' and 'r' in Fig. 10c). Even in a single train of boudins, the degree of separation of various clasts varies significantly (between clasts 'p' and 'q', and 'q' and 'r' in Fig. 10a). Variable distances amongst individual boudins indicate variation in their rigidities and/or local brittle–ductile extension parallel to the main foliation. Few of the lenticular clasts have notches at one of their corners (clasts 'p', 'q' and 'r' in Fig. 10c), and some do not (Fig. 10a, b, d). The aspect ratios (=long axis/short axis) of the clasts ranges between 1.5 and 5.2, which is narrower than the limit 2–20 compiled by Ghosh (1993) from different shear zones. In all the observed cases, the long axes of the boudinaged clasts are parallel to the main foliation that indicates a phase of brittle–ductile extension parallel to the main foliation. The foliation planes are drawn towards the gap created by partly or completely separated clasts and define prominent scar folds (arrow 'm' in Fig 10a, d). In some lenticular- and foliation boudins, the inter-boudin partition is filled with quartz (arrow 'n' in Fig. 10a). This indicates accumulation of the SiO_2 rich melt fraction at sites of low stress during extension parallel to foliations (Marchildon and Brown 2003). The quartz filling geometries,

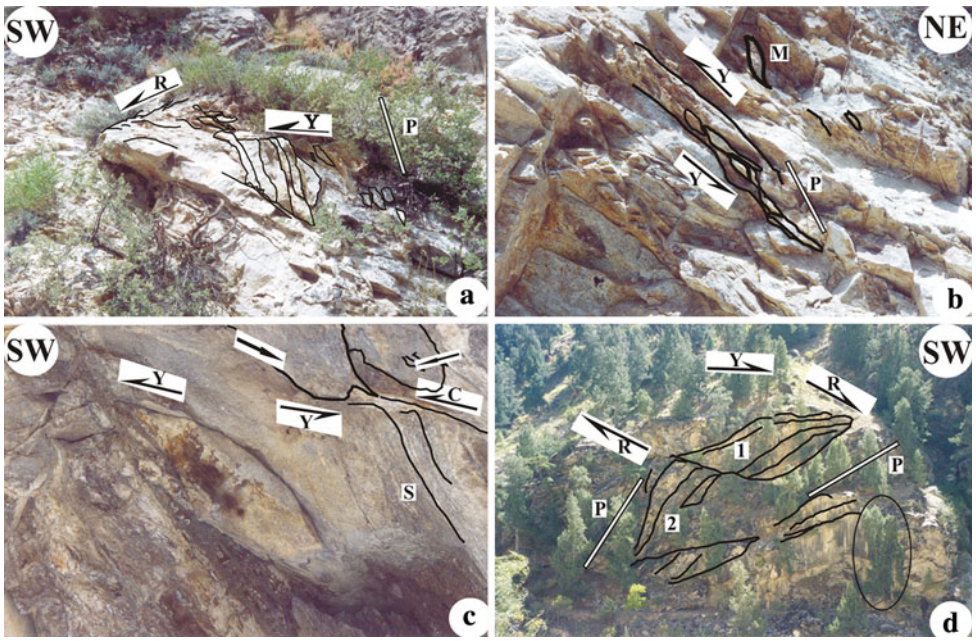

Fig. 11 Duplexes of different sizes from the HHSZ showing a consistent top-to-S/SW sense of brittle primary *Y* shearing. Some of these duplexes are also affected by secondary brittle R-shear planes. **a** The angle between the Y- and the R-planes is 28°. The orientation of the P-plane is shown by a *thick white line*. The angle between the Y- and the P-planes is ~65°. Near Samej village, outside the $STDS_U$ and $STDS_L$. **b** Long straight pair of primary brittle shear Y-planes are deciphered. A number of thrust of sigmoid thrust slices are stacked within the Y-planes. The orientation of the P-plane is shown by a *thick white line*. The angle between the Y- and the P-planes is. 35° An isolated thrust slice *M* is also noted. At Karcham within the $STDS_L$. **c** An isolated thrust slice in migmatitic gneiss. S–C fabric is also defined by the migmatitic foliation. The C-plane is parallel to the primary brittle shear Y-plane. The angle between the S- the C-plane is 40°. Above the C-plane, two brittle thrust slices are pointed out. Near Shongthong bridge, outside the $STDS_U$ and the $STDS_L$. **d** Mega-duplexes. The angle between the Y- and the P-planes in thrust slices *1* and *2* are ~33° and 63°, respectively. The orientations of the P-planes are shown by *thick white lines*. The angle between the Y- and the R-planes is 33°. Within the $STDS_U$. A ~3 m tall tree marked within an ellipse is the scale. At Kharo bridge

however, do not match their standard forms modeled and documented by Arslan et al. (2008).

Throughout the HHSZ, including the $STDS_U$ and the $STDS_L$, a late stage brittle shearing consistently in a top-to-SW sense can be determined from duplexes of dimensions ranging from few cm to several meters (Figs. 6c, 11a–d). The deduced brittle shear sense is in conformity with that deciphered from the V-pull apart structure of garnet reported from the Dhauliganga section of the HHSZ by Mukherjee (2009e). Interestingly, Saklani (2005, and references therein) considered only the MCT zone of the HHSZ in the Bhagirathi section to be a thrust nappe with a top-to-SW sense of movement. The roof- and the sole thrusts bounding these duplexes in the Sutlej section, i.e. the Y-planes, dip ~30°–40° northeasterly. Individual thrust slices are most commonly sigmoid-shaped. Both isolated (Fig. 6c, thrust slice 'M' in Fig. 11b, c) and a number of sigmoid-shaped stacked thrust slices (Fig. 11a, b, d) are noted. The P-planes of brittle shear (Passchier and Trouw 2005) are defined as the contact planes between individual thrust slices. The angles between the Y- and the P-planes widely vary between 30° and 68°. Sometimes, the angles between the Y- and the P-planes in adjacent thrust slices vary widely (Fig. 11d). Some of these thrust slices are affected by secondary brittle shearing along discontinuous and locally developed synthetic secondary 'R' shear planes (Fig. 6c, d; 11a, d). The angles between the Y- and the R-planes vary within a wide range of 25°–86°. The range is much higher than the previously compiled average value of 15° from different shear zones by Passchier and Trouw (2005). The Y-planes are found to be parallel to or the same as the primary C-shear planes (Figs. 6c, 11c). In other words, the anisotropy created by the pre-existing ductile primary shear planes acted later as the preferential sites of brittle primary shearing.

The brittle shearing prevalent on a meso-scale is also found to affect individual grains on a micro-scale in terms of duplexes of stacked-up minerals (Fig. 12a, c, d) in XZ oriented thin-sections that show the same sense of shearing as those on the field-scale. The micro-duplexes are identified by their morphological resemblance with those well established from field-scales (e.g. by McClay and Insley 1986 and references therein; Figures 6.93 & 6.96 of Davis and Reynolds 1996). The thrust-up grains are typically hat- or trapezoidal-shaped with their straight boundaries unaffected by migration of the adjacent grains. The longest boundaries of these trapezoidal grains are identified as the 'P' shear planes of

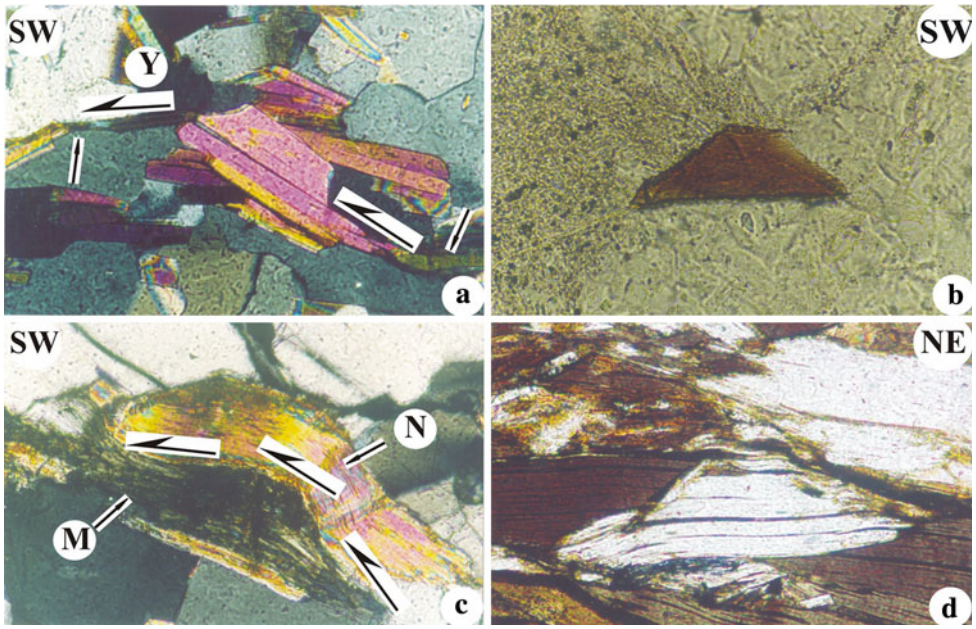

Fig. 12 Trapezium or hat-shaped mineral grains observed in the XZ-oriented thin-sections at very high magnification throughout the HHSZ including the $STDS_U$ and the $STDS_L$. These are interpreted in this work as overthrust grains. Photo lengths: 1 mm. **a** The longest arm of the hat-shaped mica is northeasterly dipping and defines the brittle shear P-plane inclined at 39° to the primary Y-shear plane. A top-to-SW sense of brittle searing is deciphered. Sharp primary brittle shear Y-planes are pointed out with *arrows*. Location: Karcham, in the $STDS_L$. Photo in cross polarized light. Thin-section number: SJ18. **b** Isolated biotite hat within quartzofeldspathic minerals with the longest boundary sub-parallel with the Y-plane. The Y-plane is not seen in the field of view. The brittle sense of shear is not attempted from this grain. Located between Kashang and Kharo, in the $STDS_U$. Photo in plane polarized light. Thin-section number: SJ21a. **c** A hat-shaped muscovite aggregate *N* is thrust over an aggregate of sillimanite *M*. A top-to-SW sense of brittle searing is deciphered. Located near south to Shonghtongh; outside the $STDS_U$ and the $STDS_L$. Photo in cross polarized light. Thin-section number: SJ25. **d** The longest grain boundary of a muscovite hat in contact with the cleavage plane of another muscovite grain. This contact is sub-parallel to the main foliation. The main foliation is not seen in the field of view. The brittle sense of shear is not attempted. Location: at Jeori; outside the $STDS_U$ and the $STDS_L$. Photo in plane polarized light. Thin-section number: SJ27

Passchier and Trouw (2005). The 'P' planes dip northeast at a moderate angle of 40° (Fig. 12a) to sub-parallel to the Y-plane (Fig. 12b, d). Few trapezoidal-shaped mica grains that are surrounded by quartzo-feldspathic minerals have their longest and straight boundaries sub-parallel to the Y-planes (Fig. 12b). These grains probably represent thrust slices that were transported relatively longer distances to the extent that they got completely detached from the underthrust counterpart grains. Such grains were exempted from determination of brittle shear sense.

The original rectangular shapes of the mica grains sometimes was modified due to extensive migration of the neighbouring quartz grains into them and give rise to 'window structures' (Jessell 1987). In these structures, the boundary of the intruding grain in contact to the neighbour grain is convex towards the later. While deciphering duplexes of mica grains, the cases of micas with curvilinear contacts with their adjacent quartz grains were negated. In other words, trapezoidal-shaped grains with (nearly) straight grain boundaries were only considered as thrust slices. A similar precaution was also adopted by Mukherjee (2007, 2008) and Mukherjee and Koyi (2009b) in sorting out trapezoidal grains from the HHSZ in other sections.

The first order structures of the Sutlej section of the HHSZ are summarized in a schematic NE–SW cross-section perpendicular to the main foliations and parallel to the stretching lineations (Fig. 13).

Formulation of the model

Constraints

The following constraints are chosen to propose an extrusion model in the ductile deformation regime of the Sutlej section of the HHSZ.

(I) The HHSZ is divisible into an upper less viscous- and a lower more viscous litho-unit prevalent during its extrusion and ductile shearing.

(II) The main foliation/primary shear planes in the HHSZ are N/NE dipping and are regionally straight.

(III) Throughout the HHSZ, a top-to-SW sense of shearing is present.

(IV) Top-to-NE sense of ductile shearing persists in two spatially separated zones, the $STDS_U$ and the $STDS_L$.

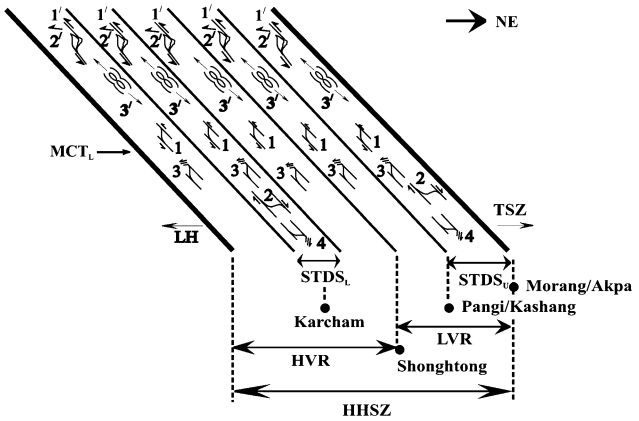

Fig. 13 The dominant structures in the HHSZ, Sutlej section deciphered from the present meso- and micro-structural studies are summarized in a NE–SW cross-section of the shear zone. The HHSZ is bounded by northeasterly dipping Main Central Thrust-Lower (MCT_L) and the Lesser Himalaya (LH) in the south, and the top of the South Tibetan Detachment System-Upper ($STDS_U$) and the beginning of the Tethyan Sedimentary Zone (TSZ) in the north. *1* Top-to-SW compressional ductile shearing. *2* Top-to-NE extensional ductile shearing confined within the $STDS_U$ and the $STDS_L$. *3* Secondary shearing synthetic to *1*. *4* Secondary shearing synthetic to *2*. *1′* Top-to-SW brittle shearing. *2′* Brittle shearing synthetic to *1′*. *3′* Boudinaging. Different fabrics were used to decode these deformations but are represented here by their single varieties. LVR and HVR stand for 'low viscosity rocks' and 'high viscosity rocks', respectively, prevalent during top-to-NE sense of ductile shearing in the HHSZ. Locations in relation to lithological and structural boundaries are indicated. The lower and the upper boundaries of the $STDS_U$ pass between the localities Pangi and Kashang, and between Morang and Akpa, respectively. The diagram is neither to scale nor angle

(V) The $STDS_U$ is present within the top of the HHSZ in the litho-unit of lower viscosity. The top boundaries of the $STDS_U$ and the low viscosity unit match, but not their bottom boundaries. The $STDS_L$ is present inside the litho-unit of the HHSZ of higher viscosity. The boundaries of this shear zone and the litho-unit do not match.

(VI) The top-to-SW sense of ductile shearing within the $STDS_U$ and the $STDS_L$ were followed by a top-to-NE sense of ductile shearing.

(VII) The possible synchrony of activation between MCT_L and $STDS_U$, MCT_L and $STDS_L$ are 15–14, 15–12 Ma, respectively. The possible simultaneity amongst MCT_L, $STDS_L$ and $STDS_U$ is between 15 and 14 Ma. The extensional shearing in the $STDS_U$ and the $STDS_L$ could either be simultaneous during 19–14 Ma, or are sequential.

(VIII) The extrusion and ductile deformation of the HHSZ took place dominantly by simple shearing with a component of pure shearing.

(IX) From the MCT_L up to the $STDS_U$, inverted metamorphism is present.

(X) At least a part of the ductile extrusion of the HHSZ took place as a fluid.

(XI) The $STDS_U$ and the $STDS_L$ are thinner than the remainder of the HHSZ.

(XII) The $STDS_L$ is thinner than the $STDS_U$.

(XIII) The thickness of the $STDS_U$ varies along its length on local- and regional scales.

(XIV) In different sections of the HHSZ, the $STDS_L$ is absent.

(XV) The rate of slip in the $STDS_U$ was faster than that near the MCT_L.

Constraint II, the synchrony of $STDS_U$ and the MCT_L as stated in VII, and VIII–X were used by Beaumont et al. (2001) in developing their classical channel flow extrusion model. The other constraints, especially I, IV and XI–XV are new additions from this work. Out of these, constraints XI–XIII, i.e. the presence of $STDS_L$ and the ratio of thicknesses $STDS_U$:$STDS_L$:HHSZ in the Sutlej section are contributions of this structural study. The rate of extensional slip on the $STDS_U$ in the Sutlej section is presently not known. For this reason it is taken from other sections as the constraint XV. Constraint I about the rheologic division of the HHSZ is selectively used in two of the analytical trials and was found not to be useful in explaining the other constraints. Different possibilities of simultaneous trigger of the $STDS_U$, $STDS_L$, MCT_U and MCT_L, as compiled in VII, are checked whether they are feasible fluid mechanically.

Existing relevant models

Simple shear model

The simple shear model (Jain and Manickavasagam 1993; Hubbard 1996; also Jain and Manickavasagam 1997) explains inverted metamorphism in the Zanskar section of the HHSZ by considering a consistent top-to-SW sense of simple shearing (constraint III in "Constraints") along northeasterly dipping numerous straight discrete shear planes (Fig. 14a, constraint II in "Constraints") giving rise to its extrusion around 25 Ma. The metamorphic isograds were kinked on a regional scale in response to simple shearing and gave rise to inverted metamorphism throughout the HHSZ (constraint IX in "Constraints"). Along with the P–T data, millimeter- to decimeter scale displacements along the C-planes have been calculated to extrude the HHSZ rocks cumulatively from a depth of at least 30–35 km.

Further works (Manickavasagam et al. 1999; Jain et al. 1999, 2002; Tripathi and Gairola 1999) from other sections of the HHSZ provided structural- and thermo-barometric data that support this model. The velocity profile for this flow model was originally not given by its proponents. However, it can be derived easily as in Eq. 3 in the

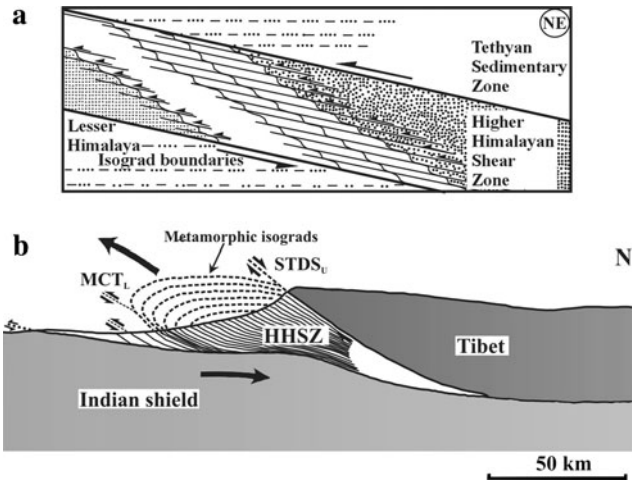

Fig. 14 **a** Idealized simple shear model of inverted metamorphism of the HHSZ, reproduced from Jain et al. (2002). The HHSZ is bounded by the Lesser Himalaya at the south and the Tethyan Sedimentary Zone in the north. Displacement of isograd boundaries within the HHSZ by a top-to-SW sense of simple shearing gives rise to inverted metamorphism and extrusion of the shear zone. **b** Channel flow model of extrusion of the HHSZ through its wedge-shaped geometry in Bhutan Himalaya. The parabolic velocity profile of extrusion gives rise to megascopic telescoping of the metamorphic isograds. *MCT$_L$* Main Central Thrust-Lower, *STDS$_U$* South Tibetan Detachment System-Upper. Subduction of the Indian shield below the Tibetan plate is shown by a *thick arrow*. Reproduced from Grujic et al. (1996). The terms 'MCT', 'South Tibetan Detachment Zone' and the 'Higher Himalayan Crystalline' in Grujic et al. (1996) are replaced with 'MCT$_L$' and 'STDS$_U$' of Godin et al. (2006) and 'HHSZ' of Jain and Anand (1988), respectively

"Appendix" (line 1 in Fig. 16a, b). The broad subdivision of the HHSZ into two rheological units (constraint I in "Constraints") was not tested in this model. The deformation has been idealized solely in terms of simple shearing, which keeps the pure shearing component of the HHSZ (constraint VIII in "Constraints") unexplained. Although a fluid mechanical theory of Couette flow (Schlichting and Gersten 1999) was implicit and the rocks of the HHSZ were considered to be of fluid character (constraint X in "Constraints"), the main shortcoming of this model lies in the fact that it cannot explain the extensional ductile shearing in the HHSZ (constraint IV in "Constraints"). Subsequently, conditions of the thickness, its variation, slip rates and possible synchrony of activation of the STDS$_U$ and the STDS$_L$ (constraint XI to XV and VII in "Constraints") also remain unexplained.

Channel flow model

During 'channel flow'/'Poiseuille flow', an incompressible Newtonian viscous fluid undergoes laminar flow through very long parallel horizontal static channel walls, due to a pressure gradient (curve 2 in Fig. 16a, Eq. 4 in "Appendix") giving rise to parabolic velocity profile. (Pai 1956). Grujic et al. (1996) used the same extrusion mechanism through a diverging upward approximately funnel-shaped HHSZ in the Bhutan Himalaya (Fig. 14b). Using numerical models, in a different tectonic setting, Koyi et al. (1999) showed that channel flow in the lower crust results in the formation of ductile shear zones with different senses of shearing. Application of the channel flow as different models of extrusion of the HHSZ has been summarized by Jessup et al. (2006).

In an ideal channel flow through parallel walls, the vertex of this profile is equidistant from the walls. A line passing through the vertex and parallel to the walls divide the channel into two zones of equal thickness with opposite senses of ductile shearing. Since the walls remain static, the fluid extrudes essentially in a simple shearing mode (constraint VIII in "Constraints"). Intersection between parabolically regionally telescoped isograds with the topography leads to an inverted metamorphism (constraint IX in "Constraints") followed by a normal sequence of isograds in the HHSZ. The rate of extrusion increases across the channel from zero at one of the walls, attains the maximum value at the middle of the channel, and drops symmetrically to zero at the other wall. Ductile shear strain at any instant is zero on the line equidistant from the walls, and increases symmetrically towards both the walls. The channel flow mode of extrusion of partially molten rocks was considered to initiate at 34 Ma in the sub-horizontal channel at $\sim$30 km depth (Beaumont et al. 2001), which therefore took 10 Ma to arrive the surface around 24 Ma. Considering the HHSZ dips at an angle of 30° (Figure 2b of Vannay and Grasemann 2001), the partially molten material is calculated to travel at least 50–60 km during extrusion. This in turn would indicate the modeled velocity of extrusion to be 5–6 km Ma^{-1}.

The channel flow model is fluid mechanical and represents the ductile deformation or flow behaviour of the HHSZ (constraint X in "Constraints"). Considering a southwestward flow of the rocks in the northeasterly dipping straight foliations of the HHSZ (constraint II in "Constraints"), the model produces a zone of top-to-NE sense of shearing characteristic of the STDS$_U$ simultaneously with the ongoing compressional shearing in the MCT$_L$ (constraint VII in "Constraints"). The model alone fails to explain the early phase of a top-to-SW sense of ductile shearing in the STDS$_U$ (constraints III in "Constraints"). The model does not utilize the rheologic division of the HHSZ prevalent during its ductile extrusion and extensional shearing (constraint I in "Constraints"). Contrary to constraint XI in "Constraints", the channel flow model generates a STDS$_U$ of equal thickness as that of the remainder of the HHSZ. Further, the same velocities of flow are produced near the MCT$_L$ and inside the STDS$_U$ at points that are equidistant from the nearest respective boundaries of the shear zone/channel (curve 2 in

Fig. 16a). Thus, a faster rate of extrusion in the $STDS_U$ compared to that near the MCT_L at any specific instant of ductile deformation of the HHSZ (constraint XV in "Constraints") remains unexplained.

For an increase or a decrease in the pressure gradient, the vertex of the parabolic profile attains a higher or a lower velocity, respectively. On other hand, with any increase or decrease in the viscosity of the rocks, the degree of tapering of the parabolic profile is modified. In these two possible cases, the vertex remains equidistant from the channel walls. For a specific thickness of the HHSZ, therefore, variation in the thickness of the $STDS_U$ over local- and regional scales (constraint XIII in "Constraints") cannot be explained by deviation in the magnitudes of flow parameters viz. the viscosity of fluid and the pressure gradient guiding the flow. From the structural point of view, the most critical drawback of the classical channel flow model in the context of the Sutlej section of the HHSZ is that it cannot explain the presence of an extensional shear zone inside the HHSZ, i.e. the $STDS_L$ (partly constraint IV in "Constraints"). Subsequently the constraint of its thickness (constraints XI and XII in "Constraints") and occasional absence in some Himalayan sections (constraint XIV in "Constraints") also remain unexplained.

General shear model

The 'general shear model' involves a combination of pure shear and a top-to-SW sense of simple shear of the HHSZ as its extrusion mechanism (Vannay and Grasemann 2001) considering the shear zone to be a rectangle of long but finite length. The fundamental parameters that guide the velocity profile of the general shear are (1) the location of the marker inside the rectangle; (2) the time elapsed after the deformation initiated; (3) the velocities of pure shear (Fig. 15a) and the simple shear of a pair of parallel boundaries defining the rectangle; (4) the length and (5) the breadth of the rectangle (Eq. 13 in "Appendix").

The 'general shear model' (Fig. 15b) of extrusion of the HHSZ takes into account a component of pure shear (constraint VIII in "Constraints") reported usually from the middle of the HHSZ noted in few sections by Bhattacharya (1981, 1999); Grasemann et al. (1999); Law et al. (2004); Jessup et al. (2006); Carosi et al. (2007); Cottle et al. (2007) and Larson and Godin (2009). Considering a NE–SW oriented rectangular HHSZ, the model involves post-metamorphic general shearing of the hinterland dipping isograds giving rise to gradual thinning and extrusion of the shear zone, inverted metamorphism (constraint IX in "Constraints"), northeast dipping straight foliation planes (constraint II in "Constraints") and formation of an extensional ductile shear zone within the top of the HHSZ as the $STDS_U$ (partly constraint IV in "Constraints").

In this model $STDS_U$, the extensional slip takes place at a higher rate than the remainder of the shear zone (constraint XV in "Constraints") simultaneous with the ductile thrusting of the MCT_L (constraint VII in "Constraints"). The model $STDS_U$ is thinner than the remainder of the HHSZ (partly constraint XI in "Constraints"). The model takes care of the fluid flow behaviour of the HHSZ (constraint X in "Constraints") since the shear zone is considered to be an incompressible Newtonian viscous fluid. Although not stated by Vannay and Grasemann (2001), the algebraic handing

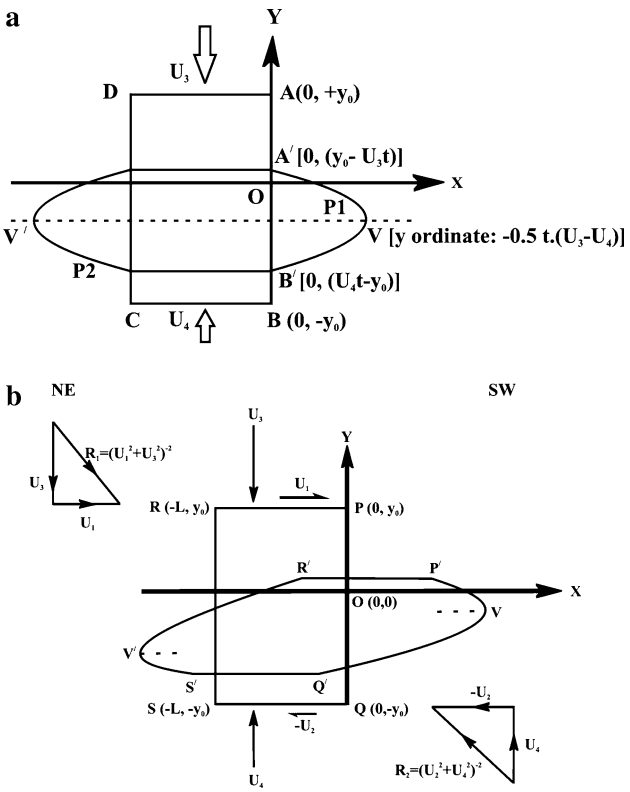

Fig. 15 **a** Pure shear deformation of the rectangle ABCD. Side DA is oriented NE–SW. Walls AD and BC are compressed with velocities U_3 and U_4, respectively. The y-axis is coincident with AB and the x-axis is parallel to and equidistant from AD and BC. Lengths AB = $2y_0$; BC = L. On pure shear, parabolic velocity profiles P1 and P2 with vertices V and V′, respectively, are produced whereby A and B reach A′and B′. **b** General shear deformation of the rectangle PQSR of incompressible Newtonian rheology and viscosity μ. Side RP is oriented NE–SW. Lengths PQ = $2y_0$; PR = L. A NE–SW geographic direction is assigned. The y-axis is selected coincident with PQ. The x-axis is chosen parallel to and equidistant from PR and QS. Wall PR undergoes simple shear and pure shear with velocities U_1 and U_3, respectively. Wall SQ undergoes these shears with velocities U_2 and U_4, respectively. $U_1 > U_2$ and $U_3 > U_4$ are considered. U_1 and U_2 define a top-to-SW sense of shear. The walls PR and QS have resultant velocities $R_1 = (U_1^2 + U_3^2)^{-2}$ and $R_2 = (U_2^2 + U_4^2)^{-2}$ and move at angles $\tan^{-1}(U_3\ U_1^{-1})$ and $\tan^{-1}(U_4\ U_2^{-1})$ to their lengths. PR and SQ move to P′R′and S′Q′. V and V′ are the vertices of the parabolic velocity profiles of the deformed rectangle at boundaries P′Q′and R′S′

of the velocity profile of general shearing shows that the $STDS_U$ can be absent in some Himalayan sections as a result of special combination of parameters guiding the flow (Eq. 16 in "Appendix"). Further, a variation in one or many flow parameters in Eq. 15 in "Appendix" can explain the variable thickness of the $STDS_U$ in different scales (constraint XIII in "Constraints").

However, the general shear model does not utilize the classification of the HHSZ into two lithologies in the Sutlej section (constraint I in "Constraints"). Besides, it cannot explain (1) the preexisting top-to-SW sense of ductile shearing throughout the HHSZ including the $STDS_U$ (constraint III in "Constraints"); and (2) the occurrence of the $STDS_L$ inside the HHSZ (party constraint IV in "Constraints"). As a result, the constraint on the thickness and occasional absence of the $STDS_L$ in some Himalayan sections (constraints XI, XII and XIV in "Constraints") also remain unexplained.

A new extrusion mechanism

Proposition

To satisfy all the constrains listed in "Constraints", the following analytical model based on the solution of a simplified form of the Navier–Stokes equation (Eq. 1 in the "Appendix") at geologically realistic physical boundary conditions is proposed as the mechanism of extrusion within the ductile regime for the Sutlej section of the HHSZ. The MCT_L and the top wall of the HHSZ/$STDS_U$ are considered parallel walls of a very long master channel filled with a Newtonian viscous fluid (constraint X in "Constraints"). Without using constraint I in "Constraints" about the two-layer division of the HHSZ prevalent during extrusion, the proposed model can aptly explain all other tectonic constraints. The presented model involves different combinations of simple shear, pure shear, and channel flow and the temporally shifting extrusion in different parts of the HHSZ (Fig. 17), and is henceforth referred as the 'shifting combined flow model'. The pure shear component (constraint VIII in "Constraints") is not introduced into the derivation of the velocity profile as it alone cannot explain the other constraints of extrusion of the HHSZ. In the model, flow lines and the inactive marker are comparable with the primary shear planes and shear fabrics, respectively. Ductile slip along individual shear planes throughout the HHSZ has been utilized in developing the model, which is, therefore, distinctly different from the channel flow mode of extrusion by tectonic inversion of the HHSZ as a 'coherent block' as recently proposed by Dasgupta et al. (2009), possibly a result of extrusion of rocks with non-Newtonian rheology through a channel with parallel-sided walls, from the Sikkim Himalaya.

In a very slow laminar extrusion flow mode, the flow lines comparable with the main foliations essentially remain straight and parallel during the extrusion process. Considering the channel to dip to the northeast and a southwestward extrusion constraint II in "Constraints" about the parallelism and dip direction of the shear planes of the HHSZ are obeyed. The consideration of rheology of real rocks as Newtonian fluids is certainly an approximation (Ramsay and Lisle 2000), but has previously been adopted in similar tectonic modeling to explain the first order tectonic constraints of the HHSZ (e.g. Beaumont et al. 2001). The fluid inside the channel, an analogue to the rocks of the HHSZ, is considered to be incompressible. In other words, the kinematic effects of dilatancy due to partial melting (Grasemann et al. 2006) within 19–14 Ma in the upper parts of the HHSZ (Godin et al. 2006) are neglected.

The shifting combined flow model is divided into two main phases: $E = E_1 + E_{2a} + E_{2b}$. These phases are explained using minimum but the most crucial flow parameters that explain the extrusion. These are (1) a pressure gradient component, (2) the relative rate of slip on the boundaries-, (3) the viscosity of the rocks-, and (4) the thickness of the HHSZ. While the E_1-phase utilizes the second- and the fourth parameter only, the E_2-pulses use all of them. The choice of minimum number of parameters here is in contrast to the classical channel flow model proposed and developed by the Dalhousie research group (e.g. Beaumont et al. 2001, 2004; Jamieson et al. 2004) that involves input of additional parameters such as density-, thermal conductivity, and the rate of erosion of the extruding rocks. However, those parameters do not have any direct relation with the first order constraints of extrusion (Grasemann et al. 2006).

The E_1-phase: (line 1 in Fig. 16a, b) An upper sub-channel of the HHSZ delimited by the MCT_U at the base and the top of the HHSZ underwent a top-to-SW sense of ductile simple shearing during 25–19 Ma. The timing is bracketed between the initiation of activities of the compressional ductile shearing of the MCT_U and that of the extensional ductile shearing of the $STDS_U$ as mentioned by Godin et al. (2006). The extrusion phase is represented by a linear velocity profile (Eq. 3 in "Appendix"). The sense of shearing and the ductile shear strain at any instant inside the sub-channel remain the same. The velocity of different layers within the sub-channel decreases linearly from the top- to the bottom wall.

We consider two possibilities for the E_1-phase as follows. The top-to-SW sense of shearing in the upper sub-channel can be generated either by (1) absolute movements of the top of the HHSZ and the MCT_U towards SW and NE, respectively (line 1 in Fig. 16a), or (2) both the boundaries move southwestward but the former with a higher velocity (line 1 in Fig. 16b). In the first case, a

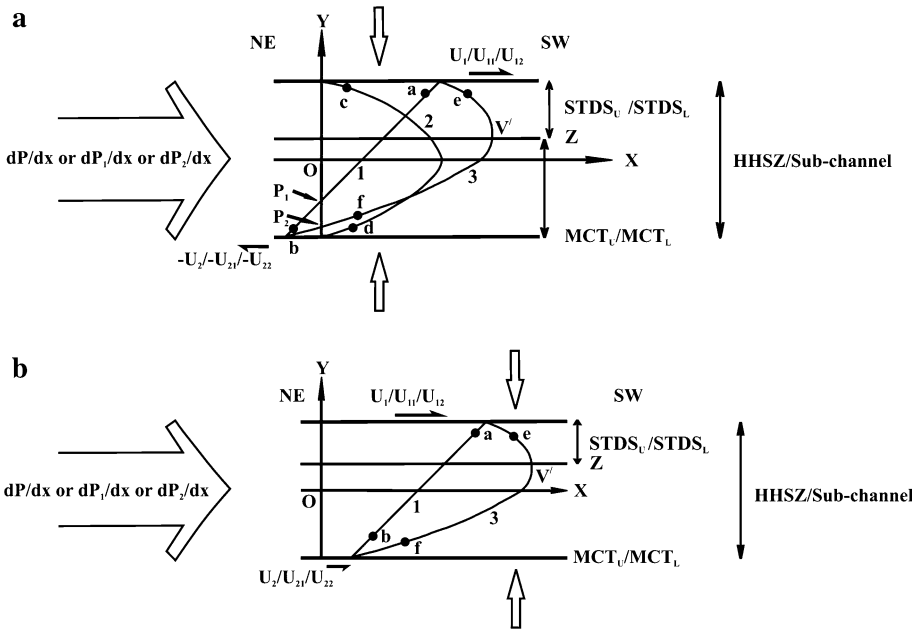

Fig. 16 A channel with NE–SW oriented long parallel walls consisting of an incompressible Newtonian viscous fluid is considered. The *x*-axis is parallel to and equidistant from the walls. An inactive marker was coincident with the *y*-axis at the onset of flow. **a** shows simple shearing achieved by absolute movement of the top- and the bottom walls/boundaries of the flow zone towards southwest and northeast, respectively. **b** shows movement of both the walls towards southwest but the former with a higher velocity. In these figures, *Line 1* Velocity profile of simple shearing in the E_1-phase within the top sub-channel defined by the top of the now $STDS_U$ and the bottom wall MCT_U. The boundaries are sheared with velocities U_1 and U_2 and no pressure gradient acts. Equation 3 in ''Appendix'' represents this profile. For static walls and solely a pressure gradient induced flow, the profile is the parabola 2. Equation 4 in ''Appendix'' represents this profile. *Parabola-3* velocity profiles for the E_{2a}- and the E_{2b}-pulses (The spatial positions of these pulses in the HHSZ are distinctly shown in Fig. 17). In the E_{2a}-pulse, the flow components (dP_1/dx), U_{11}, U_{21} and pure shear act in the HHSZ bounded by the MCT_L and the top of the now $STDS_U$. The pressure gradient and the pure shear are shown by *open*- and *close arrows*, respectively. Pure shear acted only in the E_{2a}-pulse. Equation 17 in "Appendix" represents the profile of combined simple shear and channel flow excluding the pure shear. In the E_{2b}-pulse, the flow components (dP_2/dx), U_{12} and U_{22} act within the lower sub-channel bounded by the MCT_L and the top of the now $STDS_L$. Equation 19 in "Appendix" represents this profile. *V′* vertex of parabola-3, located within the upper part of the channel. *Z*: a line passing through *V′* and parallel to the walls demarcates the lower boundary of the $STDS_U$/$STDS_L$. In **a**, pivot points P_1 and P_2 are intersection between the *y*-axis and line-1 and parabola-3, respectively. In **b,** these points do not exist. The marker remains attached at these points while getting progressively deformed during successive phases. For both the figures, for line-1 any point *a* near the top of the channel extrudes faster than the location *b* near the bottom. For parabola-2, the points equidistant from the walls, *c* and *d*, extrude with the same rate. For parabola-3, any point *e* within the model $STDS_U$ or the $STDS_L$ extrudes at a higher rate than any point *f* near the MCT_L. MCT_U Main Central Thrust-Upper, MCT_L Main Central Thrust-Lower, $STDS_U$ South Tibetan Detachment System-Upper, $STDS_L$ South Tibetan Detachment System-Lower, *HHSZ* Higher Himalayan Shear Zone. Not to scale

pivotal point exists (see expression after Eq. 3 in "Appendix") across which any imaginary marker initially non-parallel to the MCT_U keeps rotating during progressive simple shearing. The position of this pivot depends on the absolute velocity of the walls and the thickness of the channel. However, the pivot does not exist in the second case. During the E_1-phase of extrusion, the $STDS_U$ characterized by a top-to-NE shear sense was not produced within the top of the HHSZ. The E_1-phase takes into account the extrusion of the upper part of the HHSZ since 25 Ma, beginning of the Himalayan D_2 deformation phase of Jain et al. (2002) and Vannay and Grasemann (2001) and development of shear sense indicators with a consistent top-to-SW shearing (Fig. 19a, constraint III in "Constraints"). In one way, the E_1-phase is the mathematical representation of the simple shear model of Jain and Manickavasagam (1993) and Hubbard (1996).

The E_2-phase: (curve 3 in Figs. 16a, b, 17) During this phase of extrusion, viscosities of the rocks constituting the HHSZ were significantly reduced and extruded southwestward like a fluid by a combination of a pressure gradient (channel flow/Poiseuille flow) and a top-to-SW sense of shearing. The flow during the E_2-phase took place in two spatially restricted pulses that gave rise to the two strands of the South Tibetan Detachment System consecutively (Eqs. 17, 19 in "Appendix"). The first E_{2a}-pulse occupied the whole of the HHSZ, i.e. from MCT_L up to the top of the HHSZ. Pure shearing produced by relative movement of the $STDS_U$ and the MCT_L towards each other (constraint VIII in "Constraints") took place most probably during this

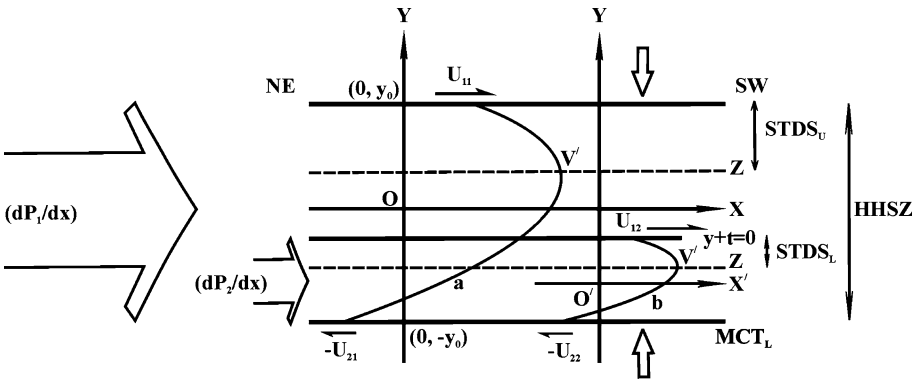

Fig. 17 The spatial occurrences of the E_{2a}- and the E_{2b}-pulses are shown inside the HHSZ considered to be of long parallel NE-SW oriented walls. Symbols and the coordinate axes are as per Fig. 16. Additionally, a and b stand for profiles of the E_{2a}- and the E_{2b}-pulses. The line $y + t = 0$ is taken as the top boundary of the $STDS_L$. To construe the velocity profile b, the *X*-axis is shifted to *X*′equidistant from the lines $y + y_0 = 0$ and $y + t = 0$. *Close arrows* represent the pure shear component prevalent during the E_{2a}-pulse

pulse. This merely accentuated the parabolic velocity profile created by combined simple shear and the channel flow. The second E_{2b} pulse was restricted within a lower sub-channel of the HHSZ bounded by the MCT_L at the bottom- and the top of the now $STDS_L$ as the upper boundary. A generalized situation of different magnitudes of simple shear velocities and pressure gradients are considered for the two pulses. It is noteworthy that where exists only the $STDS_U$ i.e. a single extensional detachment, Mukherjee and Koyi's (2009b) model of combined simple shear and channel flow in a single pulse can be a satisfactory explanation of the extrusion of the HHSZ.

Both the pulses of the E_2-phase are represented by parabolic velocity profiles. Apart from pure shear, the profiles created by a combined simple shear and channel flow are vector additions of the constituent flow components (concluded from Eqs. 3, 4, 17 in "Appendix"). The vertices of the profiles in successive pulses are located within the upper half of the respective flow zones. Across the lines passing through these vertices and parallel to the MCT_L, the senses of ductile shearing are opposite. These lines define the lower boundaries of the $STDS_U$ and the $STDS_L$, respectively. Below and above these lines lie the zones of top-to-SW compressional and the top-to-NE extensional shearing, respectively. The lower strand of the extensional ductile shear zone, i.e. the $STDS_L$, came into existence during the E_{2b}-pulse.

Outside the two strands of the detachment, the remainder of the HHSZ and the lower sub-channel in respective pulses underwent dominantly a top-to-SW sense of simple shearing in conjunction with a pressure gradient. This compressional shearing is a continuation of the D_2 deformation phase of Vannay and Grasemann (2001) and Jain et al. (2002). The boundaries that demarcate the two shear senses, i.e. the lower boundaries of the two detachments, need not be lithologic discontinuities. The E_{2b}-pulse necessitates that the upper boundary of the $STDS_L$ acted as a tectonic plane and a southwestward shearing was achieved on it and the MCT_L independently of the remainder of the HHSZ. Under simultaneity of simple shear and channel flow, the simulated $STDS_U$ and the $STDS_L$ are thinner than that of the whole of the HHSZ (Eqs. 22, 23 and onwards in the "Appendix"; constraint XI in "Constraints"). Had there been only a channel flow in the two sub-channels, ductile extensional shear zones of equal thicknesses with those of the ductile compressional shear zones in the remainder of the sub-channels would have been produced- which are not the natural situations (see "Constraints").

The rationale of choosing (1) pulsed flows and (2) pure shear restricted only in the E_{2a}- pulse are as follows; (1) Simultaneous extensional ductile shearing in the $STDS_U$ and the $STDS_L$ is kinematically implausible even though compiled geochronologic data by Godin et al. (2006) indicated such a possibility between 19 and 14 Ma (constraint VII in "Constraints"). Negative results were obtained in this work in a number of analytical- ("Possibility I" and "Possibility II") and analogue models ("Possibility III") to check whether two extensional shear zones can be produced concurrently in the HHSZ with parallel and diverging upward walls and with a single or a two-layer lithology. (2) Had there been a pure shear component along with the E_1-phase, i.e. a general shearing (Fig. 15b) to take place, an $STDS_U$ would have been produced but the early top-to-SW sense of shearing inside it (constraint III in "Constraints") would remain unexplained. On other hand, if the pure shear component had acted only in the lower sub-channel defined by the MCT_L at the base and the now $STDS_L$ as the upper boundary during the E_{2b}-pulse, a void would have been created northeast at the upper boundary of the present $STDS_L$ (Fig. 18 and its caption), which cannot be a natural case.

The proposed model considers the MCT_U as a major tectonic discontinuity in the HHSZ northeast of which the extrusion of the E_1-phase was confined. This is in

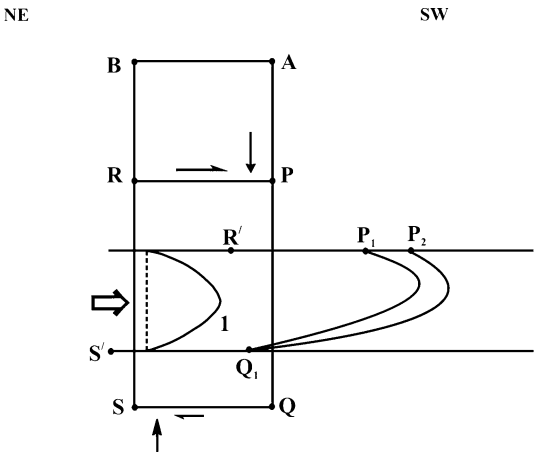

Fig. 18 A rectangle BAQS is considered as the model Higher Himalayan Shear Zone (HHSZ). Along with other flow mechanisms, whether a component of pure shear can act in a sub-zone in the HHSZ is addressed. The rectangle PRSQ defines the lower sub-channel with SQ as the MCT_L and RP as the top of the now $STDS_L$. On simple- and pure shear on SQ and RP, side PQ turns into a parabola P_1Q_1. A further component of channel flow shown by the parabolic profile *1* and the *solid arrow* makes the resultant parabolic profile P_2Q_1.Such a flow mechanism is implausible as nature will not permit the space created between the boundaries RP and $R'P_2$. Neither to scale nor angle

conformity with the disparity in geochemical parameters across the MCT_U (their Vaikrita Thrust) as compiled by Chambers et al. (2008) and their proposition that across it, the HHSZ was decoupled during extrusion. The absolute timing of the two pulses can be estimated by keeping in mind (1) the ductile extensional shearing in the $STDS_L$ and the $STDS_U$ cannot form contemporaneously, and (2) Godin et al.'s (2006) compiled data on timing of the MCT_L, the MCT_U, the $STDS_L$ and the $STDS_U$ reframed here as constraint VII in "Constraints". These imply that a simultaneous activation of the extensional ductile shearing in the $STDS_U$ and the $STDS_L$ between 19 and 14 Ma is kinematically not possible. A second point to note is that the proposed model considers the extrusion of the HHSZ in sequences—first in the upper part followed by the whole of the shear zone, and finally the lower part. Therefore, the deformation did not simply migrate southward. Thirdly, a top-to-SW sense of ductile shearing between the MCT_U and the $STDS_U$ took place in the E_1-phase and the E_{2a}-pulse; and that between the MCT_U and the MCT_L in the E_{2a}-and the E_{2a}-pulses. This means that the prior top-to-SW shearing was prevalent for a longer duration than the top-to-NE sense of ductile shearing in the $STDS_U$ and the $STDS_L$.

The E_{2a}-pulse took place throughout the HHSZ most probably between 15 and 14 Ma, which is the timing of simultaneous activation of the MCT_L and the $STDS_U$. This was followed by the E_{2b}-pulse within the sub-channel, with a probable duration twice as long as the previous one between 14 and 12 Ma. This time range is the period of overlapping activity of the MCT_L and the $STDS_L$. Interestingly, channel flow in pulses has already been proposed from few sections of the HHSZ. For example, based on cathodoluminescence imaging and U–Pb dating of zircons of the Bhagirathi valley of the HHSZ, Jain et al. (2005a) and Singh et al. (2005) proposed a channel flow extrusion of the shear zone in two pulses- around 46 and 20 Ma, respectively. However, these authors did not corroborate their findings in terms of structural constraints and spatial extent of these pulses. On the other hand, Hollister and Grujic (2006), backed with structural and thermobarometric constraints, proposed the extrusion of the HHSZ in the Bhutan Himalaya in three pulses: between 22–16, 16–13, and 12–10 Ma in spatially restricted zones. Since the velocity profiles of these pulsed extrusions are depicted (their Figure 5) to be parabolas with vertices at the middle of the respective channels, the boundaries of the channels have been considered implicitly as static. On contrary, not only of different timings of individual phases, our model considers an extrusion mechanism where the boundaries of the respective channels are in absolute motion in addition to a pressure gradient induced channel flow during the E_2-phase.

During the E_2-phase, had the pressure gradient component acted along with the first flow possibility of the E_1-phase, i.e. movement of the top and the bottom walls of the HHSZ in opposite directions, pivotal points should exist for both the E_{2a}- and the E_{2b}-pulses (curve 3 in Fig. 16a). Across these pivots, any imaginary inactive marker initially non-parallel to the walls of the shear zone/channel keeps deforming into progressively tapering parabolas. However, the pivot would not exist if the pressure gradient component characteristic of the E_2-pulses had acted along with the second flow case of the E_1-phase where both the boundary walls of the HHSZ move southwestward (curve 3 in Fig. 16b). With the uncertainty in the direction of absolute movement of the walls of the HHSZ, a search for the location of pivots in the shear zone for the E_1- and the two pulses of the E_2-phase would not be a useful exercise.

In order to generate a top-to-SW sense of shearing, the two possible extrusion cases of the E_1-phase intrinsically assume that the upper part of the HHSZ extruded at a faster rate than the bottom part (line 1 in Fig. 16a, b). The top part of the HHSZ continued to extrude more rapidly (constraint XV in "Constraints) during the E_{2a}-pulse. During the E_{2a}- and the E_{2b}-pulses in the E_2-phase, both the top- and the bottom boundaries of the $STDS_U$ and the $STDS_L$, respectively, underwent southwestward movement parallel to themselves. Their bottom boundaries moved at higher velocities (U_3, see explanation after Eq. 17 in "Appendix") than the upper boundaries during respective pulses. This would give rise to a bulk southwestward extrusion vis-à-vis a perceptible top-to-NE sense of shearing in the $STDS_U$ and the $STDS_L$ (Fig. 19b, c,

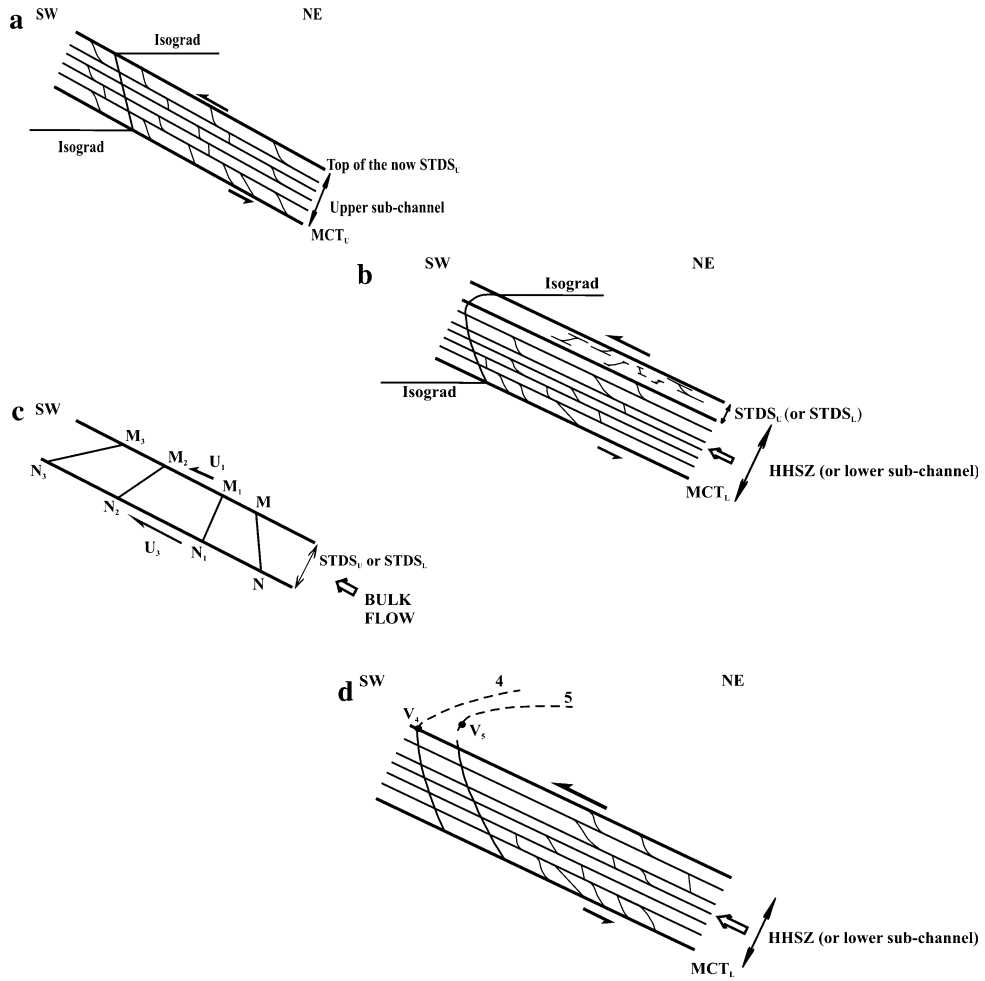

Fig. 19 Structural and metamorphic significance of the proposed extrusion phases and pulses. **a** The E_1-phase of extrusion of the upper sub-channel is confined within the MCT_U as the base and the top of the now $STDS_U$ as the upper boundary. The northeasterly dipping sub-channel demonstrates a consistent top-to-SW sense of ductile shearing as represented by the S–C fabric. The isograds are regionally kinked in a top-to-SW sense giving rise to inverted metamorphism. **b** The E_{2a}- and the E_{2b}-pulses inside the northeasterly dipping parallel walls of the HHSZ and the lower subchannel, respectively. The HHSZ is defined within the MCT_L and the top of the $STDS_U$. The lower sub-channel is defined within the MCT_L and the top of the $STDS_L$. The flow zones undergo simple shearing in a top-to-SW sense in conjunction with a pressure gradient. The isograds are deformed into parabolas inside the shear zone similar to the velocity profile giving rise to inverted metamorphism—shown by a single isograd. A top-to-NE sense of ductile shearing is produced within the $STDS_U$ and the $STDS_L$ in the two respective pulses. The remainder of the HHSZ undergoes a consistent top-to-SW sense of ductile shearing. Different senses of shearing are represented by S–C fabrics. The top-to SW sense of shearing produced during the E_1-phase occur less in numbers in the $STDS_L$ and $STDS_U$ as relics. **c** Reorientation of a ductile shear fabric MN within the $STDS_U$ (and the $STDS_L$) in the E_{2a}- (and the E_{2b}-) pulses, respectively. As a result of the previous E_1-phase (and the E_{2a}-pulse), the fabric MN achieved a top-to-SW orientation. When the E_{2a} (and the E_{2b}-) pulses happened, the lower boundary of the $STDS_U$ (and the $STDS_L$) moved with a velocity U_3 higher than their upper boundaries. A bulk southwestward flow reoriented the fabric into M_1N_1, into M_2N_2 and finally into M_3N_3. This gave rise to a top-to-NE sense of shearing at the final M_3N_3 orientation. **d** Two special cases of the E_{2a}- and the E_{2b}-pulses in a northeasterly dipping parallel wall channel compared with the HHSZ and the lower sub-channel in two considerations. The base of the channel in both the pulses is defined by the MCT_L. Profiles 4 and -5 are extrapolated outside the flow zones as dashed lines in order to show that they are parabolas. Their vertices 'V_4' and 'V_5' lie on the upper boundary and outside the flow zones, respectively. In these situations, a consistent top-to-SW sense of ductile shearing persists and is manifested by S–C fabric and other shear sense indicators. No extensional ductile shear zones are produced. The pressure gradient and the simple shear are shown by hollow arrows and a pairs of half arrows, respectively. Symbols: *HHSZ* Higher Himalayan Shear Zone, MCT_U Main Central Thrust-Upper; MCT_L Main Central Thrust-Lower; $STDS_U$ South Tibetan Detachment System-Upper; $STDS_L$ South Tibetan Detachment System-Lower. Neither to scale nor angle

constraint IV in "Constraints"). As a result, while many shear fabrics were produced showing a top-to-NE sense of ductile shearing in the $STDS_U$ (Figs. 5a, b, d, 7a–c) and the $STDS_L$ (Figs. 6a, b, 8a), most of the early fabrics indicative of a top-to-SW sense were destroyed and very few escaped the retro-shear along the same C-planes (Figs. 5c, 6c, d, 8b) possibly due to strain partitioning and survived as remnants. Taking different magnitudes of the flow

parameters, an $STDS_L$ thinner than that of the $STDS_U$ can also be explained (constraint XII in "Constraints", see after Eq. 25 in "Appendix").

According to the proposed extrusion model, the thickness of both the $STDS_U$ and the $STDS_L$ are dependent on all the four flow parameters that define the respective velocity profiles (Eqs. 20, 21 in "Appendix"). The domain within which the E_{2b}-pulse was confined was thinner than that of the E_{2a}-pulse. The two pulses of the E_2-phase had a total span of 3 Ma from 15 to 12 Ma. The geographic extent of the activation of the E_2-phase is also expected to be quite large within the HHSZ along the entire trend of the Himalaya (see Beaumont et al. 2006). Over such a wide spatial- and temporal extent, the flow parameters varied as follows. (1) *The pressure gradient* giving rise to the Poiseuille flow mode of extrusion used to be 3.5 kbar km^{-1} (Searle 1999) and 0.28 ± 0.17 kbar km^{-1} (Searle et al. 1992), 0.2885 kbar km^{-1} (Walker et al. 2001) in the Zanskar Himalaya or 0.27 kbar km^{-1} on average (Vannay et al. 2004). The later value is same as that given from the Nepalese Himalaya by Hodges et al. (1988), ~0.33 kbar km^{-1} during the proposed shifting combined flow between 16 and 13 Ma (Hollister and Grujic 2006), or 0.3 ± 0.08 kbar km^{-1} in the Langtang valley (Fraser et al. 2000) and ~0.06 MPa km^{-1} in the Marsyandi valley (Catlos et al. 2001) in Nepal. In contrast, about ten times higher amount of 1–2 kbar km^{-1} (Grujic et al. 2002) or a still higher magnitude of 3.71 kbar km^{-1} in the footwall of the ZSZ (Walker et al. 1999), 5–6 kbar km^{-1} at the base of the HHSZ in the Nepal Himalaya within the MCT_L and the MCT_U (Kohn 2008), and 6 kbar km^{-1} in the footwall of the MCT_U in central Nepal (author's MCT, Catlos 2000) have also been reported. (2) *The viscosity* of the partially molten rock at a mid-crustal depth, now extruded at the surface, was ~10^{19} Pa s (Jamieson et al. 2004); but that of the molten granite alone extruded in a prodigious proportion in the upper part of the HHSZ could had been as low as 10^5–10^{12} Pa s (Druguet and Carreras 2006 and references therein) or $10^{4.5}$ Pa s (Scaillet et al. 1996). Further, the viscosity of the molten rock is expected to temporally increase due to progressive reduction in its temperature as it keeps extruding to shallower crustal levels. (3) *The rate of slip on the boundaries of the HHSZ*: the slip rate of the MCT_L and the MCT_U in different sections ranged from few millimeter per year, e.g. 1.2 mm $year^{-1}$ (Valdiya 2001), 3–5 mm $year^{-1}$ (Yin 2006), up to an exceedingly slow rate of 0.8 mm $year^{-1}$ in the Nepal Himalaya (Wobus et al. 2005). (4) *The thickness of the HHSZ*: in different sections, the thickness and varies from 6 km as the lowest reported value (Lombardo et al. 1993) to a maximum of 50 km (Jain and Anand 1988). A temporal variation in the magnitudes of the flow parameters as discussed above could give rise to a disparity in the thickness of the $STDS_U$ and in its continuation in other sections of the Himalaya (constraint XIII in "Constraints").

For certain combinations of magnitudes of the flow parameters governing the E_{2b}-pulse, the vertex of the parabolic profile may touch the upper boundary of the sub-channel or may even plot outside the shear zone (curve 4 or -5 in Fig. 19d, Eq. 25 in the "Appendix"). In both these cases, the lower sub-channel should demonstrate a uniform top-to-SW sense of ductile shearing and no $STDS_L$ is produced even if a pressure gradient is active. The situation, therefore, is structurally equivalent to the previous E_1-phase where no ductile extensional shear zone is produced. Thus, a continuation of the $STDS_L$ might be lacking in some sections of the HHSZ even if a pressure gradient drives the extrusion along with the simple shearing of the walls (constraint XIV in "Constraints"). To check whether such an extrusion mechanism was active in any Himalayan sections lacking the $STDS_L$, the following points are to be satisfied within the specified 14–12 Ma time range: (a) the ductile shear strain within the HHSZ has to keep decreasing from the MCT_L towards north; and (b) the rate of extrusion should keep increasing from the MCT_L towards north.

The effectiveness of simple shearing of isograds on the millimeter-scale along the C-planes in giving rise to their cumulative displacement on the order of tens of kilometers or so on the regional scale and subsequent inverted metamorphism has previously been explained texturally from the Zanskar section of the HHSZ by Jain and Manickavasagam (1993) and analytically by Grasemann and Vanney (1999). A similar extrusion mechanism considering the isograds to be inactive markers has also been visualized in terms of regionally telescoped isograds from the Zanskar section (Stephenson et al. 2001) and from Bhutan Himalaya (Grujic et al. 1996).

As revealed in the present micro-structural studies of the two strands of the STDS such as the $STDS_L$, the porphyroblastic index minerals of high-grade metamorphism such as garnet were affected by a top-to-NE sense of ductile extensional shearing (Fig. 7b, c). Jain et al. (2002) made similar micro-structural observations on sheared staurolite, kyanite and sillimanite porphyroblasts from high-grade rocks in the $STDS_U$ in the Zanskar section locally designated as the Zanskar Shear Zone. These observations are interpreted as: (1) the higher grade metamorphism in the $STDS_U$ and the $STDS_L$ that gave rise to garnet, staurolite, kyanite, silliminite etc. took place either prior to or coeval with the top-to-NE sense of shearing; and (2) isograds in the $STDS_U$ and the $STDS_L$, therefore throughout the HHSZ, were further deformed as a result of the E_2-pulses of extrusion in addition to that in the previous E_1-phase. We propose that the isograds were deformed similar to the velocity profiles of the respective phases of extrusion as inactive markers, i.e. they were first

sheared in a top-to-SW sense giving rise to inverted metamorphism from the MCT_U up to the top of the HHSZ during the E_1-phase around 25 Ma (Fig. 19a). These isograds were modified into parabolas during the subsequent E_2 pulses (Fig. 19b).

Different phases of brittle deformation events, assumed to be younger than the E_{2b}-pulse $\sim$12 Ma, signals the cessation of the ductile deformation as the hot partially molten HHSZ rocks crossed the brittle–ductile regime, possibly at 8 km depth (Davis and Reynolds 1996), and entered the brittle deformation regime. The pressure gradient responsible for the fluid flow behaviour of the HHSZ of the E_2-pulses died down near this interface. However, the oldest record of the top-to-SW sense of ductile shearing component that was active since $\sim$25 Ma, still continued in terms of brittle shearing along the pre-existing primary ductile shear planes. This is revealed by duplexes at meso- and micro-scales (Figs. 11a–d, 12a–d) along the brittle shear Y-planes the same as those of the previously formed ductile C-planes. This brittle shearing event might have augmented the ductilely extruded rocks of the HHSZ to arrive at a still shallower crustal depth. A phase of brittle–ductile extension dislocated the litho-units to variable degrees giving rise to different morphologies of boudins (Fig. 10a–d) but probably did not enhance the extrusion process.

The timing of different phases of extrusion of the HHSZ as presented here may vary in other sections of the shear zone depending on the exact timing of activation of the four important tectonic zones viz. the MCT_L, the MCT_U, the $STDS_L$ and the $STDS_U$ at specific locations. On the other hand, if the timing of activation of all these zones come out from the Sutlej section in geochronologic studies in future, the timing of extrusion in this section will also need to be reassessed.

Predictions

While the presented combined flow model satisfies the constraints in "Constraints" except for the lithologic division of the HHSZ (constraint I) as discussed above, it makes the following conjectures.

Speculation 1: The ductile shear strain at any point inside the upper sub-channel defined by the MCT_U and the top of the $STDS_U$ at any instant during and at the end of the E_1-phase should be the same. This is because at any moment the angle between the marker and the shear planes (flow lines) remain the same throughout this sub-channel. However, this is not possible to check in the field since the extrusion phase was later overprinted by the E_2-pulses of extrusion with subsequent deformation giving rise to a spatial variation in the ductile shear strain.

Speculation 2: The ductile shear strain in the E_{2a}-pulse at any point on the velocity profile is defined by the 'tan' of the acute angle between the tangent at that point and its initial orientation as the *y*-axis. During and after the end of the E_{2a}-pulse, the shear strain is expected to be most intense at the boundaries of the HHSZ and keep decreasing towards the lower boundary of the $STDS_U$ passing between the locations Pangi and Kashang. However, the E_{2b}-pulse of the flow is expected to disturb this strain pattern.

Speculation-3: Since the E_{2b}-pulse took place for 2 Ma, a duration twice as that of the E_{2a}-pulse, shear strain in the lower sub-channel of the HHSZ, delimited by the MCT_L and the top of the $STDS_L$, is expected to be more intense than in the remainder of the HHSZ after the E_{2b}-pulse. Within this lower sub-channel, the shear strain is speculated to be most intense at its boundaries and keep decreasing towards the lower boundary of the $STDS_L$. Within the HHSZ, therefore, two prominent 'lows' of ductile shear strain are expected at the lower boundaries of the $STDS_U$ and the $STDS_L$. A high amount of simple shearing deciphered from the kinematic vorticity numbers at the boundaries of the HHSZ, 0.66–0.77 near the MCT_L in the lower Dolpo Range in the western Nepal, 0.67–0.98 in the $STDS_U$ in the Mt. Everest region; and the intermediate values inside the shear zone inside the shear zone, as mentioned earlier in "Tectonic constraints", broadly supports this prediction.

We note that, after the ductile extrusion had ceased, the angle between the S- and the C fabrics in the HHSZ would not necessarily show any systematic variation in a NE–SW transect. This is because the final angle between the two fabrics depends on (1) the angle between these two foliations before shearing took place; (2) whether the S-fabric is strain-sensitive or -insensitive (Davis and Reynolds 1996 and references therein); and (3) the probable strain localization within the shear zone. Therefore, unlike Martin et al. (2005), these angles are not measures of ductile shear strain, nor should their spatial variation be used to validate the proposed model.

Speculation 4: The parabolic velocity profiles characteristics of the E_2-pulses are also representations of the spatial variations of extrusion rates in the HHSZ. Thus, the E_{2a}-pulse envisages that the base of the $STDS_U$, passing between the localities Pangi and Kashang, extruded at the fastest rate, and that the extrusion rate kept decreasing towards its walls. In the E_{2b}-pulse, extrusion in the upper part of the channel stopped, but the sub-channel continued to extrude with the base of the $STDS_L$ at the highest rate. To check its validity, the rate of extrusion at a number of locations across the HHSZ when the E_1- and the E_2-phases were active is needed but is lacking in the Sutlej section. A similar data set with an average value of 1.4 ± 0.2 mm year^{-1} for the entire shear zone, deduced from the young apatite fission track ages, is available from the Sutlej section of the HHSZ (Thiede et al. 2004). However, the data

is not useful as a high rate of erosion of the shear zone has a strong control on it (Thiede et al. 2004).

Speculation 5: We recollect that the four parameters guiding the parabolic profiles in the E_2-pulses are (1) viscosity, (2) relative rate of slip on the walls, (3) thickness of the channel under consideration and (4) the pressure gradient. For specific sets of values of these parameters during the E_{2a}-pulse, the vertex of the parabolic profile touches the upper wall of the HHSZ or may be located outside the shear zone (curve 4 or 5 in Fig. 19d, Eq. 24 in "Appendix"). In both the flow situations, the HHSZ should demonstrate a uniform top-to-SW sense of ductile shearing and no $STDS_U$ is produced even if a component of channel flow is active. The situation is structurally equivalent to the previous E_1-phase where no extensional shear zone is produced. This means that a continuation of the $STDS_U$ might be lacking in some sections of the HHSZ even if a pressure gradient drives the extrusion along with the simple shearing of the walls. Therefore, if a continuation of an extensional ductile shear zone is not obtained within the top of the HHSZ at some section, it does not necessarily mean that the channel flow component was absent around 15–14 Ma.

To check whether such an extrusion mechanism was active in any section of HHSZ displaying a uniform top-to-SW sense of shearing and an absence of a ductile extensional shear zone, the following points are to be satisfied within the specified time range: (a) the ductile shear strain within the HHSZ has to keep falling from the MCT_L towards its upper wall; and (b) the rate of extrusion should keep increasing from the MCT_L towards its upper wall. An absence of the $STDS_U$ as speculated here is found in a part of the Kashmir Himalaya in India from Zanskar till the Nanga Parbat metamorphics. The available explanation is that the $STDS_U$ has been a blind structure there (Yin 2006 and references therein) although, this idea is not substantiated by any further evidences. If this part of the HHSZ can satisfy the two above mentioned points ('a' and 'b'), an alternate explanation of special combinations of the flow parameters leading to the absence of the $STDS_U$ could be exemplified.

Secondly, by a variation in the four flow parameters of the E_{2b}-pulse, it can be predicted that the $STDS_L$ varies in thickness along the Himalayan trend. This prediction is difficult to check as previous authors e.g. Edwards et al. (1996), Searle et al. (2003) and Law et al. (2004) who documented the $STDS_L$ from different Himalayan sections did not refer its thickness. The only available data of the thickness of the $STDS_L$ for the Sutlej section through this work is 1–1.4 km (Fig. 9).

Speculation 6: A top-to-SW followed by a top-to-NE sense of ductile shearing given by different shear fabrics in the $STDS_U$ and $STDS_L$ have been considered in this work as one of the constraints of extrusion of the HHSZ. Before ductile shearing, any straight foliation planes and straight grain boundaries non-parallel to the MCT_L would remain straight and become segments of a parabola after the E_1 and the E_2 extrusion phases, respectively in conformity to their velocity profiles. Since the ductile shear strain during at the end of the E_2-pulses should ideally be most intense near the boundaries of the flow zones, parabolic fabrics are expected to be strongly developed near the MCT_L and within the $STDS_U$ and the $STDS_L$. Contrary to this prediction, but as in the remainder of the HHSZ (e.g. Jain et al. 2002 and references therein) and also in other shear zones (cf. Passchier and Trouw 2005), shear fabrics and grain boundaries in the $STDS_U$ and the $STDS_L$ are usually sigmoid (Fig. 5a–d, 6b–d, 7a, 8a), rarely parallelogram shaped (Fig. 8b), but never parabolic. The behaviour of single or aggregates of mineral(s) as heterogeneous strain markers (Treagus et al. 1996) seems to be the key reason for the deviation from the simplest prediction. For example, even if simple shear with a characteristic linear velocity profile is imposed on a composite of matrix and square-shaped clasts, the clasts may acquire curved boundaries depending on the viscosity contrast between them and the matrix (Treagus and Lan 2004 and references therein). Though not investigated in this study, the shape of the clasts in clast-matrix aggregates under the proposed shifting combined extrusive flow may, therefore, be different from its velocity profile.

Negative results in tectonic modeling

Possibility-I: Can the $STDS_U$ and the $STDS_L$ form synchronously by a combined simple shear and channel flow through two viscous media in the HHSZ? (Fig. 20)

We consider the geometry, geographic orientation and the coordinate axes of the channel the same as in Fig. 16a. The channel is considered to be filled with two immiscible Newtonian viscous fluids of different viscosities. The fluid with lower viscosity is considered as the top layer. The consideration is justified since the present study has revealed a broad lithologic division of the Sutlej section of the HHSZ into more viscous rocks at the bottom and less viscous rocks within the top during the extensional ductile shearing events (Fig. 3, constraint I in "Constraints"). The location of the contact between the two fluids in Fig. 20 is equivalent to the locality Shongthong in Fig. 3. The top and the bottom boundaries of the channel are sheared in a top-to-SW sense and a uniform pressure gradient is allowed on both the fluids so that they flow southwestward leading to simple shear deformation (partly constraint VIII in "Constraints").

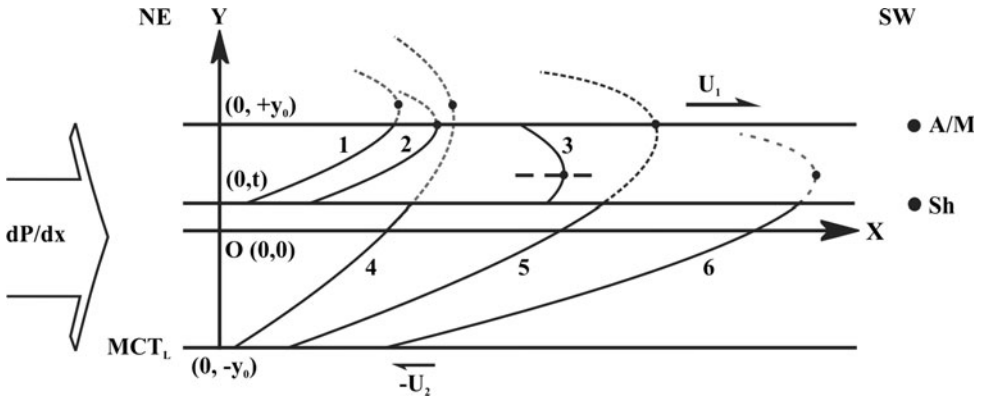

Fig. 20 The Higher Himalayan Shear Zone (HHSZ) is considered as a channel with geographic orientation, geometry, coordinate axes and the marker same as in Fig. 16a. The channel consists of two Newtonian viscous fluids with viscosities μ_1 and μ_2 ($\mu_1 < \mu_2$). Between the lines passing through the location Shongthong (Sh) and between Akpa and Morang (A/M), the fluid of lower viscosity (μ_1) resides. Between the line passing through 'Sh' and the MCT_L, the fluid of higher viscosity (μ_2) is confined. The two media are subjected to the same pressure gradient (dP/dx) along with shearing of the top- and the bottom walls with velocities U_1 and U_2, respectively, in a top-to-SW sense. Possible parabolic profiles *1–3* and *4–6* are inside the fluid layers with lower- and higher viscosities, respectively. For the sake of presentation in a single diagram, the possible profiles are drawn side by side. They do not represent movement of the marker from one profile to another. The Y-ordinate of the vertices of the profiles in two layers are the same (Eq. 35 in the "Appendix"). Therefore, in different situations one out of the three pairs of profiles *1*, *4*; *2*, *5*; and *3*, *6* should occur. The dashed part of the velocity profiles remain outside the respective flow domains but are drawn in order to show their vertices. For a northeasterly dipping channel, only profile-3 gives rise to an $STDS_U$. The lower boundary of the $STDS_U$ is marked with a *dash line*. The $STDS_L$ characterized by a top-to-NE sense of shearing is not produced in any of the cases in the lower fluid layer. MCT_L Main Central Thrust-Lower, $STDS_U$ South Tibetan Detachment System-Upper, $STDS_L$ South Tibetan Detachment System-Lower

The velocity profiles produced in the two fluid layers are segments of parabolas with each set having common *y*-ordinates (Eq. 35 in "Appendix"). Considering the isograds as inactive markers, the parabolic velocity profiles would give rise to inverted metamorphism in the HHSZ (constraint IX in "Constraints"). For particular sets of flow parameters, the vertex of the parabolic profile lies inside the fluid with lower viscosity, thereby simulating a zone of top-to-NE sense of ductile shearing i.e. the $STDS_U$ (curve 5 in Fig. 20). This $STDS_U$ is much thinner than the remainder of the HHSZ, which partly agrees with the constraint XI in "Constraints". However, the main drawback is that it can not produce a $STDS_L$ (partly constraint IV in "Constraints"). As a consequence, the constraints on the thickness and oft noted absence in certain sections of the Himalaya of the $STDS_L$ (constraints XII and XIV respectively, in "Constraints") also remain unexplained.

Possibility-II: Can ductile extensional shearing in the $STDS_U$ and the $STDS_L$ form contemporaneously in a single viscous medium? Simple shearing throughout the HHSZ and a preferential channel flow within the top are assumed (Fig. 21)

The HHSZ is considered to be a channel with geometry, geographic orientation and coordinate axes that are the same as the previous case. The channel is assumed to be filled with a single Newtonian viscous fluid medium. The top- and the bottom boundaries of the channel are subject to a top-to-SW

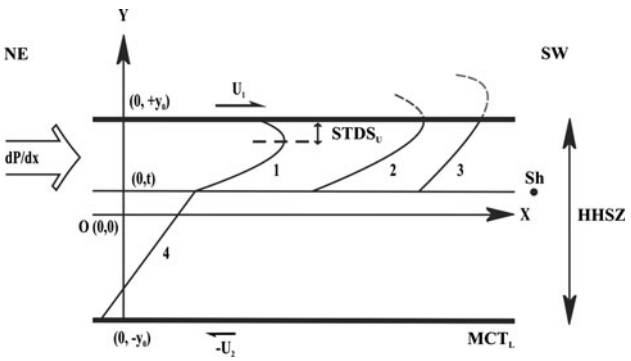

Fig. 21 The Higher Himalayan Shear Zone (HHSZ) is considered as a channel with geographic orientation, geometry, rheology, coordinate axes and the marker same as in Fig. 16a. The pressure gradient dP/dx is presumed to be confined within lines $y = t$ passing through Shongthong (Sh) and the upper boundary of the channel taken as the line $y = y_0$. The top- and the bottom walls of the channel undergo shearing with velocities U_1 and U_2, respectively, in a top-to-SW sense. Possible positions of vertices of the parabolic profiles in the top sub-channel are shown by the parabolic profiles *1*, *2* and *3*. For the sake of presentation in a single diagram, the possible profiles are drawn side by side. They do not represent movement of the marker from one profile to another. Only profile-1 simulates the $STDS_U$. Profiles *2* and *3* have their vertices located on the top wall and outside the channel, respectively. No $STDS_U$ is produced in these cases. In the lower flow domain, linear profile-4 is produced in all the cases characteristic of a top-to-SW sense of shearing. The $STDS_L$ is never produced. $STDS_U$ South Tibetan Detachment System-Upper; $STDS_L$ South Tibetan Detachment System-Lower; MCT_L Main Central Thrust-Lower

sense of simple shearing. In addition to this, the top fluid layer is under a pressure gradient. The justification of such idea is that only the top layer of the HHSZ acquired an intensive fluid character as indicated by protracted granitic melts and migmatization. The velocity profiles produced in the top zone is a parabola and that inside the lower zone is a straight line (Eqs. 36, 37 in "Appendix"). For certain combination of flow parameters, the vertex of the parabolic profile may lie within the channel, at the top wall or even outside the channel (curves 1, 2 and 3, respectively in Fig. 21). In the former case, an extensional ductile shear zone forms in the top layer equivalent to the $STDS_U$ (partly constraint IV in "Constraints"). Simulation of an $STDS_L$ inside the more viscous lower layer (constraints V and partly IV in "Constraints") is never possible. Thus, the constraints on the thickness and often absence of the $STDS_L$ in certain sections of the Himalaya (constraints XII and XIV in "Constraints") remain unexplained.

Possibility-III: Can extensional ductile shearing in the $STDS_U$ and the $STDS_L$ take place simultaneously by a Poiseuille flow in a gently and strongly diverging upward HHSZ? (Figs. 22, 23a–d)

This is addressed by presenting two out of 14 analogue models performed in the Hans Ramberg Tectonic Laboratory, Uppsala University. A channel flow box (Fig. 22) was prepared that consisted of an inclined channel equivalent to the HHSZ and an interconnected horizontal channel that is alike the feeder channel of extruded rocks of the HHSZ (also see Figure 3a of Godin et al. 2006). The dip of the boundaries of the model HHSZ are 30°, 40° and 60° (Vannay and Grasemann 2001; Figure 2 of Jamieson et al. 2004; Yin 2006) in different experiments and are diverging upward. Geometric similarity between the HHSZ in natural case and the present analogue models is maintained by choosing the thickness of the inclined channel, the orthogonal thicknesses of the horizontal channel and the depth at which the upper wall of the horizontal channel resides to be equivalent to 25–50 km (Figure 2 of Jamieson et al. 2004; and Stephenson 2000 for the optimum values), 15–50 km (from Jamieson et al. 2004; and Acharya and Ray 1977) and 35 km (average value from Figure 8b of Hauck et al. 1998), respectively. As the presented models are based on static channels, which are in contrast to the real situation of their southward migration and deformation as portrayed by Jamieson et al. (2004), they are kinematically dissimilar. However, as both the flows in analogue models and the field situations are of Reynolds Number $\ll 1$ (Eq. 40 onwards in the "Appendix"), they are dynamically similar. Polydimethylsiloxane (PDMS 36), a transparent incompressible Newtonian viscous polymer with a density 0.95 cc and a viscosity of 10^5 Pa s (Talbot and Aftabi 2004; and references therein) was used as the model material.

Although rocks of the Sutlej section of the HHSZ have been classified into two contrasting viscosities (constraint I in "Constraints"), we use a single model material due to the inherent difficulty of incorporating two deformable see-through materials in the channel flow box. Grids, partially

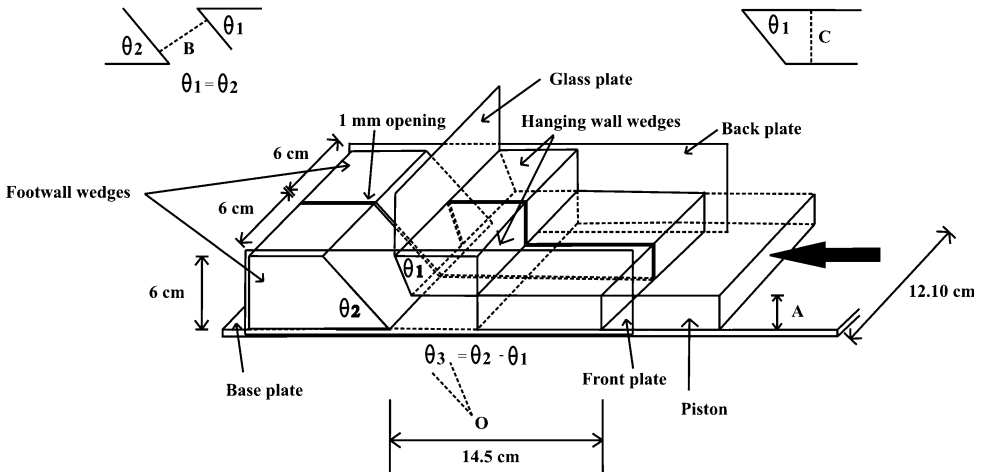

Fig. 22 The channel flow box consisting of an inclined channel analogous to the Higher Himalayan Shear Zone (HHSZ) and a linked horizontal channel. The hanging wall- and the footwall wedges constitute the inclined channel. A number of wedges were manufactured for various dip angles, θ_1 and θ_2. After setting them on a base plate, the wedges were attached with a plate in front and one in back. For a diverging upward inclined channel, i.e. $\theta_1 > \theta_2$, the aperture angle is $\theta_3 = \theta_1 - \theta_2$. Dimensions A, B and C are equivalent dimensions of thicknesses of the horizontal channel, that of the HHSZ and the depth at which the inclined channel meets the horizontal channel, respectively. The values of A, B, θ_1 and θ_2 for different experiments are listed in Table 1. In all the experiments, $C = 3.5$ cm. A pair of thin, parallel lines represents the 1 mm opening along which grids can be imprinted on the PDMS and the two halves can be screwed into a single box. A rectangular parallelepiped piston is pushed from right towards left side within the PDMS filled horizontal channel. A 'glass plate' is used in some experiments to restrict the direction of flow of the extruded PDMS. Not to scale

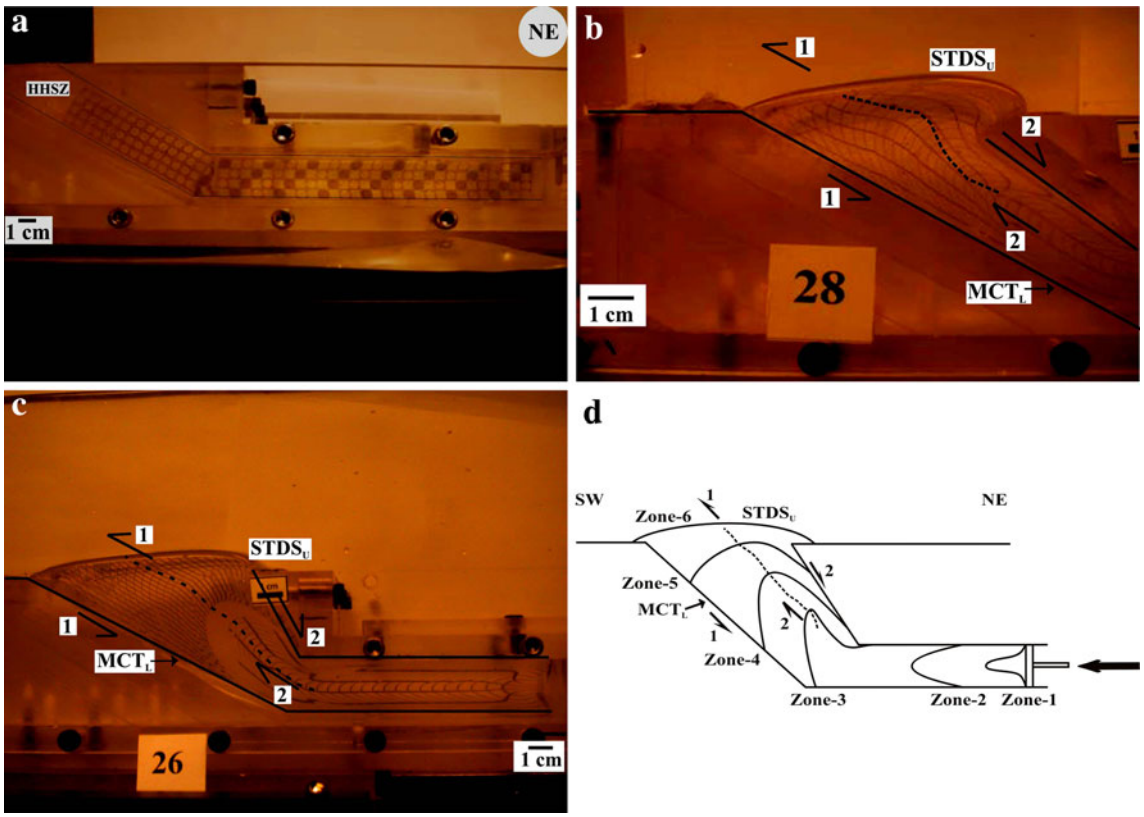

Fig. 23 **a** The channel flow box full of PDMS and imprinted undeformed grids before the onset of piston push. The dip of the parallel wall inclined channel is 30°. Each smallest square in the grid are of 5 mm × 5 mm in dimensions. *HHSZ* Higher Himalayan Shear Zone. **b–c** Upon pushing the piston through the horizontal channel, the extrusive flow in the northeasterly dipping diverging upward inclined channel gets divided into a zone of compressional top-to-SW sense of ductile shearing in southwest (*half arrows 1*) and a zone of extensional top-to-NE sense of ductile shearing characteristic of the South Tibetan Detachment System-Upper ($STDS_U$) in the northeast (*half arrows 2*). The *dashed curve* demarcates the boundary between the two zones. MCT_L Main Central Thrust-Lower. In **b**, the inclined channel is gently diverging upward—the MCT_L and the top of the $STDS_U$ dip at 30° and 40°, respectively. Photograph number-28. Time: 111 min. Experiment number: HRTL-1. In **c**, the inclined channel is strongly diverging upward—the MCT_L and the top of the $STDS_U$ dip at 30° and 60°, respectively. Photograph number-26. Time: 125 min. Experiment number: HRTL-2. Scales are indicated in these photographs. **d** Schematic representation of shear senses produced in all the experiments. Different flow zones are also shown. No second extensional ductile shear zone $STDS_L$ is formed in any cases

photocopied on transparent sheets, were imprinted on the PDMS. A piston was pushed with a constant velocity inside the horizontal channel filled with PDMS. The deformed geometries of grids near the exit of the inclined channel are only important for this study since they represent the ductile deformation within the HHSZ that is visible at the surface during field-studies. No piston push exists in the real tectonic scenario of the Himalaya–Tibet orogen, but the logic for doing so in models is to generate a channel flow characterized by parabolic profiles in the lower channel and let it extrude through the inclined diverging upward channel and to observe the senses of shearing near the exit. The horizontal channel is made as long as it is needed to generate parabolic profiles in the horizontal channel upon pushing the piston. Figure 23a shows the set up of the instrument before the piston was pushed.

As the PDMS slowly extrudes by laminar flow, marker lines initially parallel to the walls of the inclined channel act as primary shear planes (the C-planes). The deformation of the marker lines, which were perpendicular to the walls before the onset of piston push, represents the ductile sense of shearing. In the experiments with gently and strongly diverging upward channels (Table 1), the velocity profiles near the exit are parabolic or rounded. This gives rise to a single extensional ductile shear zone within the top of the model HHSZ (Fig. 23b–d), which is therefore equivalent to the $STDS_U$. Thus, the analogue models indicate that simultaneous generation of two extensional ductile shear zones within the HHSZ is not possible. A manuscript on the full description and interpretation of the analogue models, in line of the published abstracts (Mukherjee et al. 2008; 2009) is under preparation.

Table 1 Summary of specifications of analogue models

Exp No.	Channel flow box configuration					PDMS mass inside channel flow box (gm)	Exp continued till (min)	Gear	Piston velocity (mm per 10 min)
	θ_1	θ_2	θ_3 (= $\theta_1 - \theta_2$)	A (cm)	B (cm)				
HRTL-1	40	30	10 (GD)	2.50	1.5–2.5	728.4	202	0.3	3.0
HRTL-2	60	30	30 (SD)	2.50	1.5–5.0	771.3	250	0.6	5.9

The parameters θ_1, θ_2, θ_3, A and B are defined in Fig. 22

GD, *SD* gently and strongly diverging-up inclined channels

Conclusions

Besides a top-to-SW ductile shearing in the Sutlej section of the HHSZ, two spatially separated zones of late top-to-NE ductile shearing, the $STDS_U$ and the $STDS_L$, are demarcated in the field and validated in the thin-section studies. Field observation of duplexes with top-to-SW brittle shearing is corroborated in micro-scale by hat shaped minerals, commonly micas, whose longest boundaries dip northeasterly and acted as 'P' planes. Brittle–ductile extension parallel to main foliations gave rise to boudins of different morphologies throughout the HHSZ.

A 'shifting combined flow model' of extrusion $E = E_1 + E_{2a} + E_{2b}$ of the HHSZ in the ductile regime is presented based on minimum parameters of extrusion viz. (1) thickness of the flow zones, (2) viscosity of the extruding rocks, (3) the pressure gradient, and (4) relative rate of slip on the boundaries of the flow zones. The model considers (1) the boundaries of the HHSZ to be parallel, (2) the extruding rocks to be incompressible Newtonian viscous, (3) combinations of simple shear, pure shear and a pressure gradient induced flow, and (4) spatial shifts in extrusion in the shear zone. In the E_1-phase during 25–19 Ma, the upper sub-channel defined by the MCT_U and the top of the HHSZ underwent a top-to-SW simple shearing. This gave rise to a linear velocity profile and no extensional ductile shear zone was produced.

The subsequent E_{2a}-pulse of extrusion was characterized by a combined simple shear and pure shear of the boundaries of the entire HHSZ along with a pressure gradient induced flow during 15–14 Ma. This resulted in a ductile extensional shear zone within the top of the HHSZ, which is the $STDS_U$. The final E_{2b}-pulse was constituted by a top-to-SW shearing and a pressure gradient component both restricted in the lower sub-channel defined by the MCT_L and the top of the now $STDS_L$ during 14–12 Ma. This gave rise to an extensional ductile shear zone, the $STDS_L$, within the lower sub-channel. The velocity profiles for the two pulses of the E_2-phase are parabolas. The simulated $STDS_U$ and the $STDS_L$ are thinner than the HHSZ and their lower boundaries are defined by lines passing through the vertices of the respective profiles. The proposed extrusion model of the HHSZ may be valid in other sections subject to different timing of the extrusion phases and pulses.

Simultaneous generation of extensional ductile shearing in the $STDS_U$ and the $STDS_L$ is demonstrated to be implausible in the following models of extrusion of the HHSZ with parallel boundaries: (1) a two-layered viscous lithology and a channel flow along with a top-to-SW sense of shearing; and (2) a top-to-SW sense of shearing throughout the HHSZ and a restricted channel flow in the upper part of the shear zone. In addition, (3) a Poiseuille flow initiating from a horizontal channel and extruding through linked gently and strongly diverging upward HHSZ as performed in a number of analogue models with a 'channel flow box' using Newtonian viscous Polydimethylsiloxane and maintaining geometric and dynamic similarity with the natural case also gave negative results. In all these cases, a single extensional ductile shear zone similar to the $STDS_U$ was produced in the model HHSZ.

As per the proposed model, the thicknesses of the $STDS_U$ and the $STDS_L$ are functions of the four flow parameters that define their velocity profiles. Over a wide geographic and temporal extent, these parameters varied to the extent that gave rise to a disparity in thickness of the $STDS_U$ and absence of the $STDS_L$ in different Himalayan sections. During the whole extrusion process, the metamorphic isograds acted as inactive markers, underwent deformation in the same manner as the velocity profiles of different phases and, in the E_2-phase, gave rise to inverted metamorphism in the HHSZ.

The proposed extrusion model predicts the following: (1) Ductile shear strain in the upper sub-channel defined by the MCT_U and top of the now $STDS_U$ during and at the end of the E_1-phase was uniform. Since the HHSZ underwent other phases of extrusion, this conjecture is not possible to crosscheck. (2) After the E_{2a}-pulse, ductile shear strain was most intense at the boundaries of the HHSZ and progressively reduced towards the base of the $STDS_U$. (3) In the next E_{2b}-pulse, shear strain was more severe in the lower sub-channel delimited by the MCT_L and the top of the now $STDS_L$ than in the remainder of the HHSZ. Within this sub-channel, shear strain decreased from both the boundaries towards the lower boundary of the $STDS_L$. Previously reported values of a higher magnitude of simple shear at the

boundaries and its lesser value inside the HHSZ broadly support surmises (2) and (3). (4) The bases of the $STDS_U$ and the $STDS_L$ extruded at highest rates and the extrusion rates kept decreasing towards the boundaries of E_{2a}- and the E_{2b}- flow pulses, respectively. (5) For certain magnitudes of the flow parameters, the $STDS_U$ can be absent and the thickness of the $STDS_L$ varies along the Himalayan trend. Suitable data does not exist to confirm prediction (4) and the variable thickness of the $STDS_L$. (6) Had they behaved as inactive markers, the ductile shear fabrics after the E_{2b}-pulses inside the $STDS_U$, the $STDS_L$ and near the MCT_L are expected to become segments of parabolas. In contrast, the ductile shear fabrics reported from field and micro-scales are more often sigmoid-shaped and do not fit with this prediction. This could be due to heterogeneous deformation of real rocks on meso- and micro-scales.

As the extruding rocks of the HHSZ entered the brittle deformation regime around 12 Ma, the pressure gradient component ceased. However, the top-to-SW sense of shearing continued in the brittle regime along the pre-existing ductile shear planes and allowed rocks to arrive at a lower crustal level. This extensional phase leading to boudinage probably did not facilitate the extrusion.

Acknowledgments SM acknowledges the Guest Scholarship (2005–2006) of Swedish Institute, 2002–2007 Junior and Senior Research Fellowships (grant numbers: F.NO.2-48/2001(II)EU.II and 9/143(441)/2003-EMR-I, respectively) of the Council of Scientific and Industrial Research (India), 2008 Research Associateship of Jawaharlal Nehru Center for Advanced Scientific Research (JNCASR, India) and 2009 onwards 'Seed Grant' (Spons/GS/SM-1/2009) of Indian Institute of Technology Bombay. Swedish Research Council supported HAK. Discussions with K. C. Sahu (Imperial College) and C. J. Talbot (Uppsala University) on channel flow, and with A. K. Jain (Indian Institute of Technology Roorkee) on Himalayan geology were beneficial. C. J. Talbot owes additional thanks to help us in designing the 'channel flow box' (Fig. 22), fine tuning the English and sharpening research problems. R. Chakrabarti (Harvard University), S. Bhattacharyya (Alabama University) and A. Ghatak (Rochester University) constantly updated us on Himalayan Geology. Several interactions with R. Govindarajan (JNCASR) led SM to correlate channel flow with the Himalayan tectonics. The 'channel flow box' was manufactured by Sören Karlson (Uppsala University). A number of constructive reviews by B. C. Burchfiel (Massachusetts Institute of Technology) significantly improved the manuscript. W-C. Dullo, M. Dullo and the Indian Springer team are thanked for their efficient editorial handling of the manuscript.

Appendix 1: Simple shear flow (line 1 in Fig. 16a)

Steady plane laminar flow of an incompressible Newtonian fluid within a very long NE–SW oriented channel with parallel- and horizontal walls is given by

$$\mathrm{d}P/\mathrm{d}x = \mu\left(\mathrm{d}^2x/\mathrm{d}y^2\right) \quad (1)$$

(Schlichting and Gersten 1999) Here, $\mathrm{d}P/\mathrm{d}x$ pressure gradient along X-direction, μ viscosity. Putting $\mathrm{d}P/\mathrm{d}x = 0$, for simple shear,

$$\left(\mathrm{d}^2x/\mathrm{d}y^2\right) = 0 \quad (2)$$

Integrating twice, taking the channel thickness '$2y_o$' and velocity of walls $x = -U_2, U_1$ at $y = -y_0, y_0$, respectively, the flow profile is:

$$x = 0.5(U_1 - U_2) + 0.5yy_0^{-1}(U_1 + U_2) \quad (3)$$

Putting $x = 0$ in Eq. 3, the coordinate of the pivot, defined by intersection between the y-axis and the velocity profile, is $P_1 \equiv [0, y_0(U_1 - U_2)(U_1 + U_2)^{-1}]$

Appendix 2: Channel flow/Poiseuille flow (curve 2 in Fig. 16a)

A channel with geometry, orientation and rheology same as that of the previous case is considered. Here $U_1, U_2 = 0$ at $y = +y_0, -y_0$, $\mathrm{d}P/\mathrm{d}x$ is a constant $\neq 0$. Integrating Eq. 2 twice and using these boundary conditions, the profile as in many fluid mechanics text e.g. Pai (1956) is

$$x = -0.5\mu^{-1}(dP/dx)\left(y_0^2 - y^2\right) \quad (4)$$

The vertex of this parabolic profile is $[0.5\mu^{-1}y_0^2(\mathrm{d}P/\mathrm{d}x), 0]$

Appendix 3: Velocity profile of general shearing (Fig. 15b)

We first consider pure shear on a rectangle ABCD where a pair of opposite walls, AD and BC, move with unequal velocities U_3 and U_4, respectively ($U_3 > U_4$) (Fig. 15a). Let AD and AB are of lengths 'l' and '$2y_0$', respectively. Points A $(0, y_0)$ and B $(0, -y_0)$ on the two walls, after instant 't' come to A′$(0, y_0 - \mathrm{U}_3\ t)$ and B′$(0, U_4\ t - y_0)$. The line AB is deformed into a parabolic velocity profile P1 (Spurk 1993, pp 58–60), which is the velocity profile at A and B. The vertex of the parabolic profile is equidistant from these two points. Therefore, the Y-ordinate of vertex is $-0.5\ t\ (U_3 - U_4)$. Let the X-ordinate of the vertex is 'p'. Thus the vertex has the coordinate $[p, -0.5\ t\ (U_3 - U_4)]$. Let the equation of this parabola is

$$y^2 + Dx + Ey + F = 0 \quad (5)$$

Putting the co-ordinate of $A'$and B' in Eq. 5, E and F are solved, put back in Eq. 5, and is rewritten,

$$x = -D^{-1}\left[(U_3 - U_4)ty + (y_0 - U_3t)(U_4t - y_0) + y^2\right] \quad (6)$$

Area bounded by this parabola with the y-axis between coordinates $A'[0, (y_0 - \mathrm{U}_3\ t)]$ and $B'[0, (U_4\ t - y_0)]$ is

$$A_1 = -D^{-1} \int_{(U_4t-y_0)}^{(y_0-U_3t)} \left[y^2 + (U_3 - U_4)ty + (y_0 - U_3t).(U_4t - y_0)\right]\mathrm{d}y \quad (7)$$

or,

$$A_1 = -0.17D^{-1}(2y_0 - U_3t - U_4t) \times \left\{4(y_0 - U_3t)(U_4t - y_0) - t^2(U_3 - U_4)^2\right\} \quad (8)$$

Assuming a constant area deformation (Spurk 1993), it can be stated that the area bounded by the parabola P1 with the y-axis is half to that of area lost from the original rectangle due to compression, i.e.

$$A_1 = 0.5(U_3 + U_4)tL \quad (9)$$

Eliminating 'A_1' from Eqs. 8 and 9

$$D = -0.33t^{-1}L^{-1}(U_3 + U_4)^{-1}(2y_0 - U_3t - U_4t) \times \left[t(U_3 + U_4)\{4y_0 - (U_3 + U_4)t\} - 4y_0^2\right] \quad (10)$$

Putting this in Eq. 5 along with the values of E and F, the parabolic velocity profile for pure shear at point A is

$$x = (2y_0 - U_3t - U_4t)^{-1} \times \left[(U_3 + U_4)t\{4y_0 - (U_3 + U_4)t\} - 4y_0^2\right]^{-1} \times 3Lt(U_3 + U_4)\left[y^2 + (U_3 - U_4)ty + (y_0 - U_3t)(U_4t - y_0)\right] \quad (11)$$

Now a NE–SW oriented rectangle with very long length sides and full of incompressible Newtonian rheology and viscosity μ undergoing general shear by a pure shear and another component of top-to-SW sense of simple shearing (Fig. 15b) is represented by

$$x_{\text{general shear}} = x_{\text{pure shear}} + x_{\text{simple shear}} \quad (12)$$

Putting the expressions for $x_{\text{pure shear}}$ and $x_{\text{simple shear}}$ from Eqs. 3 and 11 in 12.

$$x_{\text{general shear}} = (2y_0 - U_3t - U_4t)^{-1} \times \left[(U_3 + U_4)t\{4y_0 - t(U_3 + U_4)\} - 4y_0^2\right]^{-1} \times 3Lt(U_3 + U_4)\left[y^2 + (U_3 - U_4)yt + (y_0 - U_3t)(U_4t - y_0)\right] + 0.5(\mathrm{U}_1 - \mathrm{U}_2) + 0.5\mathrm{y}y_0^{-1}(\mathrm{U}_1 + \mathrm{U}_2) \quad (13)$$

As this is a quadratic expression of y, it represents a parabola. The Y-ordinate of the vertex is

$$Y \equiv 0.5[(U_4 - U_3)t - (U_1 + U_2)\{(2y_0 - U_3t - U_4t) \times \{(U_3 + U_4)t(4y_0 - U_3t - U_4t) - 4y_0^2\} \times \{1.5Lt(U_3 + U_4)\}^{-1}\mathrm{y}_0^{-1}] \quad (14)$$

Therefore, the thickness of the $\mathrm{STDS_U}$ characterized by a top-to-NE sense of shearing within the top of the deformed rectangle is given by

$$T' = (y_0 - U_3t) - Y \quad (15)$$

The zone of top-to-NE shearing does not form when

$$T' \leq 0 \quad (16)$$

Appendix 4: A combination of simple shear and channel flow in a shifting mode (curve 3 in Fig. 17)

A channel with geometry, orientation and rheology same as that of "Appendix 1" is considered. The velocities are $x = U_{11}$, $-x = U_{21}$ at $y = y_0$, $-y_0$, respectively, at the boundaries; also a pressure gradient ($\mathrm{d}P_1/\mathrm{d}x$) acts. Using these in Eq. 2, the velocity profile, defined within $y = y_0$, $-y_0$, is

$$x = 0.5(U_{11} - U_{21}) + 0.5yy_0^{-1}(U_{11} + U_{21}) - 0.5\mu^{-1}(\mathrm{d}P_1/\mathrm{d}x)\left(y_0^2 - y^2\right) \quad (17)$$

From Eqs. 3, 4 and 17, we note that $x_{\text{combined flow}} = x_{\text{simple shear}} + x_{\text{channel flow}}$.

The parabolic profile given by Eq. 17 has its vertex at:

X-ordinate: $0.5\ (U_{11} - U_{21}) - 0.125\ \mathrm{y}_0^{-2}(U_{11} + U_{21})^2\ \mu\ (\mathrm{d}x/\mathrm{d}P_1) - 0.5\ \mu^{-1}\ y_0^2\ (\mathrm{d}P_1/\mathrm{d}x)$

Y-ordinate: $-0.5y_0^{-1}\ \mu\ (U_{11} + U_{21})(\mathrm{d}x/\mathrm{d}P_1)$

The maximum value of the X-ordinate on profile 17 is obtained at the vertex. Therefore, the fluid attains highest velocity $U_3 = X$-ordinate at the vertex. For another combined simple shear and channel flow in the sub-channel defined by the walls $y = -t$, $-y_0$ due to their shear velocities $x = U_{12}$, $-U_{22}$, respectively, and a pressure gradient ($\mathrm{d}P_2/\mathrm{d}x < 0$), the velocity profile is to be deduced. Transforming O′[0,−0.5 $(y_0 + t)$] as the new origin [0,0], the old coordinates [0,$-t$] and [0,0] become [0,0.5 $(y_0 -$ t)], and [0,0.5 $(y_0 + t)$], respectively. Substituting $y_0 = 0.5$ $(y_0 -$ t), $U_{11} = U_{12}$, $U_{21} = U_{22}$ and $(\mathrm{d}P_1/\mathrm{d}x) = (\mathrm{d}P_2/\mathrm{d}x)$ in Eq. 17, the velocity profile, defined within $y = 0.5$ $(y_0 -$ t), 0.5 $(y_0 + t)$, with reference to the new coordinate axes, is

$$x = 0.5(U_{12} - U_{22}) + 0.5(U_{12} + U_{22})(y_0 - t)^{-1}y - 0.5\mu^{-1}(\mathrm{d}P_2/\mathrm{d}x)\left[\{0.5(\mathrm{y}_0 - \mathrm{t})\}^2 - \mathrm{y}^2\right] \quad (18)$$

Now going back from new origin O'[0,0] to the old origin O [0,0.5 $(y_0 + t)$], Eq. 18 is rewritten

$$x = 0.5(U_{12} - U_{22}) + (U_{12} + U_{22})(y_0 - t)^{-1} \times [y - 0.5(y_0 + t)] - 0.5\mu^{-1}(\mathrm{d}P_2/\mathrm{d}x) \times \left[(y_0 + t) - \left\{0.5\left(y_0^2 + t^2\right)\right\} - y^2\right] \quad (19)$$

The profiles given by Eqs. 17 and 19 have zones of top-to-NE shearing, the $\mathrm{STDS_U}$ and the $\mathrm{STDS_L}$, respectively, with thicknesses

$$T_1 = y_0 - 0.5y_0^{-1}(U_{11} + U_{21})\mu_1(\mathrm{d}P_1/\mathrm{d}x)^{-1} \quad (20)$$

$$T_2 = 0.5(y_0 - t) - (y_0 - t)^{-1}(U_{12} + U_{22})\mu_2(\mathrm{d}P_2/\mathrm{d}x)^{-1} \quad (21)$$

The thickness of the HHSZ outside the respective detachments are

$$T_1' = \left[y_0 + 0.5y_0^{-1}(U_{11} + U_{21})\mu_1(\mathrm{d}P_1/\mathrm{d}x)^{-1}\right] \quad (22)$$

$$\mathrm{T}_2' = \left[(\mathrm{y}_0 - \mathrm{t}) + 0.5(\mathrm{y}_0 - \mathrm{t})^{-1}(\mathrm{U}_{12} + \mathrm{U}_{22})\mu_2(\mathrm{dP}_2/\mathrm{dx})^{-1}\right] \quad (23)$$

From Eqs. 20–23, we note $T_1 < T_1'$and $T_2 < T_2'$. From Eq. 19, the $\mathrm{STDS_U}$ does not form when

$$(U_{11}+U_{21})(\mathrm{d}P_1/\mathrm{d}x)^{-1} = \mathrm{or} > \left(2y_0^2\mu_1^{-1}\right);\ T_1 = \mathrm{or} < 0 \quad (24)$$

From Eq. 21, the $\mathrm{STDS_L}$ does not form when

$$(U_{12} + U_{22})(\mathrm{d}P_2/\mathrm{d}x)^{-1} = \mathrm{or} > \left[2(y_0 - \mathrm{t})^2\mu_2^{-1}\right];\ T_2 = \mathrm{or} < 0 \quad (25)$$

Note that for certain combination of flow parameters (y_0, U_{11}, U_{21}, μ_1, $\mathrm{d}P_1/\mathrm{d}x$, t, U_{12}, U_{22}, μ_2 and $\mathrm{d}P_2/\mathrm{d}x$), T_2 is $<T_1$.

Appendix 5: Combined flow through a two-layer HHSZ (Fig. 20)

A channel of same geometry and geographic orientation as "Appendix 1" is considered. The channel is assumed to be full with two immiscible Newtonian fluids- the top and the bottom layers with viscosities μ_1 and μ_2, respectively ($\mu_1 < \mu_2$). The line $y = t$ ($0 < t < -y_0$) is taken as the fluid interface. The top- and the bottom walls are sheared with velocities U_1 and $-U_2$, respectively, and $(\mathrm{dP/dx}) < 0$. The distribution of velocities in the top- and the bottom layers of the fluid are $\mathrm{x_1}$ and $\mathrm{x_2}$, respectively. The following deductions are based on steps similar to those in Papanastasiou et al. (2000). From Navier–Stokes equation, for the top and the bottom fluid layers

$$(\mathrm{d}P/\mathrm{d}x) = \mu_1\left(\mathrm{d}^2x_1/\mathrm{d}y_2\right) \quad (26)$$

$$(\mathrm{d}P/\mathrm{d}x) = \mu_2\left(\mathrm{d}^2x_2/\mathrm{d}y_2\right) \quad (27)$$

At the fluid interface, i.e. at the line $y = t$, the momentum flux is continuous through fluid–fluid interface. In other words, at $y = t$,

$$\mu_1(\mathrm{d}x_1/\mathrm{d}y) = \mu_2(\mathrm{d}x_2/\mathrm{d}y) \quad (28)$$

Integrating Eqs. 26 and 27:

$$(\mathrm{d}x_1/\mathrm{d}y)\mu_1 = y(\mathrm{d}P/\mathrm{d}x) + C \quad (29)$$

$$(\mathrm{d}x_2/\mathrm{d}y)\mu_2 = y(\mathrm{d}P/\mathrm{d}x) + C' \quad (30)$$

From Eqs. 28, 29, and 30, $C = C'$. Integrating Eqs. 29 and 30

$$x_1 = 0.5y^2\mu_1^{-1}(\mathrm{d}P/\mathrm{d}x) + Cy\mu_1^{-1} + C_1 \quad (31)$$

$$x_2 = 0.5y^2\mu_2^{-1}(\mathrm{d}P/\mathrm{d}x) + Cy\mu_2^{-1} + C_2 \quad (32)$$

Now at $y = t$, $x_1 = x_2$; at $y = +y_0$, $x_1 = U_1$; and at $y = -y_0$, $x_2 = -U_2$. Using these in Eqs. 31 and 32, $C_1 = C_2$. Using this back in Eqs. 31 and 32, C and C_1 are solved and put in those equations:

$$\begin{aligned} x_1 =& 0.5\mu_1^{-1}y^2(\mathrm{d}P/\mathrm{d}x) + y\mu_1^{-1} \\ &\times\left[(U_1+U_2)y_0^{-1}\left(\mu_1^{-1}+\mu_2^{-1}\right)^{-1} - 0.5y_0(\mathrm{d}P/\mathrm{d}x)\right. \\ &\left.\times\left(\mu_1^{-1}-\mu_2^{-1}\right)\left(\mu_1^{-1}+\mu_2^{-1}\right)^{-1}\right] \\ &+\left[\left\{(U_1\mu_1 - U_2\mu_2) - \mathrm{y}_0^2(\mathrm{d}P/\mathrm{d}x)\right\}(\mu_1+\mu_2)^{-1}\right] \end{aligned} \quad (33)$$

$$\begin{aligned} x_2 =& 0.5y^2\mu_2^{-1}(\mathrm{d}P/\mathrm{d}x) + y\mu_2^{-1}\left[(U_1+U_2)y_0^{-1}\left(\mu_1^{-1}+\mu_2^{-1}\right)^{-1}\right. \\ &\left.-0.5y_0(\mathrm{d}P/\mathrm{d}x)\left(\mu_1^{-1}-\mu_2^{-1}\right)\left(\mu_1^{-1}+\mu_2^{-1}\right)^{-1}\right] \\ &+\left[\left\{(U_1\mu_1 - U_2\mu_2) - y_0^2(\mathrm{d}P/\mathrm{d}x)\right\}(\mu_1+\mu_2)^{-1}\right] \end{aligned} \quad (34)$$

As these are quadratic equations of 'y', they represent parabolas with the same 'Y'-ordinate of their vertices

$$\begin{aligned} Y \equiv& -(U_1+U_2)y_0^{-1}\left(\mu_1^{-1}+\mu_2^{-1}\right)^{-1}(\mathrm{d}P/\mathrm{d}x)^{-1} \\ &+0.5y_0\left(\mu_1^{-1}-\mu_2^{-1}\right)\left(\mu_1^{-1}+\mu_2^{-1}\right)^{-1} \end{aligned} \quad (35)$$

Appendix 6: Flow restricted within the upper parts of the HHSZ (Fig. 21)

We choose a channel with a geometry, geographic orientation and rheology same as that of case- (I). A simple shear of top-to-SW sense with velocities of its top and bottom walls as U_1 and $-U_2$, respectively, and that only top portion of the channel ($y = t$ to y_0) have an additional flow component imparted by the pressure gradient ($\mathrm{d}P/\mathrm{d}x$). Replacing 't' in 'y' in Eq. 3, velocity along the X-direction at coordinate $(0,t)$ is

$$x = 0.5(U_1 - U_2) + 0.5y_0^{-1}\mathrm{t}(U_1 + U_2) \quad (36)$$

Thus, in the upper sub-channel, velocities of its boundaries are: $x = +U_1$, at $y = y_0$ and at $y = t$, $x = 0.5(U_1 - U_2) + 0.5\ y_0^{-1}\ t\ (U_1 + U_2)$.

Using these conditions and parameters in Eq. 2, the velocity profile in the upper sub-channel is

$$\begin{aligned} x =& 0.5\mu^{-1}y^2(\mathrm{d}P/\mathrm{d}x) + \left\{0.5yy_0^{-1}(U_1+U_2)\right\} \\ &- 0.5y\mu^{-1}(\mathrm{d}P/\mathrm{d}x)(y_0+t) \\ &+ 0.5(U_1 - U_2) + 0.5t\mu^1y_0(\mathrm{dP/dx}) \end{aligned} \quad (37)$$

The Y-ordinate of the vertex of the parabolic profile is

$$Y \equiv 0.5\left[(y_0 + t) - \mu(dP/dx)^{-1} y_0^{-1}(U_1 + U_2)\right]. \quad (38)$$

Three profiles 3, 2, and 1 are presented in Fig. 21 for $Y>$, =, and $<y_0$, respectively. Only in the former case, an $STDS_U$ forms with a thickness

$$T = (y_0 - Y) \quad (39)$$

Appendix 7: Calculations for analogue models

The Reynolds Number is defined as

$$R_e = \rho v y_0 \mu^{-1} \quad (40)$$

where ρ density of the fluid, μ dynamic viscosity of the fluid, y_0 half the width of the channel, and v velocity of flow. In the real situation of the HHSZ, taking crustal density $\rho = 2.7$ gm cm^{-3}, viscosity of partially molten mid-crustal rocks $\mu = 10^{19}$ Pa s (as taken by Jamieson et al. 2004), $v = 4.8$ mm year^{-1} (the maximum value for the Zanskar Shear Zone, a continuation of the $STDS_U$, as given by Dèzes et al. 1999), R_e comes out in the order of 10^{-21}.

In the model, taking the density of the PDMS $\rho = 0.95$ gm cm^{-3}, $\mu = 10^5$ Pa s (Talbot and Aftabi 2004 and references therein), the slowest velocity of extrusion attained $v = 3$ mm per 10 min, half the width of the model HHSZ (y_0) = 1.25 cm in few experiments, R_e comes out in the order of 10^{-14}.

References

Acharya SK, Ray KK (1977) Geology of the Darjeeling–Sikkim Himalaya. In: Guide to Excursion No. 4 Fourth International Gondwana Symposium, India, report, Calcutta, India, 25 pp

Annen C, Scaillet B, Sparks RSJ (2005) Thermal constraints on the emplacement rate of a large intrusive complex: the Manaslu Leucogranite, Nepal Himalaya. J Petrol 47:71–95. doi:10.1093/petrology/egi068

Argles TW, Edwards MA (2002) First evidence of high-grade, Himalayan age synconvergent extension recognized within the western syntaxis—Nanga Parbat, Pakistan. J Struct Geol 24:1327–2344. doi:10.1016/S0191-8141(01)00136-5

Arslan A, Passchier CW, Kohen D (2008) Foliation boudinage. J Struct Geol 30:291–309. doi:10.1016/j.jsg.2007.11.004

Beaumont C, Jamieson RA, Nguyen MH et al (2001) Himalayan tectonics explained by extrusion of a low-viscosity crustal channel coupled to focused surface denudation. Nature 414:738–742. doi:10.1038/414738a

Beaumont C, Jamieson RA, Nguyen MH et al (2004) Crustal channel flows: 1. Numerical models with application to the tectonics of the Himalayan-Tibetan Orogen. J Geophys Res 109:B06406. doi:10.1029/2003JB002809

Beaumont C, Jamieson R, Nguyen M (2006) The Himalayan-Tibet system: models of long term lithosphere-mantle interactions and the short term tectonic response to variable denudation. In: Ahmad T et al (eds) 21st Himalaya-Karakoram-Tibet Workshop. 29–31 March 2006. University of Cambridge, UK. Abstract Volume. J Asian Earth Sci 26:126

Bèrthe D, Choukroune P, Jegouzo P (1979) Orthogneiss, mylonite and non-coaxial deformation of granite: the example of the south Armorican shear zone. J Struct Geol 1:31–42. doi:10.1016/0191-8141(79)90019-1

Bhattacharya AR (1981) Stratigraphy and correlation of the Inner Kumaun Lesser Himalaya: implications of a mathematical study. In: Sinha AK (ed) Contemporary Geoscientific Research in Himalaya 1, pp 137–150

Bhattacharya AR (1999) Deformational regimes across the Kumaun Himalaya: a study in strain patterns. In: Jain AK, Manickavasagam RM (eds) Geodynamics of the NW Himalaya. Gond Res Gp Mem No 6 Field Science, Osaka, pp 81–90

Burbank DW (2005) Earth science: cracking the Himalaya. Nature 434:963–964. doi:10.1038/434963a

Burchfiel BC, Chen Z, Hodges KV et al (1992) The South Tibetan Detachment System, Himalayan orogen: extension contemporaneous with and parallel to shortening in a collisional mountain belt. Geol Soc Am Spec Pap 269:1–41

Caldwell WB, Klemperer SL, Rai SS et al (2009) Partial melt in the upper-middle crust of the northwest Himalaya revealed by Rayleigh wave dispersion. Tectonophysics. doi:10.1016/j.tecto.2009.01.013

Carosi R, Musumeci G, Pertusali PC (1999) Extensional tectonics in the higher Himalayan Crystallines of Khumbu Himal, eastern Nepal. In: Macfarlane A, Sorkhabi RB, Quade J (eds) Himalaya and Tibet: mountain roots to mountain tops, 328. Geological Society of London, Special Publication, Boluder, Colorado, pp 211–223

Carosi R, Montomili C, Visonà D (2007) A structural transect in the lower Dolpo: insights in the tectonic evolution of Western Nepal. J Asian Earth Sci 29:407–423. doi:10.1016/j.jseaes.2006.05.001

Catlos EJ (2000) Geochronologic and Thermobarometric Constraints on the Evolution of the Main Central Thrust, Himalayan Orogen. Unpublished PhD Dissertation. University of California. Los Angeles, pp xix–xx

Catlos EJ, Harrison TM, Kohn MJ et al (2001) Geochronological and thermobarometric constraints on the evolution of the main central thrust, central Nepal. J Geophys Res-Solid Earth 106:16117–16204. ISSN:0148-0227

Chambers JA, Argles TW, Horstwood MSA et al (2008) Tectonic implications of Paleoproterozoic anatexis and Late Miocene metamorphism in the Lesser Himalayan Sequence, Sutlej Valley, NW India. J Geol Soc Lond 165:725–737. doi:10.1144/0016-76492007/090

Cottle JM, Jessup MJ, Newell DL et al (2006) Structure of the South Tibetan detachment system, Kharta region south Tibetan Himalaya. In: Ahmad T et al (eds) 21st Himalaya-Karakoram-Tibet Workshop. 29–31 March 2006. University of Cambridge, UK. Abstract Volume. J Asian Earth Sci 26:132

Cottle JM, Jessup MJ, Newell DL et al (2007) Structural insights into the early stages of exhumation along an orogen-scale detachment: the South Tibetan Detachment System, Dzakaa Chu section, Eastern Himalaya. J Struct Geol 29:1781–1797. doi:10.1016/j.jsg.2007.08.007

Dasgupta S, Chakraborty S, Neogi S (2009) Petrology of an inverted barrovian sequence of metapelites in Sikkim Himalaya, India: constraints on the tectonics of inversion. Am J Sci 309:43–84. doi:10.2475/01.2009.02

Davis GH, Reynolds SJ (1996) Structural Geology of Rocks and Regions, 2nd edn. Wiley, New York

Depietro JA, Pogue KR (2004) Tectonostratigraphic subdivision of the Himalaya—a view from the west. Tectonics 23:TC 5001. doi:10.1029/2003TC001554

Dewey L (2008) Continental lower-crustal flow: channel flow and laminar flow. Earth Sci Frontiers 15:130–139. doi:10.1016/S1872-5791(08)60065-2

Dèzes PJ (1999) Tectonic and Metamorphic evolution of the central Himalayan domain in southeast Zanskar (Kashmir India). PhD Thesis, University of Lausanne, Switzerland, pp 1–160

Dèzes PJ, Vannay JC, Steck A et al (1999) Synorogenic extension: quantitative constraints on the age and displacement of the Zanskar shear Zone. Geol Soc Am Bull 111:364–374. doi:10.1130/0016-7606(1999)111<0364:SEQCOT>2.3.CO;2

Druguet E, Carreras J (2006) Analogue modeling of syntectonic leucosomes in mylonitic schists. J Struct Geol 28:1734–1747. doi:10.1016/j.jsg.2006.06.015

Edwards MA, Kidd WSF, Li J et al (1996) Multi-stage development of the southern Tibet detachment system near Khula Kangri: new data from Gonto La. Tectonophysics 260:1–19. doi:10.1016/0040-1951(96)00073-X

Fraser G, Worley B, Sandiford M (2000) High-precision geothermometry across the High Himalayan metamorphic sequence, Langtang Valley, Nepal. J Meta Geol 18:665–681. doi:10.1046/j.1525-1314.2000.00283.x

Gansser A (1983) Geology of the Bhutan Himalaya. Birkhäuser Verlag, Switzerland

Ghosh SK (1993) Structural geology fundamental and modern development, Pergamon, Oxford

Godin L, Grujic D, Law RD et al (2006) Channel flow, extrusion and exhumation in continental collision zones: an introduction. In: Law RD, Searle MP (eds) Channel flow, extrusion and exhumation in continental collision zones, volL 268. Geological Society of London, Special Publication, pp 1–23. doi:10.1144/GSL.SP.2006.268.01.01

Goscombe B, Gray D, Hand M (2006) Crustal architecture of the Himalayan metamorphic front in eastern Himalaya. Gond Res 10:232–255. doi:10.1016/j.gr.2006.05.003

Grasemann B, Vanney J-C (1999) Flow controlled inverted metamorphism in shear zones. J Struct Geol 21:743–750. doi:10.1016/S0191-8141(99)00071-1

Grasemann B, Fritz H, Vannay JC (1999) Quantitative kinematic flow analysis from the Main Central Thrust Zone (NW-Himalaya, India): implications for a decelerating strain path and extrusion of orogenic wedges. J Struct Geol 21:837–853. doi:10.1016/S0191-8141(99)00077-2

Grasemann B, Edwards MA, Wiesmayr G (2006) Kinematic dilatancy effects on orogenic extrusion. In: Law RD, Searle MP, Godin L (eds) Channel flow, ductile extrusion and exhumation in continental collisional zones, vol 268. Geological Society of London, Special Publication, pp 183–199. doi:10.1144/GSL.SP.2006.268.01.08

Grujic D (2006) Channel flow and continental collision tectonics: an overview. In: Law RD, Searle MP (eds) Channel flow, extrusion and exhumation in continental collision zones, vol 268. Geological Society of London, Special Publication, pp 25–37. doi:10.1144/GSL.SP.2006.268.01.02

Grujic D, Casey M, Davidson C (1996) Ductile extrusion of the Higher Himalayan crystalline in Bhutan: evidence from quartz microfabrics. Tectonophysics 260:21–43. doi:10.1016/0040-1951(96)00074-1

Grujic D, Hollister LS, Parrish RR (2002) Himalayan metamorphic sequence as an orogenic channel: insight from Bhutan. Earth Planet Sci Lett 198:177–191. doi:10.1016/S0012-821X(02)00482-X

Harris N (2007) Channel flow and the Himalayan–Tibetan orogen: a critical review. J Geol Soc Lond 164:511–523. doi:10.1144/0016-76492006-133

Hauck ML, Nelson KD, Brown LD et al (1998) Crustal structure of the Himalayan orogen at 900 east longitude from project INDEPTH deep seismic reflection profiles. Tectonics 17:481–500. doi:10.1029/98TC01314

Herren E (1987) Zanskar Shear Zone: northeast southwest extension within the Higher Himalaya (Ladakh, India). Geology 15:409–413. doi:10.1130/0091-7613(1987)15<409:ZSZNEW>2.0.CO;2

Hodges KV (2000) Tectonics of the Himalaya and southern Tibet from two decades perspectives. Geol Soc Am Spec Bull 112:324–350. doi:10.1130/0016-7606(2000)112<0324:TOTHAS>2.3.CO;2

Hodges KV (2006) A synthesis of the channel flow-extrusion hypothesis as developed for the Himalayan-Tibetan orogenic system. In: Law RD, Searle MP (eds) Channel flow, extrusion and exhumation in continental collision zones, vol 268. Geological Society of London, Special Publication, pp 71–90. doi:10.1144/GSL.SP.2006.268.01.04

Hodges KV, Le Fort P, Pêcher A (1988) Possible thermal buffering by crustal anatexis in collisional orogens: Thermobarometric evidence from the Nepalese Himalaya. Geology 16:707–710. doi:10.1130/0091-7613(1988)016<0707:PTBBCA>2.3.CO;2

Hodges KV, Bowring SA, Davidek KL et al (1998) Evidence for rapid displacement on Himalayan normal faults and the importance of tectonic denudation in the evolution of mountain ranges. Geology 26:483–486. doi:10.1130/0091-7613(1998)026<0483:EFRDOH>2.3.CO;2

Hollister LS, Grujic D (2006) Himalaya Tiber Plateau. Pulsed channel flow in Bhutan. In: Law RD, Searle MP, Godin L (eds) Channel flow, ductile extrusion and exhumation in continental collision zones, vol 268. Geological Society of London, Special Publication, pp 415–423. doi:10.1144/GSL.SP.2006.268.01.19

Hubbard MS (1996) Ductile shear as a cause of inverted metamorphism: example from the Nepal Himalaya. J Geol 104:493–499

Israil M, Tyagi DK, Gupta PK et al (2008) Magnetotelluric investigations for imaging electrical structure of Garhwal Himalayan corridor, Uttarakhand, India. J Earth Syst Sci 117:189–200. doi:10.1007/s12040-008-0023-0

Jain AK, Anand A (1988) Deformational and strain patterns of an intracontinental ductile shear zone- an example from the Higher Garhwal Himalaya. J Struct Geol 10:717–734. doi:10.1016/0191-8141(88)90079-X

Jain AK, Manickavasagam RM (1993) Inverted metamorphism in the intracontinental ductile shear zone during Himalayan collision tectonics. Geology 21:407–410. doi:10.1130/0091-7613(1993)021<0407:IMITID>2.3.CO;2

Jain AK, Manickavasagam RM (1997) Ductile shear as a cause of inverted metamorphism: example from the Nepal Himalaya: a discussion. J Geol 105:511–514. doi:10.1086/515943

Jain AK, Mukherjee S (2009) Cover photo: a flanking microstructure. Him Geol 30

Jain AK, Patel RC (1999) Structure of the Higher Himalayan Crystallines along the Suru-Doda Valleys (Zanskar), NW-Himalaya. In: Jain AK, Manickavasagam RM (eds) Geodynamics of the NW Himalaya. Gond Res Gp Mem No 6. Field Science, Osaka, pp 91–110

Jain AK, Manickavasagam RM, Singh S (1999) Collision tectonics in the NW Himalaya: deformation, metamorphism and emplacement of leucogranite along Beas-Parbati Valleys, Himachal Pradesh. In: Jain AK, Manickavasagam RM (eds) Geodynamics of the NW Himalaya, Gond Res Gp Mem No 6. Field Science, Osaka, pp 3–37

Jain AK, Kumar D, Singh S et al (2000) Timing, quantification and tectonic modelling of Pliocene-Quaternary movements in the NW Himalaya: evidences from fission track dating. Earth Planet Sci Lett 179:437–451. doi:10.1016/S0012-821X(00)00133-3

Jain AK, Singh S, Manickavasagam RM (2002) Himalayan collisional tectonics. Gond Res Gp Mem No. 7.Field Science, Hashimoto, p 4

Jain AK, Manickavasagam RM, Singh S et al (2005a) Himalayan collision zone: new perspectives—its tectonic evolution in a combined ductile shear zone and channel flow model. Himal Geol 26(1):1–18

Jain AK, Mukherjee S, Singh S (2005b) Great Himalayan orogenic channel: its structure and tectonic patterns. Abstract number: 58-SE-A1226. Solid earth. Asia Oceania Geosciences Society. 2nd Annual General Meeting 20–24 June 2005, Singapore. http://www.asiaoceania.org/abstract/se/58-SE-A1226.pdf

Jamieson RA, Beaumont C, Nguyen MH et al (2002) Interaction of metamorphism, deformation and exhumation in large convergent orogens. J Meta Geol 20:9–24. doi:10.1046/j.0263-4929.2001.00357.x

Jamieson RA, Beaumont C, Medvedev S et al (2004) Crustal Channel Flows: 2. Numerical models with implications for metamorphism in the Himalayan–Tibetan Orogen. J Geophys Res 109:B06407. doi:10.1029/2003JB002811

Janda C, Hager C, Grasemann B et al (2002) The Karcham Normal Fault—implications for an active extruding wedge, Sutlej valley, NW Himalaya. J Asian Earth Sci 20:19–20

Jessell MW (1987) Grain boundary migration microstructures in naturally deformed quartzite. J Struct Geol 9:1007–1014. doi:10.1016/0191-8141(87)90008-3

Jessup MJ, Law RD, Searle MP et al (2006) Structural evolution and vorticity of flow during extrusion and exhumation of the Greater Himalayan Slab, Mount Everest Massif, Tibet/Nepal: implications for orogen-scale flow partitioning, vol 268. Geological Society of London, Special Publication, pp 379–413. doi:10.1144/GSL.SP.2006.268.01.18

Kellet DAM (2006) Characterization and age of north-verging back structures in the Tethyan Sedimentary Sequence, Hidden Valley, central Nepal Himalaya. Unpublished M.Sc. thesis. Queen's University, Canada, p 27

Kellett DA, Godin L (2009) Pre-Miocene deformation of the Himalayan superstructure, Hidden valley, cenral Nepal. J Geol Soc London 166:1–14. doi:10.1144/0016-76492008-097

Kohn MJ (2008) P–T–t data from central Nepal support critical taper and reduplicate large-scale channel flow of the Greater Himalayan Sequence. Geol Soc Am Bull 120:259–273. doi:10.1130/B26252.1

Koyi HA, Milnes G, Schmeling H et al (1999) Numerical models of ductile rebound of crustal roots beneath mountain belts. Geophys J Int 139:556–562. doi:10.1046/j.1365-246x.1999.00978.x

Kumar D, Jain AK, Lal N (2005) Tectonic exhumation and paleoseismic events from the Higher Himalayan Crystallines (HHC), NW Himalaya: evidences from fission track (FT) dating. Abstract Number: 58-SEA0725. Asia Oceania Geosciences Society. Session: Solid Earth. 2nd Annual General Meeting 20–24 June 2005, Singapore. http://www.asiaoceania.org/abstract/se/58-SEA0725.pdf

Kwatra SK, Singh S, Singh VP et al (1999) Geochemical and geochronological characteristics of the early Paleozoic granitoids from Sutlej-Baspa Valleys, Himachal Himalaya. In: Jain AK, Manickavasagam RM (eds) Geodynamics of the NW Himalaya. Gondwana Res Gp Mem 6, pp 144–158

Larson KP, Godin L (2009) Kinematics of the Greater Himalaya sequence, Dhaulagiri Himal: implications for the structural framework of central Nepal. J Geol Soc Lond 166:25–43. doi:10.1144/0016-76492007-180

Law R, Searle MP, Simpson RL (2004) Strain, deformation temperatures and vorticity of flow at the top of the Greater Himalayan Slab, Everest Massif, Tibet. J Geol Soc Lond 161:305–320. doi:10.1144/0016-764903-047

LeCureux F, Burnett J (1975) Graphical methods used in the numerical solution of Jeffery–Hamel flow at fixed flow rates. Comput Graph ACM 1:233–238. doi:10.1016/0097-8493(75)90013-8

Lister LS, Snoke AW (1984) S-C mylonites. J Struct Geol 6:617–638. doi:10.1016/0191-8141(84)90001-4

Lombardo B, Pertusati P, Borghi S (1993) Geology and tectonomagmatic evolution of the eastern Himalaya along the Chomolungma-Makalu transect, vol 74. Geological Society of London, Special Publication, pp 341–355. doi:10.1144/GSL.SP.1993.074.01.23

Manickavasagam RM, Jain AK, Singh S et al (1999) Metamorphic evolution of the NW-Himalaya, India: pressure temperature data, inverted metamorphism, and exhumation in the Kashmir, Himachal and Garhwal Himalaya. In: Macfarlane A, Sorkhabi RB, Quade J (eds) Himalaya and Tibet: mountain roots to mountain tops. Geol Soc Am Spec Pap 328:179–198

Marchildon N, Brown M (2003) Spatial distribution of melt-bearing structures in anatectic rocks from Southern Brittany, France: implications for melt transfer at grain- to orogen-scale. Tectonophysics 364:215–235. doi:10.1016/S0040-1951(03)00061-1

Martin A, DeCelles P, Gehrels GE et al (2005) Isotopic and structural constraints on the location of the Main Central thrust in the Annapurna Range, central Nepal Himalaya. Geol Soc Am Bull 117:926–944. doi:10.1130/B25646.1

McClay KR, Insley MW (1986) Duplex structures in the lewis thrust sheet, crowsnest pass, rocky mountains, Alberta, Canada. J Struct Geol 8:911–922. doi:10.1016/0191-8141(86)90036-2

Molli G, Iacopini D, Pertusati PC et al (internet reference) Architecture, strain features and fault rock types of the South Tibetan Detachment system between Katra and Tingri (South Tibet Himalaya). http://209.85.175.104/search?q=cache:DWXY1Ve5_T8J:www.see.leeds.ac.uk/peachandhorne/friday/047_Mollietal.pdf+Architecture,+strain+features+and+fault+rock+types+of+the+South+Tibetan+Detachment+system+betwe&hl=en&ct=clnk&cd=1&gl=in; http://www.env.leeds.ac.uk/peachandhorne/friday/047_Mollietal.pdf (Accessed on 1 May 2008)

Mukherjee S (2005) Channel flow, ductile extrusion and exhumation of lower-middle crust in continental collision zones. Current Sci 89:435–436. http://www.iisc.ernet.in/currsci/aug102005/435.pdf

Mukherjee S (2007) Geodynamics, deformation and mathematical analysis of metamorphic belts of the NW Himalaya. Unpublished PhD thesis. Indian Institute of Technology Roorkee, pp 1–267

Mukherjee S (2008) Manifestation of brittle thrusting in micro-scale in terms of micro-duplexes of minerals in the Higher Himalayan Shear Zone, Sutlej & Zanskar section, northwest Indian Himalaya. GeoMod2008. International Geological Modelling Conference. Florence, Italy. 22–24 September. Bolletino di Geofisica Teorica e Applicata 49:254–257

Mukherjee S (2009a) Channel flow model of extrusion of the higher Himalaya-successes & limitations. Geophysical Research Abstract. European Geosciences Union. Vienna, Austria, 19–24 April. vol. 11, EGU2009-13966. http://meetingorganizer.copernicus.org/EGU2009/EGU2009-13966.pdf

Mukherjee S (2009b) Flanking Microstructures from the Zanskar Shear Zone, NW Indian Himalaya. Int J Earth Sci (submitted)

Mukherjee S (2009c) Flanking microstructures from the western Indian Himalaya. Abstract. MicroAnalysis, processes, time (MAPT) session: mineral microstructures: their implications and applications. The Mineralogical Society of Great Britain and Ireland. 30 August–04 September 2009. University of Edinburg (submitted)

Mukherjee S (2009d) Boudins from the Sutlej & the Zanskar Sections of the Western Indian Higher Himalaya. Geophysical Research

Abstract. European Geosciences Union. Vienna, Austria, 19–24 April. vol. 11, EGU2009–13972. http://meetingorganizer.copernicus.org/EGU2009/EGU2009-13972.pdf

Mukherjee S (2009e) Macroscopic 'V' pull-apart structure in garnet. Photo of the month. J Struct Geol. doi:10.1016/j.jsg.2008.10.014

Mukherjee S, Koyi HA (2009a) Flanking microstructures. Geol Mag 146:517–526. doi:10.1017/S0016756809005986

Mukherjee S, Koyi HA (2009b) Higher Himalayan Shear Zone, Zanskar Indian Himalaya—microstructural studies & extrusion mechanism by a combination of simple shear & channel flow. Int J Earth Sci (in press). doi:10.1007/s00531-009-0447-z; http://www.springerlink.com/content/k64l47n84884j428/fulltext.pdf

Mukherjee S, Pal P (2000) Tectonic structures of the Karakoram metamorphic belt, its significance in the Geodynamic Evolution. Unpublished Report. Summer Undergraduate Research Award. University of Roorkee

Mukherjee S, Koyi HA, Talbot CJ (2008) Double detachments and secondary thrusting inside the Higher Himalayan Shear Zone—intrinsic to extrusive flow patterns and independent to climate—insights from analogue models. GeoMod2008. International Geological Modelling Conference. Florence, Italy. 22–24 September. Bolletino di Geofisica Teorica e Applicata 49:257–261

Mukherjee S, Koyi HA, Talbot CJ (2009) Out-of-sequence thrust in the Higher Himalaya—a review & possible genesis, vol 11, EGU2009-13783. European Geosciences Union General Assembly. Geophys Res Abs. Vienna, Austria, 19–24 April. http://meetingorganizer.copernicus.org/EGU2009/EGU2009-13783.pdf

Nelson KD, Zhao W, Brown LD et al (1996) Partially molten middle crust beneath Southern Tibet: synthesis of project INDEPTH results. Science 274:1684–1688. doi:10.1126/science.274.5293.1684

Pai S-I (1956) Viscous Flow Theory I—Laminar flow. D. Van Nostrand, New Jersey, p 51

Papanastasiou CT, Georgiou GC, Alexandrou AN (2000) Viscous fuid flow. CRC Press, Florida, p 253

Passchier CW, Trouw RAJ (2005) Microtectonics, 2nd edn. Springer, Berlin, p 43

Patel RC, Singh S, Asokan A et al (1993) Extensional tectonics in the Himalayan orogen, Zanskar, NW India. In: Treloar PJ, Searle MP (eds) Himalayan Tectonics. Geological Society of London, Special Publication No 74, pp 445–459. doi:10.1144/GSL.SP.1993.074.01.30

Ramsay JG, Lisle R (2000) The techniques of modern structural geology 3: applications of continuum mechanics in structural geology. Academic Press, San Diego, pp 837–884

Robinson D, DeCelles P, Copeland P (2006) Tectonic evolution of the Himalayan thrust belt in western Nepal: implications for channel flow models. Geol Soc Am Bull 118:865–885. doi:10.1130/B25911.1

Rogers RH (1978) Fluid mechanics. Routledge & Kegan Paul, London, pp 93–109

Saklani PS (2005) Tectonic geology of the main central thrust, Garhwal-Uttaranchal. In: Saklani PS (ed) Himalaya (Geological aspects). Satish Serial Publishing House, Delhi, pp 173–189. ISBN:81-89304-04-6.3

Scaillet B, Holtz F, Pichavant M (1996) Viscosity of Himalayan Leucogranites: implications for mechanisms of granite magma ascent. J Geophys Res 101:27691–27699. doi:10.1029/96JB01631

Schlichting H, Gersten K (1999) Boundary layer theory, 8th revised enlarged edn. Springer, Berlin

Searle MP (1999) Extensional and compressional faults in the Everest-Lhotse massif, Khumbu Himalaya, Nepal. J Geol Soc London 156:227–240. doi:10.1144/gsjgs.156.2.0227

Searle MP, Godin L (2003) The South Tibetan Detachment and the Manaslu Leucogranite: a structural reinterpretation and restoration of the Annapurna–Manaslu Himalaya, Nepal. J Geol 111:505–523. doi:10.1086/376763

Searle MP, Cooper DJW, Rex AJ (1988) Collision tectonics of the Ladakh-Zanskar Himalaya. In: Shackleton RM, Dewey JF, Windley BF (eds) Tectonic evolution of the Himalayas and Tibet Phil Trans Royal Soc London A326, London, pp 117–150. doi:10.1098/rsta.1988.0082

Searle MP, Waters DJ, Rex DC et al (1992) Pressure, temperature and time constraints on Himalayan metamorphism from eastern Kashmir and Western Zanskar. J Geol Soc London 149:753–773. doi:10.1144/gsjgs.149.5.0753

Searle MP, Simpson RL, Law RD (2003) The structural geometry, metamorphic and magmatic evolution of the Everest massif, High Himalaya of Nepal-South Tibet. J Geol Soc London 160:345–366. doi:10.1144/0016-764902-126

Singh S (1993) Collision tectonics: metamorphic and geochronological constraints from parts of Himachal Pradesh, NW-Himalaya. Unpublished PhD Thesis. University of Roorkee, India, pp 1–289

Singh S, Jain AK, Barley ME (2005) Himalayan orogenic channel: when did it start? Abstract Number: 58-SE-A0396. Asia Oceania Geosciences Society. Session: solid earth. 2nd Annual General Meeting 20–24 June 2005, Singapore. http://www.asiaoceania.org/abstract/se/58-SEA0396.pdf

Spurk J (1993) Fluid mechanics problems and solutions. Springer, Berlin, pp 58–60

Srikantia SV, Bhargava ON (1998) Geology of Himachal Pradesh. Geological Society of India, Bangalore, pp 1–406

Stephenson BJ, Waters DJ, Searle MP (2000) Inverted metamorphism and the Main Central Thrust: field relations and thermobarometric constraints from the Kishtwar Window, NW Indian Himalaya. J Meta Geol 18:571–590. doi:10.1046/j.1525-1314.2000.00277.x

Stephenson BJ, Searle MP, Waters DJ et al (2001) Structure of the Main Central Thrust zone and extrusion of the High Himalayan deep crustal wedge, Kishtwar–Zanskar Himalaya. J Geol Soc Lond 158:637–652

Talbot CJ, Aftabi P (2004) Geology and models of salt extrusion at Qum Kuh, central Iran. J Geol Soc London 161:321–334. doi:10.1144/0016-764903-102

ten Grotenhuis SM, Passchier CW, Bons PD (2002) The influence of strain localization on the rotation behaviour of rigid objects in experimental shear zones. J Struct Geol 24:485–499. doi:10.1016/S0191-8141(01)00072-4

Thakur VC (1992) Geology of Western Himalaya. Oxford, Pergamon

Thiede RC, Bookhagen B, Arrowsmith JR et al (2004) Climatic control on rapid exhumation along the Southern Himalayan Front. Earth Planet Sci Lett 222:791–806. doi:10.1016/j.epsl.2004.03.015

Treagus S, Lan L (2004) Deformation of square objects and boudins. J Struct Geol 26:1361–1376. doi:10.1016/j.jsg.2003.12.002

Treagus SH, Hudleston PJ, Lan L (1996) Non-ellipsoidal inclusions as geological strain markers and competence indicators. J Struct Geol 18:1167–1172. doi:10.1016/0191-8141(96)00039-9

Tripathi A, Gairola VK (1999) P–T conditions of metamorphism in the Garhwal Nappe. In: Jain AK, Manickavasagam RM (eds) Geodynamics of the NW Himalaya. Gond Res Gr Mem No 6. Field Science, Osaka, pp 167–172

Valdiya KS (1998) Dynamic Himalaya. University Press, Bangalore

Valdiya KS (2001) Reactivation of terrane-defining boundary thrusts in central sectors of the Himalaya: implications. Curr Sci 81:1418–1431

Vannay J-C, Grasemann B (1998) Inverted metamorphism in the High Himalaya of Himachal Pradesh (NW India): phase equilibria versus thermobarometry. Schweiz Mineral Petrogr Mitt 78:107–132

Vannay J-C, Grasemann B (2001) Himalayan inverted metamorphism and syn-convergence extension as a consequence of a general

shear extrusion. Geol Mag 138:253–276. doi:10.1017/S0016756801005313

Vannay J-C, Sharp DZ, Grasemann B (1999) Himalayan inverted metamorphism constrained by oxygen thermometry. Contrib Mineral Petrol 137:90–101. doi:10.1007/s004100050584

Vannay JC, Grasemann B, Rahn M et al (2004) Miocene to Holocene exhumation of metamorphic crustal wedge in the NW Himalaya: Evidence for tectonic extrusion coupled to fluvial erosion. Tectonics 23(TC1014):1–24. doi:10.1029/2002TC001429

Walker JD, Martin MW, Bowring SA et al (1999) Metamorphism, melting and extension: age constraints from the High Himalayan slab of southeast Zanskar and northwest Lahul. J Geol 107:473–495. doi:10.1086/314360

Walker CB, Searle MP, Waters DJ (2001) An integrated tectonothermal model for the evolution of the High Himalaya in western Zanskar with constraints from thermobarometry and metamorphic modeling. Tectonics 20:810–833. doi:10.1029/2000TC001249

Whipp DM Jr, Ehlers TA, Blythe AE et al (2005) Kinematic and erosion History of the Greater Himalayan Sequence, Central Nepal from Integrated Thermochronology and Numerical Modeling. Salt Lake City Annual Meeting. October 16–19. Geol Soc Am Abstr with Programs vol 37, 346 pp

Wobus C, Heimsath A, Whipple K (2005) Active out-of-sequence thrust faulting in the central Nepalese Himalaya. Nature 434:1008–1011. doi:10.1038/nature03499

Wu C, Nelson KD, Wortman G et al (1998) Yadong cross structure and South Tibetan Detachment in the east central Himalaya (890–900 E). Tectonics 17:28–45. doi:10.1029/97TC03386

Yin A (2006) Cenozoic tectonic evolution of the Himalayan orogen as constrained by along-strike variation of structural geometry, extrusion history, and foreland sedimentation. Earth-Sci Rev 76:1–131. doi:10.1016/j.earscirev.2005.05.004